

A SEARCH FOR GAMMA-RAY BURSTS AND PULSARS,  
AND THE APPLICATION OF KALMAN FILTERS TO  
GAMMA-RAY RECONSTRUCTION

A DISSERTATION  
SUBMITTED TO THE DEPARTMENT OF PHYSICS  
AND THE COMMITTEE ON GRADUATE STUDIES  
OF STANFORD UNIVERSITY  
IN PARTIAL FULFILLMENT OF THE REQUIREMENTS  
FOR THE DEGREE OF  
DOCTOR OF PHILOSOPHY

By  
Brian Jones  
October 1998

© Copyright 1999 by Brian Jones  
All Rights Reserved

I certify that I have read this dissertation and that in my opinion it is fully adequate, in scope and quality, as a dissertation for the degree of Doctor of Philosophy.

---

Peter Michelson  
(Principal Adviser)

I certify that I have read this dissertation and that in my opinion it is fully adequate, in scope and quality, as a dissertation for the degree of Doctor of Philosophy.

---

Vahé Petrosian

I certify that I have read this dissertation and that in my opinion it is fully adequate, in scope and quality, as a dissertation for the degree of Doctor of Philosophy.

---

Robert Wagoner

Approved for the University Committee on Graduate Studies:

# Abstract

High-energy  $\gamma$ -ray astronomy was revolutionized in 1991 with the launch of the Energetic Gamma-Ray Experiment Telescope (*EGRET*) on board the *Compton Gamma-Ray Observatory*. In addition to unprecedented instrument effective area and a narrow point-spread function, *EGRET* provided photon time-tagging to an absolute accuracy of  $100\ \mu\text{s}$ . The opportunity to analyze high-quality  $\gamma$ -ray data requires sophisticated statistical and analytic tools. Part I describes the analysis of periodic and transient signals in *EGRET* data. A method to search for the transient flux from  $\gamma$ -ray bursts independent of triggers from other  $\gamma$ -ray instruments is developed. Several known  $\gamma$ -ray bursts were independently detected, and there is evidence for a previously unknown  $\gamma$ -ray burst candidate. Statistical methods using maximum likelihood and Bayesian inference are developed and implemented to extract periodic signals from  $\gamma$ -ray sources in the presence of significant astrophysical background radiation. The methods allow searches for periodic modulation without *a priori* knowledge of the period or period derivative. The analysis was performed on six pulsars and three pulsar candidates. The three brightest pulsars, Crab, Vela, and Geminga, were readily identified, and would have been detected independently in the *EGRET* data without knowledge of the pulse period. No significant pulsation was detected in the three pulsar candidates. Furthermore, the method allows the analysis of sources with periods on the same order as the time scales associated with changes in the instrumental sensitivity, such as the orbital time scale of *CGRO* around the Earth. Eighteen X-ray binaries were examined. None showed any evidence of periodicity. In addition, methods for calculating the detection threshold of periodic flux modulation were developed.

The future hopes of  $\gamma$ -ray astronomy lie in the development of the *Gamma-ray Large Area Space Telescope*, or *GLAST*. Part II describes the development and results of the particle track reconstruction software for a *GLAST* science prototype instrument beamtest. The Kalman filtering method of track reconstruction is introduced and implemented. Monte Carlo simulations, very similar to those used for the full *GLAST* instrument, were performed to predict the instrumental response of the prototype. The prototype was tested in a  $\gamma$ -ray beam at SLAC. The reconstruction software was used to determine the incident  $\gamma$ -ray direction. It was found that the simulations did an excellent job of representing the actual instrument response.

# Acknowledgements

The acknowledgements page of the modern physics thesis has become a stage upon which seasoned and world-weary graduate students perform a tragicomic stand-up routine to amuse their family and friends. It is altogether fitting and proper that they should do so, since it is unlikely that those family and friends will read any of the rest of the thesis. Besides, they hope they will be mentioned. Nevertheless, it is a good medium, and a useful way to point out the people and institutions without whom, for better or worse, this work would never have been performed.

The number of people who have been a part of this cause is enormous. There is no way I can mention all of the friends and colleagues whom I appreciate, so I will just touch on a few. Beginning with the most general, I must thank the taxpayers of the United States who, whether they knew it or not, spent a vast amount of money to advance the frontiers of  $\gamma$ -ray astrophysics. I can only hope to have done them proud. I was fortunate enough to profit from data taken by the *EGRET* instrument, on board the Compton Gamma-Ray Observatory. I have deep appreciation for the work done to get *EGRET* into orbit and taking data by the scientists and staff of Goddard Space Flight Center, especially Dave Thompson, who was always particularly supportive of my work, and the Max Planck Institut für Extraterrestrische Physik. This collaboration has done an outstanding job in designing, building, and operating an instrument which has radically changed our understanding of the  $\gamma$ -ray sky. I'm proud to have been a small part of that group.

I'm also proud to be a part of a second international collaboration, this one responsible for *GLAST*. I have benefitted from the chance to work with scientists from Goddard, the Naval Research Laboratory, UC Santa Cruz, and Columbia University

in the United States, as well as the École Polytechnique and CEA in France, the University of Trieste in Italy and the University of Tokyo, as well as dozens of other institutions worldwide too numerous to mention. Being on the inside of a developing Big Science project has been eye-opening, to say the least. Specifically, I'd like to thank Steve Ritz, Neil Johnson, and Eric Grove for listening to the brash opinions of a grad student as if he were a Real Scientist.

The fact that no Stanford (or SLAC) people are included above reflects not their absence, but their proximity. A number of people in and around Stanford have made an indelible impression on me. My advisor Peter Michelson has given me tremendous freedom to pursue my own interests, even when they were not what most astrophysicists would call mainstream. Bill Atwood has been a tremendous motivator, and taught me a great deal. His methods are generally quite harsh, by his own admission, and he is never satisfied. For some reason which I still do not understand, this had the effect of spurring me on to better, more careful, and more thorough work, completed more rapidly, rather than to hatred and bitterness. Joe Fierro's Pucklike sensibilities drew me to the group in the first place, in the belief that it would be a fun place to work. He was a great help once I pestered him enough. Tom Willis graciously put up with a newcomer in his office, and helped me through the steep learning curve in *EGRET* minutiae. Although he's not at Stanford, Prof. Dave Wilkinson along with the rest of the Princeton faculty showed me what I am really capable of, and gave me the best undergraduate physics education available. After that, grad school was a breeze. And of course, without Marcia Keating in the Varian office, I would never have filed a study list, gotten paid, or managed to file the appropriate graduation forms. It doesn't matter how many Nobel Laureates we have wandering around; without Marcia, this place would fall apart. She will be greatly missed as she moves on to new challenges.

Pat Nolan, my *de facto* advisor, deserves a paragraph to himself. His patience, advice, and knowledge have been a prime factor in whatever success I may have had. He also deserves rich thanks for maintaining the computer systems and knowing arcane details about UNIX so that I didn't have to. It is a great privilege to have had the opportunity to learn from him.

Also critical have been my fellow graduate students in the Physics Department, especially Doug Natelson and Bill Tompkins. Doug, as my erstwhile roommate, had to put up with a lot and endured it well. Bill, as roommate and officemate, found he could never avoid me. He therefore sought to educate me, so that I would be more bearable. If I have given half as good as I've gotten from him, I consider myself a success.

On a more personal note, I would like to thank all of the members of TMBS for their support and prayers. I know the Lord would have given me strength without them, but they knocked at the door persistently, and it has paid off.

Primarily, however, support for an undertaking such as a Ph.D. has to come from the family. Fortunately, I have been blessed with the best family I could imagine. My parents have supported me in my quest "to be a scientist" from the very beginning, and always believed I could do it, even if they weren't sure why I wanted to. Plus, they paid for college. My brother Bill, aside from the non-trivial accomplishment of being a fantastically supportive brother, decided to study physics just so I wouldn't feel alone. And last, but by no means least, my beautiful wife Kim met me while I was yet a graduate student, and saw some kernel of value in me even then. Her love, support, and confidence in me have given me the strength to finish this work. My great blessing is that although this thesis is now part of the past, we have many wonderful years together in our future.



O LORD, *our Lord, how majestic is your name in all the earth!*

*You have set your glory above the heavens.*

*When I consider your heavens, the work of your fingers,*

*the moon and the stars, which you have set in place,*

*what is man that you are mindful of him,*

*the son of man that you care for him?*

Psalm 8 (NIV)

*The heavens declare the glory of God;*

*the skies proclaim the work of his hands.*

*Day after day they pour forth speech;*

*night after night they display knowledge.*

*There is no speech or language where their voice is not heard.*

*Their voice goes out into all the earth,*

*their words to the ends of the world.*

*In the heavens he has pitched a tent for the sun,*

*which is like a bridegroom coming forth from his pavilion,*

*like a champion rejoicing to run his course.*

Psalm 19 (NIV)

# Contents

<b>Abstract</b>	<b>iv</b>
<b>Acknowledgements</b>	<b>vi</b>
<b>I Methods for Time-Series Analysis</b>	<b>1</b>
<b>1 Introduction</b>	<b>2</b>
1.1 The $\gamma$ -Ray Observatories . . . . .	3
1.2 The <i>EGRET</i> instrument . . . . .	5
1.2.1 Instrumental Design . . . . .	5
1.2.2 Instrumental Calibration and Performance . . . . .	7
1.3 Successes with <i>EGRET</i> . . . . .	8
<b>2 Statistical Methods in <math>\gamma</math>-Ray Astronomy</b>	<b>10</b>
2.1 The Nature of the $\gamma$ -Rays . . . . .	11
2.1.1 Diffuse Background . . . . .	12
2.1.2 Spectral Differences . . . . .	13
2.2 Instrumental Effects . . . . .	14
2.2.1 Point-Spread Function . . . . .	14
2.2.2 Sensitive Area . . . . .	15
2.2.3 Energy Dispersion . . . . .	16
2.3 Likelihood Analysis . . . . .	17
2.4 Applying Likelihood Analysis to <i>EGRET</i> . . . . .	19

2.4.1	Binned Likelihood . . . . .	20
2.4.2	Maximizing the Likelihood with <b>LIKE</b> . . . . .	23
2.5	Parameter Estimation vs. Hypothesis Testing . . . . .	24
2.6	Bayesian Methods . . . . .	25
2.6.1	Bayes' Theorem . . . . .	26
2.6.2	The Odds Ratio . . . . .	28
2.6.3	Marginalization and Confidence Regions . . . . .	29
2.6.4	Advantages and Disadvantages . . . . .	30
2.7	Calculating Upper Limits . . . . .	31
2.7.1	Upper Limits from <b>LIKE</b> . . . . .	32
2.7.2	Calculating More Accurate Upper Limits . . . . .	33
2.7.3	Implications for Extant Conclusions . . . . .	34
<b>3</b>	<b><math>\gamma</math>-Ray Bursts</b>	<b>36</b>
3.1	Recent Observations . . . . .	39
3.2	$\gamma$ -Ray Burst Models . . . . .	40
3.2.1	Energy production mechanisms . . . . .	41
3.2.2	Blast wave theories . . . . .	43
3.2.3	Observable consequences . . . . .	45
3.3	<i>EGRET</i> observations . . . . .	46
3.4	Possible <i>EGRET</i> -only Bursts . . . . .	48
3.4.1	Statistical Methods . . . . .	49
3.4.2	Results . . . . .	53
3.4.3	Discussion . . . . .	55
3.5	Conclusions . . . . .	60
<b>4</b>	<b>Periodic Time-Series Analysis</b>	<b>62</b>
4.1	Pulsars . . . . .	63
4.1.1	<i>EGRET</i> Contributions . . . . .	65
4.1.2	Models . . . . .	67
4.2	Statistical Methods . . . . .	69
4.2.1	Previous Methods . . . . .	70

4.2.2	Maximum Likelihood . . . . .	75
4.2.3	Application to <i>EGRET</i> . . . . .	78
4.2.4	Bayesian Inference . . . . .	83
4.2.5	Upper Limits and Thresholds . . . . .	85
4.2.6	Bin-free Maximum Likelihood . . . . .	90
4.3	Searching for Pulsars . . . . .	91
4.3.1	Measurement of Known Pulsars . . . . .	92
4.3.2	Searches for Geminga-like Pulsars . . . . .	95
4.3.3	Results . . . . .	100
4.4	X-Ray Binaries . . . . .	101
4.4.1	Thresholds and Searches . . . . .	102
4.4.2	Results . . . . .	103
<b>5</b>	<b>Conclusions</b>	<b>107</b>
<b>II</b>	<b>The October 1997 <i>GLAST</i>-prototype Beam Test</b>	<b>111</b>
<b>6</b>	<b><i>GLAST</i>: The Next Generation</b>	<b>112</b>
6.1	Potential Improvements . . . . .	113
6.2	The Baseline <i>GLAST</i> Instrument . . . . .	115
<b>7</b>	<b>Testing the <i>GLAST</i> Science Prototype</b>	<b>118</b>
7.1	The SLAC $e^-$ Beam . . . . .	118
7.2	The Beam Test Instrument . . . . .	121
7.2.1	Tracker . . . . .	121
7.2.2	Calorimeter . . . . .	124
7.2.3	Anti-Coincidence Detector . . . . .	125
7.3	Summary of Data . . . . .	126
7.4	Simulations . . . . .	127
<b>8</b>	<b>Reconstructing Events</b>	<b>129</b>
8.1	Pair Production . . . . .	130

8.2	Track Reconstruction . . . . .	132
8.3	The Annotated Kalman Filtering Formulae . . . . .	136
8.3.1	The Filtering Equations . . . . .	138
8.3.2	The Smoothing Equations . . . . .	139
8.3.3	Goodness of Fit . . . . .	141
8.3.4	Kalman Filter Implementation for the Beam Test . . . . .	142
8.4	Track Finding Algorithm . . . . .	143
8.4.1	The Exhaustive Search . . . . .	143
8.4.2	Beam Test Algorithm . . . . .	144
8.5	Measurement Error and Multiple Scatter Estimates . . . . .	146
8.6	Noise . . . . .	148
8.7	Energy . . . . .	150
8.7.1	Energy Splitting . . . . .	151
8.7.2	Energy Dispersion . . . . .	151
8.8	Potential Improvements . . . . .	153
8.8.1	Track Fitting . . . . .	153
8.8.2	Track Finding . . . . .	154
8.8.3	Energy Estimations . . . . .	156
8.9	Calculating the Point-Spread Function . . . . .	157
8.10	Extended Kalman Filters . . . . .	159
<b>9</b>	<b>Instrument Response</b>	<b>160</b>
9.1	Alignment . . . . .	160
9.2	Cuts . . . . .	161
9.3	Expected Beam Test Point-Spread Widths . . . . .	163
9.4	Conclusions . . . . .	166
9.4.1	Comparison of Beam Test and Monte Carlo Results . . . . .	166
9.4.2	Implications for <i>GLAST</i> . . . . .	169
<b>A</b>	<b>SSB Arrival Time Corrections</b>	<b>171</b>
<b>B</b>	<b>Summary of Kalman Filtering Equations</b>	<b>173</b>

C Track Finding Algorithm	174
Bibliography	177

# List of Tables

1.1	$\gamma$ -Ray telescope performance . . . . .	7
3.1	Three minute burst time scale results . . . . .	54
3.2	Ten minute burst time scale results . . . . .	54
3.3	Thirty minute time scale results . . . . .	55
3.4	One hour burst time scale results . . . . .	55
3.5	Triggered bursts not independently detected . . . . .	56
3.6	Hardness ratios for burst candidates . . . . .	57
3.7	Joint burst probabilities . . . . .	59
4.1	Typical pulsar parameters . . . . .	65
4.2	Detection of known $\gamma$ -ray pulsars by <code>timevar</code> . . . . .	93
4.3	Thresholds for pulsed sources . . . . .	98
4.4	<i>GLAST</i> pulsed signal thresholds . . . . .	100
4.5	Results of period search with <code>timevar</code> . . . . .	101
4.6	Low mass X-ray binaries . . . . .	104
4.7	High mass X-ray binaries . . . . .	105
4.8	Low-mass X-ray binary results . . . . .	106
4.9	High-mass X-ray binary results . . . . .	106
6.1	<i>GLAST</i> baseline characteristics . . . . .	115
6.2	Institutions in the <i>GLAST</i> collaboration . . . . .	117
7.1	Radiation lengths of Pb available . . . . .	123
7.2	Energy bands used for analysis . . . . .	124

9.1	Cut efficiencies . . . . .	163
9.2	Calculated point-spread widths . . . . .	170



# List of Figures

1.1	The electromagnetic spectrum . . . . .	2
1.2	The Compton Gamma-Ray Observatory . . . . .	4
1.3	The <i>EGRET</i> Instrument . . . . .	6
2.1	Full sky photon counts . . . . .	11
2.2	Full sky galactic diffuse map . . . . .	13
2.3	Full sky exposure map . . . . .	22
2.4	Full sky intensity map . . . . .	24
2.5	Bayesian upper limits . . . . .	34
3.1	$\gamma$ -Ray bursts observed by <i>BATSE</i> . . . . .	38
3.2	Overall $\gamma$ -ray burst significance from the Monte Carlo simulations. . .	52
4.1	Geminga likelihoods . . . . .	82
4.2	Geminga light curves . . . . .	83
4.3	Geminga phase offsets . . . . .	85
4.4	Marginalized geminga likelihood . . . . .	86
4.5	Pulsar periods vs. period derivatives . . . . .	92
4.6	Likelihood of flux modulation from Crab . . . . .	94
4.7	Light curves of Crab . . . . .	94
4.8	Likelihood of flux modulation from Vela . . . . .	95
4.9	Light curves of Vela . . . . .	96
4.10	Likelihood of flux modulation in PSR 1706-44 . . . . .	96
4.11	Light curves of PSR 1706-44 . . . . .	97

4.12	$\dot{E}/D^2$ vs. pulsar period . . . . .	99
6.1	The <i>GLAST</i> satellite . . . . .	113
7.1	Location of End Station A at SLAC . . . . .	120
7.2	Beam test experimental scheme . . . . .	121
7.3	Pancake and Stretch tracker configurations . . . . .	122
7.4	CsI(Tl) Calorimeter . . . . .	125
8.1	Kalman filtering . . . . .	133
8.2	Kalman smoothing . . . . .	135
8.3	Measurement error distributions . . . . .	147
8.4	Strip occupancies . . . . .	149
8.5	Monte Carlo energy dispersion . . . . .	152
8.6	Probability distributions of $e^-e^+$ energy split as a function of total incident energy . . . . .	158
9.1	Point-spread width dependence on total energy and energy splitting fraction . . . . .	164
9.2	Pancake X-Projection PSF vs. Monte Carlo . . . . .	166
9.3	Stretch X-Projection PSF vs. Monte Carlo . . . . .	168
9.4	Projected point-spread distributions . . . . .	169

# **Part I**

## **Methods for Time-Series Analysis**

# Chapter 1

## Introduction

The desire to experiment with the extremes of nature is innate. While it is almost always amusing, it can be informative as well. Such is the case in the study of some of the most energetic photons produced in space: the  $\gamma$ -rays (Figure 1.1). With at least ten million times the energy of ordinary optical photons,  $\gamma$ -rays represent a unique window into the most energetic processes in astrophysics—the (electromagnetically) roaring jets from active galactic nuclei, the arcing plasmas in the intense gravitational fields of pulsars, and the enigmatic and inordinately powerful explosions known as  $\gamma$ -ray bursts.

The immense value of  $\gamma$ -rays for astrophysics lies both in their role as telltale markers of large energy-generation processes and in their likelihood of passing unperturbed through vast reaches of intergalactic space. Measuring the  $\gamma$ -ray spectra of astrophysical objects sharply constrains estimates of their total energy output.

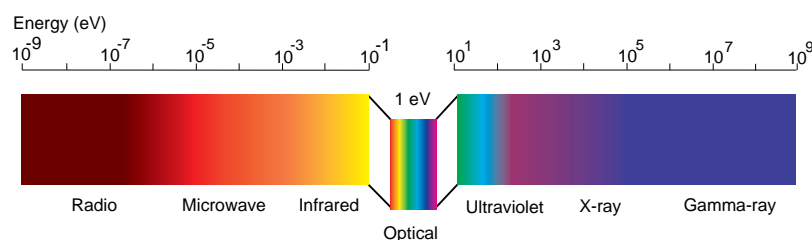


Figure 1.1: The Electromagnetic Spectrum.  $\gamma$ -Rays occupy the highest energy extreme of the electromagnetic spectrum, from 10 MeV to over 300 GeV.

Since  $\gamma$ -rays are so energetic, many astrophysical sources emit the bulk of their total power output at these high energies. In addition,  $\gamma$ -rays travel relatively unimpeded through space. Since they carry no charge, they are nearly unaffected by galactic and intergalactic magnetic fields. Their small interaction cross section means that they are relatively unaffected by dust and gas in the intervening space between the source and the detector. A high-energy  $\gamma$ -ray can travel through the central plane of the Galaxy with only a 1% chance of being absorbed [43].  $\gamma$ -Rays may be observed from Earth essentially unchanged since they left the distant violence in which they were created.

However, every silver lining has its cloud. The Earth's atmosphere is very good at absorbing  $\gamma$ -rays. Unfortunately, it means that precise astrophysical  $\gamma$ -ray observations must be done in space. The second difficulty in  $\gamma$ -ray astronomy is intrinsic to the energy production mechanisms that produce  $\gamma$ -rays in the first place. Because  $\gamma$ -rays are so energetic, most sources produce very few of them. Detectors must be very efficient to collect these rare photons, and at the same time be able to discriminate against the sea of undesirable charged particles trapped in the Earth's magnetic field and albedo  $\gamma$ -rays which are generated in the Earth's atmosphere. This discrimination requires background rejection on the order of one part in  $\sim 10^5$  or better.

## 1.1 The $\gamma$ -Ray Observatories

Experience with terrestrial accelerator-based  $\gamma$ -ray detectors suggested that a spark chamber might be an effective astrophysical  $\gamma$ -ray detector. In the mid-1970s, *SAS 2* [39] and *COS B* [12] proved the concept of a  $\gamma$ -ray satellite telescope, while discovering several of the brightest  $\gamma$ -ray sources. Simultaneously, NASA envisioned the *Great Observatories for Space Astrophysics* program: a series of satellite telescopes designed to give unprecedented insights into electromagnetic emission from infrared to  $\gamma$ -rays. Under the auspices of this program, the Space InfraRed Telescope Facility (*SIRTF*) infrared telescope has been designed, the Advanced X-ray Astrophysics

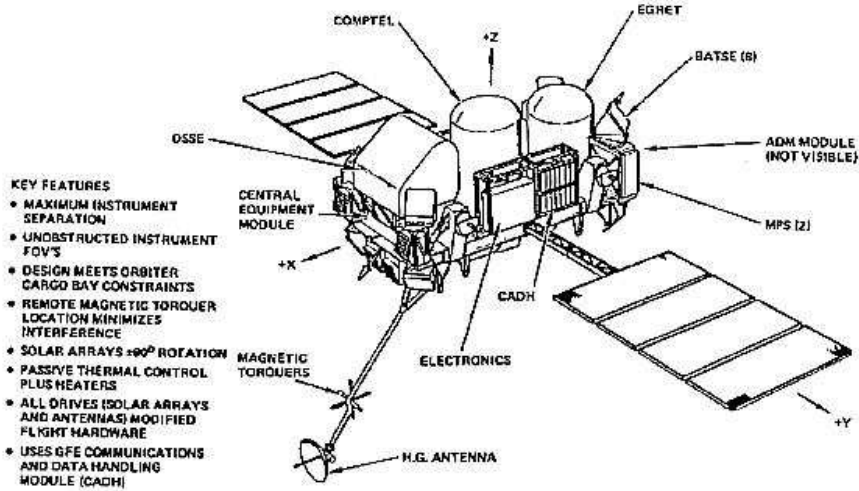


Figure 1.2: The Compton Gamma-Ray Observatory. *EGRET* is the dome on the right end of the spacecraft. It is coaligned with *COMPTEL*. Rounding out the instruments aboard *CGRO* are *OSSE*, which is very sensitive to  $e^-e^+$  annihilation lines, and the omni-directional *BATSE*  $\gamma$ -ray burst detector.

Facility (AXAF) has been designed and built, the Hubble Space Telescope has revolutionized optical astronomy, and the Compton Gamma-Ray Observatory (*CGRO*) has explored the  $\gamma$ -ray sky from less than 0.1 MeV to more than 10 GeV (Figure 1.2).

The five orders of magnitude in energy of the electromagnetic spectrum observed by *CGRO* require four different instruments on the satellite. The lowest energy  $\gamma$ -rays interact primarily through the photo-electric effect. The Oriented Scintillation Spectrometer Experiment (*OSSE*) covers the energy range from 0.05–10 MeV with a field of view of  $3.8 \times 11.4$  [78]. The Compton Telescope (*COMPTEL*) detects Compton scattered electrons, the most significant  $\gamma$ -ray interaction in the energy range between 1 MeV and almost 30 MeV, to image the  $\gamma$ -ray sky with a field of view of  $\sim 1$  sr [178]. The Energetic Gamma-Ray Telescope Experiment (*EGRET*) measures pair-conversion events in a spark chamber, like *SAS 2* and *COS B*. It is sensitive to energies between 20 MeV and 30 GeV, with a field of view of  $\sim 1$  sr [71, 92]. In addition, a fourth instrument aboard *CGRO* is optimized to detect  $\gamma$ -ray bursts. The Burst and

Transient Source Experiment (*BATSE*) consists of eight uncollimated detectors, one on each corner of the *CGRO* spacecraft, sensitive to 25 keV–2 MeV  $\gamma$ -rays with nearly uniform coverage of the sky [47].

The *EGRET* instrument is the focus of Part I of this work. The instrument was built and operated by a collaboration of scientists at Stanford University, Goddard Space Flight Center (Greenbelt, Maryland), the Max Planck Institut für Extraterrestrische Physik (Garching, Germany), and the Grumman Aerospace Corporation (Bethpage, New York). It was launched aboard *CGRO* on the Space Shuttle Atlantis (STS-37) on April 5, 1991 and was deployed two days later. It was activated on April 15, and began taking data on April 20. The instrument and its characteristics have been extensively documented [71, 92, 93, 150, 193]; we will briefly touch on the highlights relevant to data analysis in §2.2.

Future  $\gamma$ -ray telescopes will further extend our understanding of astrophysical  $\gamma$ -ray processes. The *GLAST* instrument, scheduled for launch in 2005 [134, 2, 14, 15], will improve upon the successes of *EGRET* as it brings  $\gamma$ -ray astronomy to the 21st century. The test of a *GLAST* science prototype will be the focus of Part II of this work. Details of the current instrument baseline design are given in §6.2.

## 1.2 The *EGRET* instrument

Spark chambers detect  $\gamma$ -rays *via* pair production. Pair production refers to the process whereby a  $\gamma$ -ray converts to an electron–positron pair in the presence of matter. The detection process is more fully described in §8.1. The resulting electrons and positrons are easily detected because they are charged particles.

### 1.2.1 Instrumental Design

To optimize the detection and resolution of  $\gamma$ -rays, the *EGRET* instrument consists of a series of thin tantalum (Ta) sheets interleaved with planes of conducting wires spaced by 0.8 mm. Below this multilayer spark chamber is a NaI(Tl) calorimeter known as the TASC (Total Absorption Shower Counter). Surrounding the spark

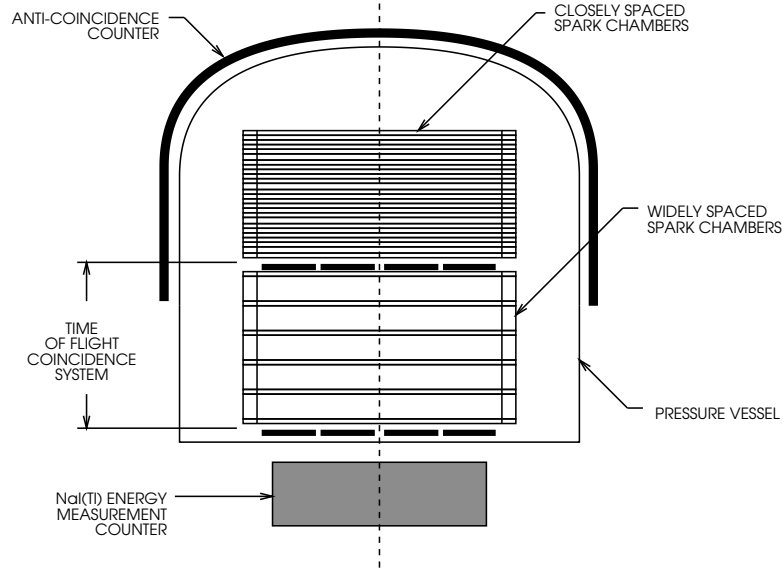


Figure 1.3: The *EGRET* instrument. The total height of the spark chambers is approximately 1 m.

chamber is a monolithic plastic scintillator to reject charged cosmic ray particles. The schematic design is shown in Figure 1.3.

99.5% of  $\gamma$ -rays will pass undetected through the anticoincidence scintillator into the 28 closely-spaced spark chamber modules, where it has a  $\sim 33\%$  chance of converting to an  $e^-e^+$  pair. If it does so, the pair will ionize the (mostly) neon gas in the spark chamber along their trajectories. Below the closely-spaced modules is a time-of-flight system designed to measure whether the particles are upward- or downward-moving. The system consists of two layers of  $4 \times 4$  arrays of plastic scintillator tiles, spaced 60 cm apart. By combining measurements from the two layers, the time-of-flight delay can be measured to within  $\sim 1.5$  ns, and the general direction of the particles can be estimated. At any given time, a limited number of general directions are considered valid for an instrument trigger. The valid directions depend on orbital parameters, and are designed to exclude the Earth's limb, as well as limiting the field-of-view when desired.

If the time-of-flight system registers the passage of a downward particle from a valid region of the sky, and the anticoincidence system has not been triggered by a



	<i>SAS 2</i>	<i>COS B</i>	<i>EGRET</i>	<i>GLAST</i>
Field of View	0.25 sr	0.25 sr	1.0 sr	2.6 sr
Effective Area >100 MeV	100 cm <sup>2</sup>	70 cm <sup>2</sup>	1200 cm <sup>2</sup>	~7000 cm <sup>2</sup>
Angular Resolution <sup>a</sup>	1°5	1°5	0°6	~0°1
Energy Resolution <sup>b</sup>	~100%	42%	18%	10%
Point Source Sensitivity <sup>c</sup> (photons cm <sup>-2</sup> s <sup>-1</sup> )	10 <sup>-6</sup>	10 <sup>-6</sup>	10 <sup>-7</sup>	<4 × 10 <sup>-9d</sup>

<sup>a</sup>RMS at 500 MeV

<sup>b</sup>full-width, half maximum at 100 MeV

<sup>c</sup>>100 MeV, 10<sup>6</sup> s exposure, unless noted

<sup>d</sup>1 year, high-latitude, >100 MeV, 5σ

Table 1.1: Performance of four high-energy  $\gamma$ -ray telescopes. Continually improving technology is reflected in improving performance from the earliest instruments, *SAS 2* and *COS B*, through *EGRET* and on to the proposed *GLAST* instrument.

charged particle, a high voltage pulse is applied to the wires in the spark chamber modules. Ionized paths short the wires to ground, and the affected wires are recorded digitally in ferrite cores.

The Total Absorption Spectrometer Calorimeter (TASC), located below the spark chamber, measures the total energy of the  $\gamma$ -ray event. It consists of 8 radiation lengths of NaI(Tl), and has an energy resolution of ~20% FWHM from a few tens of MeV to several tens of GeV. Events are tagged with an arrival time by the *CGRO* on-board clock to an absolute accuracy of 100  $\mu$ s and a relative accuracy of 8  $\mu$ s. The energy measurements made by the TASC are corrected on the ground for energy lost in the spark chamber and shower leakage.

## 1.2.2 Instrumental Calibration and Performance

Good calibration of the *EGRET* instrument was critical to the proper understanding of its data. The calibration was as extensive as its literature [193, 92, 93, 115, 150]; only the results will be stated here. There are three areas in which we will need to know the instrument performance: the point-spread function, or the distribution of the measured  $\gamma$ -ray incident angles as a function of the true incident angle; the sensitive (or effective) area, or the physical area for collecting  $\gamma$ -rays multiplied by

the efficiency, as a function of position on the sky at any given time; and the energy dispersion, or the distribution of measured energy as a function of the true energy.

These three functions were measured and recorded in tabular form as a function of aspect angle and energy. Their use in data analysis will be discussed in §2.2. A reasonable approximation to the point-spread width assumes a relatively simple functional form. The half-angle which defines a cone containing  $\sim 68\%$  of the  $\gamma$ -rays from a point on the sky may be taken as

$$\theta_{68} = 5.85(E/100 \text{ MeV})^{-0.534} \quad (1.1)$$

where  $E$  is the energy in MeV [193].

The sensitive area and energy dispersion are not easily expressible in functional form. Tables of their values were created in machine readable form, and analysis programs access them directly.

The performance of the *EGRET* instrument compares very favorably with its predecessors, *SAS 2* and *COS B*. The order of magnitude increase in effective area and improved point-spread function lead to the order of magnitude improvement in the point source sensitivity. A comparison of the telescopes, along with the proposed *GLAST* telescope, is shown in Table 1.1.

### 1.3 Successes with *EGRET*

The *Compton Gamma-Ray Observatory* has been very fortunate in successfully achieving and exceeding its design goals. Still operating some 7 years after launch, it has almost quadrupled its planned lifetime. While the entire observatory has been critical in advancing our understanding of astrophysics from 15 keV to 30 GeV (most notably the shocking revelation from *BATSE* that the mysterious  $\gamma$ -ray bursts are isotropically distributed on the sky), we will concentrate here on the contributions made by *EGRET*, with a view toward future advancements to be made by *GLAST*.

*EGRET* has significantly improved our understanding of pulsars [43, 191]. Six  $\gamma$ -ray pulsars have been identified by *EGRET*, and their pulse periods have been

measured. *EGRET* observations of pulsars will be discussed in Chapter 4. Significant advancements have been made through observations of the Galactic [73] and extragalactic [212] diffuse background emission. The largest number of identified *EGRET* sources are the  $\gamma$ -ray blazars. Roughly 60 blazars have been identified above 100 MeV, leading to new insights into blazar emission mechanisms [62]. While the *BATSE*  $\gamma$ -ray burst measurements were the most revolutionary discovery, *EGRET* has made significant contributions to our understanding of  $\gamma$ -ray bursts at the highest energies [122].  $\gamma$ -Ray bursts will be discussed in Chapter 3.

*CGRO* has yielded a wealth of information about the  $\gamma$ -ray sky. Much of that information has directly increased our understanding of astrophysical systems. In particular, *EGRET* has given us an unprecedented view of the high-energy  $\gamma$ -ray sky. *EGRET* has identified a great number of new sources; the launch of *GLAST* will give us a tool to understand what exactly it is that we have found.

## Chapter 2

# Statistical Methods in $\gamma$ -Ray Astronomy

Optical astronomy has long been famous for breathtaking images of distant galaxies, star-forming clouds, and beautiful nebulae. While  $\gamma$ -ray astronomy can produce equally beautiful results, the nature of the photons and the instrument yield data which must be analyzed very differently than data from other wavelengths. The first major difference is the sparsity of the photons; integration times of days are usually required to observe all but the brightest sources. A multitude of astrophysical conditions also affect the nature of the data. Cosmic ray interactions with Galactic dust and gas produce diffuse background  $\gamma$ -rays. Different energy generation mechanisms produce different spectral profiles across the energy range observed by *EGRET*. Several specific instrumental responses also shape the data analysis process. A finite point-spread function means that  $\gamma$ -ray directions will be determined to within a statistical distribution around the true source direction. Instrumental sensitivity to three orders of magnitude in energy across the field of view of more than a steradian is not uniform as the platform orbits at 17,000 miles per hour. Meanwhile, our estimates of all these parameters depend on the  $\gamma$ -ray energy, which is only known to limited accuracy.

Despite these impediments to observation, *EGRET* has been very successful in

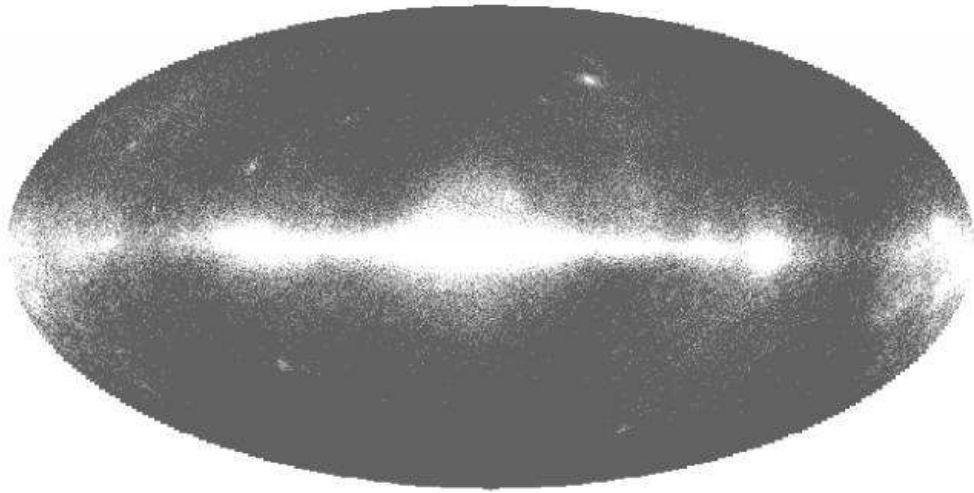


Figure 2.1: All  $\gamma$ -rays above 100 MeV measured by *EGRET* in phase I, II, and III, binned at a scale of  $0.5^\circ$ .

making  $\gamma$ -ray observations. This chapter will examine the nature of the *EGRET* data, and the statistical methods used to analyze it.

## 2.1 The Nature of the $\gamma$ -Rays

Several major features of the high-energy  $\gamma$ -ray sky are evident from the simplest possible examination. Figure 2.1 shows the raw photon counts for the whole sky in  $0.5^\circ \times 0.5^\circ$  bins in Galactic coordinates. The Galactic center is evident at the center of the map, as is the Galactic disk. There are several bright spots in the plane, as well as some evident high-latitude sources. We will first examine the diffuse background, then see how statistical methods along with understanding of the background will help us identify point sources and estimate their locations and fluxes.

### 2.1.1 Diffuse Background

Almost two decades before the launch of *SAS 2*, Hayakawa [66] predicted that high-energy  $\gamma$ -rays would be produced as cosmic rays interacted with interstellar gas yielding pions, which would decay, directly or indirectly, into  $\gamma$ -rays. Indeed, experience with *SAS 2*, *COS B*, and *EGRET* has shown strong correlations of the diffuse  $\gamma$ -ray background at low Galactic latitudes with known Galactic structural features such as the spiral arms [39, 63, 119]. Based on indications that the diffuse  $\gamma$ -ray flux observed by *SAS 2* and *COS B* was approximately the intensity and shape expected from cosmic ray interactions with interstellar matter, a model of the diffuse flux was made for the purposes of *EGRET* data analysis [10, 75].

There are three main processes by which diffuse  $\gamma$ -rays are generated. The dominant process above  $\sim 70$  MeV is the decay of pions. Pions are produced when cosmic-ray protons interact with dust particles or gas. These pions then decay to high-energy  $\gamma$ -rays. Below  $\sim 70$  MeV,  $\gamma$ -rays can be produced by either bremsstrahlung of cosmic rays in interstellar clouds or by inverse-Compton upscattering of low-energy photons.

A good model of the Galactic diffuse  $\gamma$ -ray intensity thus requires a good model of the distribution of interstellar matter in the Galaxy, and a good model of the cosmic ray flux throughout the Galaxy. The first may be well approximated using maps of the distribution of hydrogen, which comprises most of the interstellar matter in the Galaxy. Atomic hydrogen has been carefully mapped with observations of the 21 cm hyperfine transition line. Molecular hydrogen is more difficult to map, but may be approximated by assuming that CO is a good tracer, easily identified by its 2.6 mm emission line. A constant ratio of CO to molecular hydrogen is typically assumed throughout the galaxy.

Much more difficult is the estimation of the Galactic cosmic ray flux. Since the flux cannot be directly measured, assumptions about the distribution of cosmic rays must be made. For the purposes of *EGRET* analysis, Bertsch [10] and Hunter [75] assume that cosmic rays are in dynamic equilibrium with the interstellar magnetic pressure and the gravitational pressure of the galactic matter. These assumptions, convolved with the instrument point-spread function (§2.4), result in the map of diffuse Galactic  $\gamma$ -rays shown in Figure 2.2, which is in good agreement with the observed

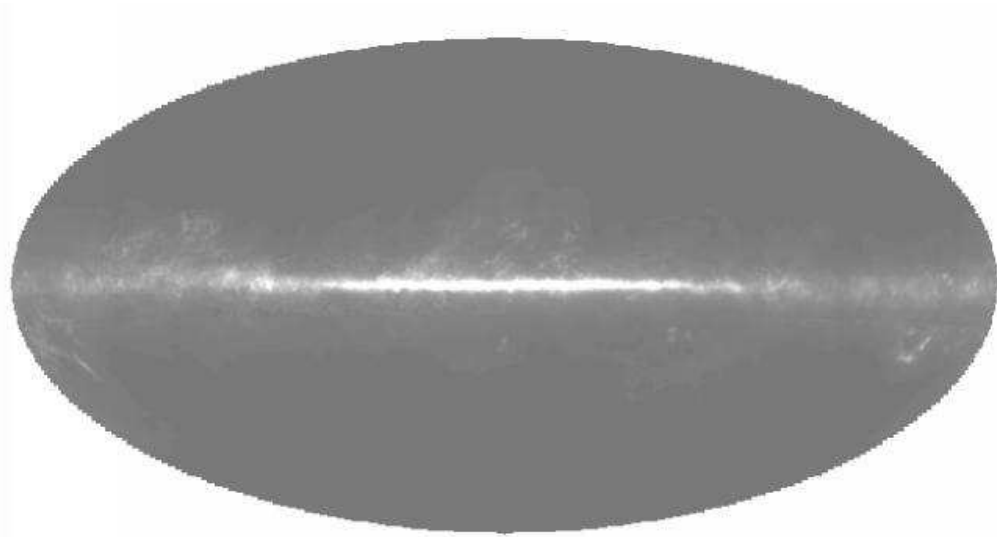


Figure 2.2: The assumed Galactic contribution to the diffuse  $\gamma$ -ray background, taken from measurements of atomic and molecular hydrogen, and convolved with the *EGRET* point-spread function. This is a map of  $G_{ij}$ , as defined in equation (2.20).

intensity map shown in Figure 2.4. Of course, at high galactic latitudes the diffuse background is primarily extragalactic [182], although there is significant galactic diffuse background at high latitude. Some or all of this extragalactic background is due to a large number of weak sources, while some of it may be due to a truly diffuse background [212].

### 2.1.2 Spectral Differences

*EGRET*'s broad energy range allows the spectra of sources and the diffuse background to be measured. The spectrum of almost every *EGRET* source is well fit by a power law. Since  $\gamma$ -rays are so sparse, the power laws are usually quoted as a function of the number of photons, instead of a function of energy as is sometimes used for other wavelengths. The form is then

$$I(E) = I_0 E^{-\alpha} \text{ photons cm}^{-2} \text{ s}^{-1} \text{ MeV}^{-1} \quad (2.1)$$

where  $I(E)$  is the differential photon flux. The spectral index  $\alpha$  is close to 2.0 for most sources, though it can be as low as 1.42 for pulsars. The Galactic diffuse background has a bit softer spectrum—about 2.1.

## 2.2 Instrumental Effects

The quality and nature of the data depend equally on the photons and the instrument which observes them. Any attempt to analyze the data must consider the instrumental response as the basis for an analysis method. The three main aspects of the instrumental response that we must consider are the point-spread function, the sensitive area, and the energy dispersion. There is no reason, *a priori*, to expect that the instrument response function should separate cleanly into these three functions. However, it offers great simplification to the data analysis, and in practice seems to be a good approximation.

### 2.2.1 Point-Spread Function

It is important to be able to quantify the ability of a  $\gamma$ -ray telescope to correctly reconstruct the true incident direction of a  $\gamma$ -ray. To precisely define this, we will distinguish between the “point-spread density” and the “point-spread function.” The point-spread density, or PSD, refers to the probability density distribution of incident  $\gamma$ -ray directions measured by the instrument from a point source. This distribution may in general be a function the true position of the point source (the inclination and azimuth relative to the centerline of the telescope) and the energy of the  $\gamma$ -ray:

$$\text{PSD} = \text{PSD}(\theta, \phi; \theta_0, \phi_0, E_0) \quad (2.2)$$

where  $\theta_0, \phi_0$  represents the true source position and  $E_0$  is the true  $\gamma$ -ray energy. The apparent  $\gamma$ -ray direction is  $(\theta, \phi)$ . Often, we will require a probability, as opposed to a probability density. The differential probability of measuring a photon in a differential



element  $d\theta d\phi$  is given by

$$dP = \text{PSD}(\theta, \phi; \theta_0, \phi_0, E_0) \sin \theta d\theta d\phi \quad (2.3)$$

The point-spread function is the differential probability, often integrated over azimuth and energy to yield a function of inclination, as in equation (2.6).

The *EGRET* PSD was measured at the Stanford Linear Accelerator Center in 1986. A beam of electrons with tunable energies between 650 MeV and 30 GeV was back-scattered off pulsed laser photons.  $\gamma$ -Rays were produced between 15 MeV and 10 GeV by inverse-Compton scattering [115]. The point-spread density was measured as a function of apparent  $\gamma$ -ray position for 10 discrete energies, 5 inclination angles ( $\theta_0$ ) and 3 azimuthal angles ( $\phi_0$ ). The resulting tables yield the relative probability of detecting a photon at  $(\theta, \phi)$  assuming values of the other three parameters. In addition, *EGRET* operates in up to 87 different “modes,” corresponding to different triggering criteria.\* These modes are designed to maximize the operating field of view, even when part of the geometric field of view is obscured by the Earth or its limb.

### 2.2.2 Sensitive Area

A second function which is clearly critical for data analysis is the sensitive area of instrument. The sensitive area (or effective area) is the projected area of the detector multiplied by its efficiency. It too is a function of incident  $\gamma$ -ray parameters:

$$\text{SA} = \text{SA}(\theta_0, \phi_0, E_0) \quad (2.4)$$

Clearly, the sensitive area of the instrument is also dependent on the instrument mode.

---

\*These different modes correspond to allowing only photons from certain broad regions of the sky as defined by coincidence of different combinations of time-of-flight tiles.

### 2.2.3 Energy Dispersion

Finally, the analysis must consider energy dispersion. The energy dispersion function gives the distribution of measured energy for a given true energy. The measured energy varies from the true energy because of noise in the photomultipliers, fluctuations in the shower leakage from the calorimeter, and incomplete correction for energy losses elsewhere in the instrument.

$$\text{ED} = \text{ED}(E; E_0, \theta_0, \phi_0) \quad (2.5)$$

Taken together, these three functions yield the point-spread width approximation in equation (1.1) in the following way. We first notice from the calibration data that the point-spread function is roughly azimuthally symmetric, and that it does not vary widely with the true inclination angle. Then we can find

$$\text{PSF}(\theta) = \frac{2\pi}{N} \int_{E=E_{min}}^{E_{max}} \int_{E'=0}^{\infty} E'^{-\alpha} \text{PSF}(\theta, E') \text{ED}(E', E) dE' dE \quad (2.6)$$

where  $E$  is the measured  $\gamma$ -ray energy,  $E'$  is the true  $\gamma$ -ray energy, and  $N$  is a normalization factor. The deviation between the apparent incident angle and the true incident angle is  $\theta$ . The point-spread function  $\text{PSF}(\theta)$  is the integral of the true-energy dependent point-spread function, weighted by the spectrum, integrated over the measured energy band from  $E_{min}$  to  $E_{max}$ , and integrated over all true energies, weighted by the energy dispersion function. This reflects the fact that there is some probability that a  $\gamma$ -ray of any given true energy will have a measured energy between  $E_{min}$  and  $E_{max}$ .

This integral was done numerically for a number of energy bands, and a Gaussian fit to the results led to equation (1.1) [193].

## 2.3 Likelihood Analysis

The sparsity of astrophysical  $\gamma$ -rays and the complicated instrumental response of the *EGRET* instrument suggests statistical data analysis that functions at the photon-by-photon level, taking into account backgrounds and the instantaneous instrument state to extract the most information from each photon. Early analyses of *COS B* data were based on a cross-correlation method [69]. However, this method could not easily handle the highly structured background that is typical of high-energy  $\gamma$ -ray astrophysics. Later, a maximum likelihood technique was brought to bear on *COS B* data with much greater success [164]. Based on this success, maximum likelihood techniques were adopted for use with *EGRET* [117].

The central idea of likelihood analysis is very simple. Given a set of models, we wish to find the model which is most likely to be responsible for the observed data. The *likelihood* is defined as the probability of the observed data, given a choice of model. The likelihood is written as follows:

$$\mathcal{L}(D|M) \tag{2.7}$$

where  $D$  represents the observed data, and  $M$  the model. Quantities to the right of the  $|$  sign are taken as given and fixed, making the likelihood a conditional probability. The *maximum likelihood* method determines the best model by maximizing this likelihood function. A special, but very common, case is that of a parameterized model. For example, consider that we wish to measure the flux of a  $\gamma$ -ray source. We will imagine an idealized detector with 100% efficiency and an angular area of  $\alpha$  sr from the source. The number of  $\gamma$ -rays emitted in a unit time is Poisson distributed, so the likelihood of measuring  $n'$  photons from a source with intensity  $\mu$  is given by

$$\mathcal{L}(D|\mu) = \frac{\alpha}{4\pi} \frac{e^{-\mu} \mu^n}{n!} \tag{2.8}$$

where  $n$  is the number of photons emitted from the source, and  $n' = (\alpha/4\pi)n$ . To find our best estimate of  $\mu$ , we maximize this likelihood. In fact, we will find it more convenient (and mathematically equivalent) to maximize the logarithm of the

likelihood.

$$\ln \mathcal{L}(D|\mu) = -\mu + n \ln \mu + \ln \left( \frac{\alpha}{4\pi n!} \right) \quad (2.9)$$

The last term is constant, and thus for maximization purposes can be ignored. Setting the derivative of equation (2.9) to zero, we find

$$0 = -1 + n/\mu \implies \mu = n = \frac{4\pi}{\alpha} n' \quad (2.10)$$

Unsurprisingly, in this simple example, we find that the number of photons measured per unit time divided by the subtended angle fraction is the best estimate of the flux.

One other example is illustrative. Let us assume we have some Gaussian process with a constant mean and a known variance  $\sigma^2$ . A series of observations  $\mathbf{x}$  is made, and the most likely mean value  $\mu$  is desired. The likelihood function is

$$\mathcal{L}(\mathbf{x}|\mu) = \prod_i e^{-\frac{(x_i - \mu)^2}{2\sigma^2}} \quad (2.11)$$

Taking the logarithm, we have

$$\ln \mathcal{L}(\mathbf{x}|\mu) = -1/2 \sum_i \frac{(x_i - \mu)^2}{\sigma^2} \quad (2.12)$$

We notice that  $-2 \ln \mathcal{L}$  is formally equivalent to  $\chi^2$ . In fact, this is an example of a general result: in the limit that all distributions involved are Gaussian, the maximum likelihood result is the same as the  $\chi^2$  minimizing result. This is an example of a more general result known as Wilks' Theorem [211]; it will be described more thoroughly in §2.5.

**Maximum Likelihood Confidence Regions.** Maximum likelihood methods also yield confidence regions. Following Eadie, et al. [36], we first consider the case of a Gaussian distribution with unit variance and unknown mean  $\mu$ . The likelihood is

$$\mathcal{L}(\bar{x}|\mu) = (2\pi)^{-N/2} \exp \left[ -\frac{1}{2} \sum_{i=1}^N (x_i - \mu)^2 \right]$$

$$= (2\pi)^{-N/2} \exp \left[ -\frac{N}{2}(\bar{x} - \mu)^2 \right] \exp \left[ -\frac{1}{2} \sum_{i=1}^N (x_i - \bar{x})^2 \right] \quad (2.13)$$

The  $\ln \mathcal{L}$  is thus a parabola in  $\mu$  of the form  $-\frac{N}{2}(\mu - \bar{x})^2$ . In the case that  $N = 1$ , let  $\ln \mathcal{L} \geq -1/2$ . This corresponds to the interval  $-1 \leq \mu - \bar{x} \leq +1$ . From the properties of the normal distribution, we know that this must contain 68.3% of the distribution. Similarly, the interval corresponding to  $\ln \mathcal{L} \geq -2$  contains 95.5% of the distribution.

This would be merely a curiosity if not for the following. Suppose that the likelihood function is a continuous function of  $\mu$ , with only one maximum. In that case, we may reparameterize our observed variable in terms of a new variable  $g(\mu)$  such that the likelihood as a function of  $g$  is parabolic. We may now find the confidence region in  $g$  as we did above. Given that region, we may invert the reparameterization to find a confidence interval in  $\mu$ . Furthermore, we notice that the function is the same, whether it is parameterized by  $\mu$  or  $g$ . That is,

$$\ln \mathcal{L}(\bar{x}|\mu) = \ln \mathcal{L}(\bar{x}|\mu(g)) \quad (2.14)$$

Thus, we can find the confidence region in  $\mu$  directly by determining the point at which the  $\ln \mathcal{L}$  has decreased by 1/2 for 68% or 2 for 95.5%, without ever finding the reparameterization  $g$ . However, note that the interval is central in  $g$  since the likelihood as a function of  $g$  is a Gaussian, but it is not necessarily central in  $\mu$ .

## 2.4 Applying Likelihood Analysis to *EGRET*

We can see now how to proceed in *EGRET* data analysis. Take all the data accumulated in some time period. The likelihood of that data is the product over differential elements of angle and energy of the Poisson probability density of detecting the photons, given the rate of photons times the probability of detecting each photon. The rate  $\mu$  can be expressed as

$$\mu(\ell, b, E; \ell_0, b_0) = \int_{E=0}^{\infty} [I(\ell_0, b_0) \text{PSF}(\ell, b, E'; \ell_0, b_0) + B(\ell, b)] \text{SA}(\ell, b, E') \text{ED}(E', E) dE' \quad (2.15)$$

The rate is a function of the measured energy and position on the sky. The source intensity  $I$  depends only on the true source position  $(\ell_0, b_0)$ . The background  $B$  is assumed to have already been convolved with the point-spread function. The three instrument functions depend on the instrument mode  $m$  as well; this dependence will be suppressed for clarity.

The likelihood is then the product over all differential parameter elements of the Poisson probability of measuring (or not measuring, as was the case) a photon in that element, given the rate in that element from equation (2.15). The appearance of derivatives of products encourages us to use the logarithm of the likelihood. Denoting the integrated rate over measured energies as  $\bar{\mu} = \int_{E_{min}}^{E_{max}} \mu(\ell, b, E) dE$ , the log likelihood becomes

$$\ln \mathcal{L}(\ell_0, b_0) = \int_{\ell} \int_b [-\bar{\mu}(\ell, b; \ell_0, b_0) + n \ln \bar{\mu}(\ell, b; \ell_0, b_0)] d\ell db \quad (2.16)$$

where  $n$  is the number of photons observed in a differential element  $d\ell db$ . Since the element is differential, this must be either 1 or 0. The integral thus divides into an integral and a sum:

$$\ln \mathcal{L}(\ell_0, b_0) = - \int_{\ell} \int_b \bar{\mu}(\ell, b; \ell_0, b_0) d\ell db + \sum_{i=1}^N \ln \bar{\mu}(\ell_i, b_i; \ell_0, b_0) \quad (2.17)$$

where the sum is evaluated for the parameters of each photon. While this looks fairly simple,  $\bar{\mu}$  is quite a complicated object, implicitly containing four integrals. We would like to maximize equation (2.17) over  $\ell_0$  and  $b_0$ , the source position. Computationally, this is a herculean task, requiring evaluation of a six-dimensional integral at each trial point  $(\ell_0, b_0)$ . Clearly, some simplification is necessary.

### 2.4.1 Binned Likelihood

The most obvious simplification is to give up on individual photons, and create binned maps. While binning is always undesirable, as it loses information in the data, in this case binning is minimally undesirable. Our derivation above considered differential elements in the parameters; essentially, we let the bin size go to zero. It has been

shown that using a finite but small bin size speeds computation dramatically at very little expense of accuracy [199].

A standard analysis program called **LIKE** was developed for the map-based likelihood analysis of *EGRET* data [117]. **LIKE** considers the total expected  $\gamma$ -ray rate in each pixel, typically  $0.5^\circ \times 0.5^\circ$  on the sky.<sup>†</sup> This rate is the sum of the expected rates from the isotropic background, the galactic background, and a point source. In order to estimate rates for binned maps, the photons from any desired observation interval are binned as in Figure 2.1. In addition, the instrument exposure to the sky must be calculated. This is a function of the amount of observing time and the sensitive area during that time. Let  $T(\theta, \phi, m)$  be the amount of observing “livetime,” (that is, elapsed viewing time that the instrument was active, excluding occultations and instrument dead time) for a location  $(\theta, \phi)$  on the sky in an instrument observing mode  $m$  between time  $t_1$  and  $t_2$ . Only the total observing time in each mode is relevant; it need not be contiguous. Then the exposure  $\mathcal{E}(\Delta E; \theta, \phi)$  for a given measured energy range  $\Delta E$  to a point  $(\theta, \phi)$  on the sky is

$$\mathcal{E}(\Delta E; \theta, \phi, t_1, t_2) = \sum_m T(\theta, \phi, m; t_1, t_2) \bar{A}(\Delta E; \theta, \phi, m) \quad (2.18)$$

where

$$\bar{A}(\Delta E; \theta, \phi, m) = \int_{E=E_{min}}^{E_{max}} \int_{E'=0}^{\infty} E'^{-\alpha} \text{SA}(E'; \theta, \phi, m) \text{ED}(E, E') dE' dE \quad (2.19)$$

This exposure explicitly depends on the spectral index of the source or background, whichever is being observed. This is the first example of a continuing difficulty; the spectral index is required to calculate the exposure, but it is not known until after the flux is determined. In principle, the spectral index should be allowed to vary everywhere during the maximization process. An approximation would be to iterate. However, since most spectral indices are very nearly 2.0, and varying the index

---

<sup>†</sup> This scale is somewhat arbitrary. It was based largely on the scale to which the Galactic hydrogen has been mapped, as well as to ensure sufficient photons in each bin. It was not chosen to optimize the likelihood method. Nevertheless, for most energies the bin size is much smaller than the instrument point-spread width.

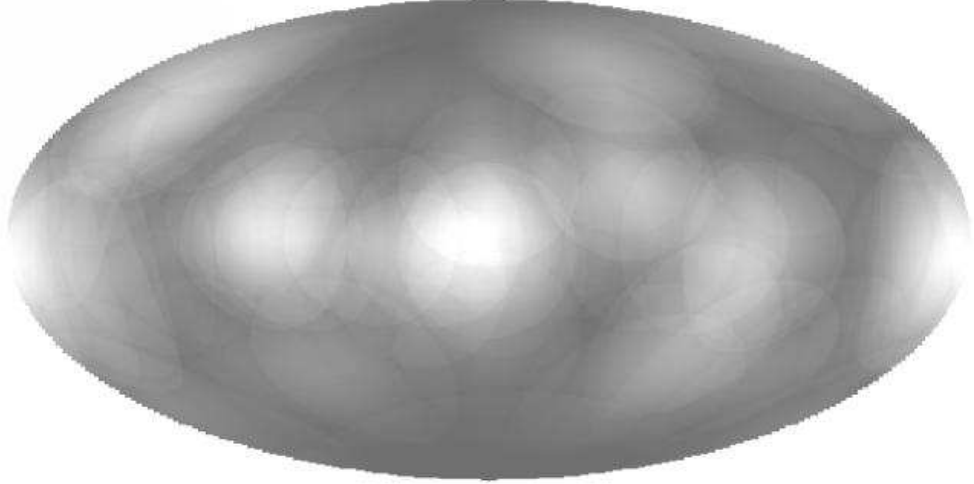


Figure 2.3: Combined *EGRET* exposure in phase I, II, and III. Phase I was an all-sky survey, with roughly even exposure. Phases II and III consisted of pointed observations for sources of interest. Lighter shade corresponds to more exposure.

requires recalculating the exposure maps (a computationally expensive prospect), a constant index is assumed. The exposure can be calculated for each pixel in the standard map; an example is shown in Figure 2.3.

To allow for the degrees of freedom in the background maps described above, the background is assumed to be a linear combination of isotropic and galactic background whose coefficients will be optimized. The isotropic diffuse count estimate for a given bin is  $g_b \mathcal{E}_{ij}$ , where  $g_b$  (“g-bias”) is the coefficient to be fit in units of photons  $\text{cm}^{-2} \text{s}^{-1} \text{sr}^{-1}$ , and  $\mathcal{E}_{ij}$  is the instrument exposure to pixel  $i, j$  in units of  $\text{cm}^2 \text{s sr}$ .

The Galactic component of the rate will depend on both the diffuse map and the instrument point-spread function, as well as the exposure. Denoting the binned radio diffuse gas map as  $f_{ij}$ , the rate due to the Galactic diffuse background is

$$G_{ij} = \frac{\sum_{kl} f_{kl} \mathcal{E}_{kl} \text{PSF}(\theta_{ij,kl})}{\sum_{kl} \text{PSF}(\theta_{ij,kl})} \quad (2.20)$$

where  $\theta_{ij,kl}$  is the angular distance between pixel  $i, j$  and pixel  $k, l$ . The denominator is a normalization factor, necessary since the sums over  $k$  and  $l$  may not be over



the entire sky. Pixels far from the point of interest will contribute negligibly to the estimation of source flux and location, but it is critical to good flux measurements to have a normalized point-spread function. Therefore, we allow analysis of only the pixels within some radius of analysis  $R_{anal}$ , but renormalize the point-spread function. In addition, to allow for the unknown cosmic ray flux and the CO/H<sub>2</sub> ratio, we will allow a constant multiplier  $g_m$  (“g-mult”) to be optimized as well.

So, then, given  $k$  sources in the field of view, the expected number of counts in bin  $i, j$  is

$$\mu_{ij} = g_m G_{ij} + g_b \mathcal{E}_{ij} + \sum_k c_k \text{PSF}(\theta_{ij,k}) \quad (2.21)$$

where  $\theta_{ij,k}$  is the angular distance between the position of source  $k$  and pixel  $i, j$ . This count estimate is a function of  $3k + 2$  parameters: the  $k$  source strengths, latitudes, and longitudes;  $g_m$ , and  $g_b$ . The fit values of  $g_m$  are consistently in the range 0.92–1.08. The fit level of  $g_b$  is usually around  $2 \times 10^{-5}$  photons cm<sup>-2</sup> s<sup>-1</sup> sr<sup>-1</sup> [43].

## 2.4.2 Maximizing the Likelihood with LIKE

Just as in the exact case, the distribution of photon counts in each bin is Poisson. The likelihood of a given map, then, is:

$$\mathcal{L}(D|c_k, \ell_k, b_k, g_m, g_b) = \prod_{ij} \frac{\mu_{ij}^{n_{ij}} e^{-\mu_{ij}}}{n_{ij}!} \quad (2.22)$$

with  $\mu_{ij}$  given by equation (2.21). The maximum likelihood estimates of  $c_k, \ell_k, b_k, g_m$ , and  $g_b$  are simultaneously solving the the set of equations

$$\left. \frac{\partial}{\partial c_k} \ln \mathcal{L}(\mu) \right|_{\mu=\hat{\mu}} = 0 \quad (2.23)$$

$$\left. \frac{\partial}{\partial \ell_k} \ln \mathcal{L}(\mu) \right|_{\mu=\hat{\mu}} = 0 \quad (2.24)$$

$$\left. \frac{\partial}{\partial b_k} \ln \mathcal{L}(\mu) \right|_{\mu=\hat{\mu}} = 0 \quad (2.25)$$

$$\left. \frac{\partial}{\partial g_m} \ln \mathcal{L}(\mu) \right|_{\mu=\hat{\mu}} = 0 \quad (2.26)$$

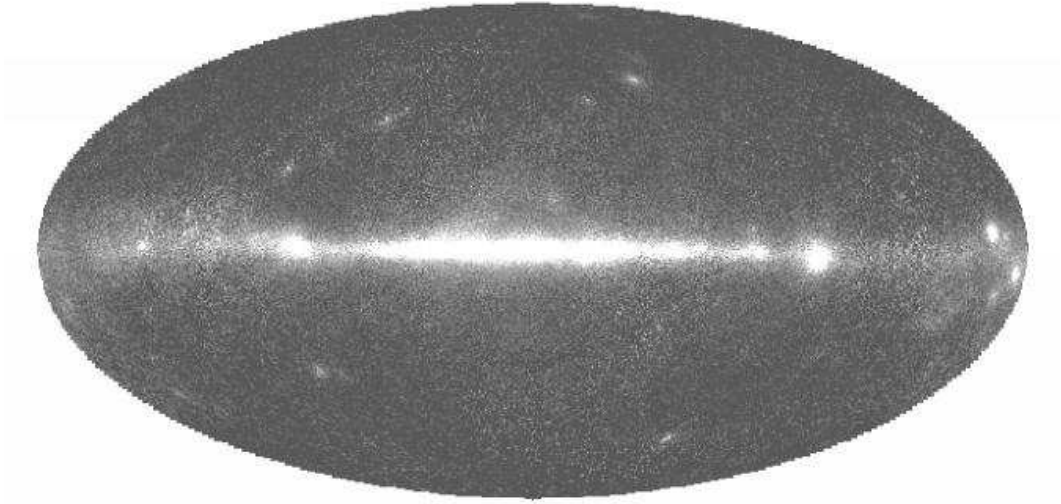


Figure 2.4:  $\gamma$ -Ray intensity as measured by *EGRET*. The counts map in Figure 2.1 is divided by the exposure map in Figure 2.3 to yield the  $\gamma$ -ray intensity.

$$\left. \frac{\partial}{\partial g_b} \ln \mathcal{L}(\mu) \right|_{\mu=\hat{\mu}} = 0 \quad (2.27)$$

where  $\hat{\mu}$  is optimized to satisfy all these conditions. This is just the multi-dimensional maximization of the likelihood function—there are  $3k + 2$  equations to solve simultaneously. For this reason, it is usually computationally much faster (although less accurate) to find the brightest source first, then fix its parameters and fit the next source. Once the locations of the sources are established, equation (2.21) divided by the exposure map yields an intensity map of the sky in Figure 2.4; equivalent to the optical image observed simply by peering through the eyepiece of an optical telescope.

## 2.5 Parameter Estimation vs. Hypothesis Testing

The foregoing discussion concerned the estimation of the position and flux of a source which was assumed to exist. The maximum likelihood technique not only allows for parameter estimation as described above but also for hypothesis testing. Hypothesis testing estimates the significance of the source detection. Highly significant sources are reliable; low significance sources may be statistical fluctuations.

Consider two hypotheses,  $M_0$  and  $M_1$ . For concreteness, let us assume that  $M_0$ , the null hypothesis, states that there is no source in the field of view. Further, we assume that  $M_1$  states that there is a source with non-zero flux in the field of view. If there are  $n$  degrees of freedom in  $M_0$ , and  $m$  degrees of freedom in  $M_1$ , then Wilks' Theorem [211] states that  $-2$  times the logarithm of the likelihood ratio is asymptotically distributed as  $\chi^2_{(m-n)}$ :

$$-2 \ln \frac{\mathcal{L}(D|M_0)}{\mathcal{L}(D|M_1)} \sim \chi^2_{(m-n)} \quad (2.28)$$

In the case of a source whose position is known from other experiments, there are 3 degrees of freedom in  $M_1$  ( $c_k, g_m, g_b$ ) and 2 degrees of freedom in  $M_0$  ( $g_m, g_b$ ). Thus, the likelihood is distributed as  $\chi^2_1$ . We define the *EGRET* test statistic  $\text{TS} \equiv -2(\ln \mathcal{L}_0 - \ln \mathcal{L}_1)$ . From the definition of the  $\chi^2$  distribution, this implies that the significance of a detection is given by  $\sqrt{\text{TS}}\sigma$  in the standard nomenclature. Thus, a  $\text{TS} = 16$  source is detected at the  $4\sigma$  level. Of course, that is for a single trial, and in fact many sources observed by other telescopes have been searched for with *EGRET*.

The case of previously unknown sources is a little more complicated.  $M_1$  now has 5 degrees of freedom:  $c_k, \ell_k, b_k, g_m, g_b$ . But the null hypothesis is degenerate in the position—the likelihood is independent of position when the flux is zero. In that case, Wilks' Theorem does not hold, so the distribution is not known. Some theoretical work has been done to determine this distribution [198]. Based on Monte Carlo simulations, *EGRET* sources are accepted as detections if, for sources at Galactic latitudes  $|b| > 10^\circ$ ,  $\sqrt{\text{TS}} > 4$ , and for sources at Galactic latitudes  $|b| < 10^\circ$ ,  $\sqrt{\text{TS}} > 5$ . Monte Carlo simulations have shown that for a perfect background model, roughly one spurious excess with  $\text{TS} > 16$  will be detected in an analysis of the entire sky [117, 43].

## 2.6 Bayesian Methods

Despite their formal similarity, conceptual differences between maximum likelihood analysis and Bayesian methods have kept the latter relegated, for the most part, to the

statistical backwaters of astrophysics. Some recent work using Bayesian methods has yielded useful results [174, 110, 111]; since Bayesian methods will be an appropriate alternative framework for later chapters, a brief overview will be presented here.

Traditional, or *frequentist*, statistics are predicated on the notion that extreme values of some function of the data given a null hypothesis indicate that the null hypothesis is probably wrong, and therefore the test hypothesis is probably true. Much of the confusion of the general population about “Statistics” is due to the two twists involved in frequentist analysis: first of all, the goal is to disprove the thing we suspect false, rather than find evidence for what we suspect true; and second, this is done by considering all possible outcomes from an ensemble of data sets. In the case of likelihood statistics, we calculate the statistic  $(-2 \ln \mathcal{L})$  and compare it to the distribution expected from the ensemble of data sets that might be generated if the null hypothesis were true. If the measured value of the likelihood is extreme, according to this distribution, we claim that the null hypothesis has been excluded to some confidence level.

### 2.6.1 Bayes’ Theorem

In contrast, the Bayesian method demands that we stay at all times in the realm of probability: specifically, the probability that the test hypothesis is true. To develop the mathematics, let us begin with what Scargle [174] calls the “obviously true” form of Bayes’ Theorem:

$$P(M|D)P(D) = P(D|M)P(M) \quad (2.29)$$

Formally, this follows from the definition of conditional probabilities. The probability of some statement  $M$  being true, given that another statement  $D$  is true is the joint probability of  $M$  and  $D$ . Any joint probability may be expressed as the probability of one statement times the conditional probability of the other. Or stated another way, the probability of  $A$  and  $B$  equals the probability of  $B$  and  $A$ . Thus Bayes’ Theorem is proved.

Clearly, the notation in equation (2.29) is suggestive. As we have identified above, the probability of the data, given a model, is known as the likelihood of the data.

Equation (2.29) points out that while we have been calculating likelihoods, what we really desire is  $P(M|D)$ ; that is, given the data that we have, what is the probability that a given model is true? This is the question which Bayesian methods set out to answer. To that end, we rearrange equation (2.29) into a more useful form.

$$P(M|D) = \frac{\mathcal{L}(D|M)P(M)}{P(D)} \quad (2.30)$$

Equation (2.30) gives us exactly what we want: the probability of a model being true, given the data that we have observed. We do not resort to any hypothetical ensembles of data, and more importantly, we make direct statements about the model in question.

Analogously to our likelihood calculations in §2.3, the model in question may be one of a discrete series, or it may be parameterized. In the case that the model is a function of a continuous parameter, then the left side of equation (2.30), known as the *posterior* probability, becomes a function  $P(M(\theta)|D)$ . It is interpreted as the probability that the true value of the parameter  $\theta_0$  is given by  $\theta$ .

Given the importance of the posterior probability, it behooves us to understand the right side of equation (2.30). The likelihood has been fully discussed.  $P(M)$  is known as the *prior* probability of the model. Except (apparently) in the case of quantum mechanics, probabilities are used to represent ignorance. We do not know the true value of a parameter, or which model is correct, so we assign probabilities to represent the knowledge that we do have.  $P(M)$  represents the knowledge we have about the system before we receive the data  $D$ . A common example is that of a parameterized model in which we know that the true value of the parameter  $\theta$  lies somewhere between  $\theta_{min}$  and  $\theta_{max}$ <sup>‡</sup>. The prior is then flat over the interval  $[\theta_{min}, \theta_{max}]$  and zero elsewhere. In other situations, it may be more appropriate to take a scale-invariant prior, which would have a logarithmic form. Such a prior is generally referred to as a “least informative prior.” It reflects only information about the structure of the experiment, and does not favor any specific outcome. Of course,

---

<sup>‡</sup>It will often be possible to take the limit of our results as  $\theta_{min} \rightarrow -\infty$  and  $\theta_{max} \rightarrow \infty$ .

if there is specific information about the true parameter value, the prior should reflect that information.

Finally, we must address the denominator of equation (2.30). This term, the probability of the data, serves as a normalization. It expresses the probability of measuring the data regardless of which model is actually true. If this can be rigorously calculated, then the left side of equation (2.30) will be a well-normalized probability distribution. In practice, it is often more practical to sidestep the issue by forming the odds ratio.

### 2.6.2 The Odds Ratio

Usually it is the case that we compare two discrete models, or that we compare a discrete model with a class of models characterized by a finite number of continuous parameters. In that case, the odds ratio conveniently handles our normalization issues. The odds ratio is formed by comparing the posterior probabilities of the different models. Consider two discrete models,  $M_0$  and  $M_1$ . For concreteness and comparison with §2.5, let us assume that  $M_0$  states that there is no source, and that  $M_1$  states that there is a source of a given flux at a given position. Then the odds ratio is

$$\frac{P(M_0|D)}{P(M_1|D)} = \frac{\mathcal{L}(D|M_0)P(M_0)}{\mathcal{L}(D|M_1)P(M_1)} \quad (2.31)$$

This gives the probability that there is no source relative to the probability that there is a source. Note that it only allows those two possibilities. A value of 1/3, for example, would mean it was three times more likely that there was a source than that there was no source. We know nothing about the probability that there were two sources.

Of course, the example in §2.5 was more complicated than this. The model  $M_1 = M_1(\mu)$  was a class of models, parameterized by the source strength. The odds ratio in that case is also a function of the parameter:

$$O(\mu) = \frac{P(M_1(\mu)|D)P(M_1(\mu))}{P(M_0|D)P(M_0)} \quad (2.32)$$

The function  $O(\mu)$  gives the odds that there is a source of strength  $\mu$  at a given position versus that there is no source. In most cases, we will be interested in the total odds ratio; that is, the odds that there is a source regardless of its strength. This is akin to the detection significance calculated in §2.5. We may calculate this ratio using the procedure known as marginalization.

### 2.6.3 Marginalization and Confidence Regions

We may eliminate uninteresting parameters by *marginalization*. This process acquired its odd name through a historical accident, when “integrations” were carried out numerically by adding columns of numbers into the margins of the page. In essence, the method is mathematically simple. Given any conditional probability, and the probability of the condition, we may integrate to eliminate the condition:

$$P(A) = \int_{B=B_{min}}^{B_{max}} P(A|B)P(B)dB \quad (2.33)$$

The application to the odds ratio is immediately clear. We simply integrate the numerator over all possible  $\mu$  to find the total odds ratio.

A very similar process may be used to find confidence intervals. Consider the situation when a source is known to exist. We then wish to find the best estimate of its flux, and a confidence interval for that estimate. Since the flux  $\mu$  must take on some positive value, we may evaluate the denominator of equation (2.30):

$$P(D) = \int_0^\infty \mathcal{L}(D|M(\mu))P(\mu)d\mu \quad (2.34)$$

Then the probability that the true value of  $\mu$  is between  $\mu_-$  and  $\mu_+$  is

$$P(\mu_- \leq \mu_0 \leq \mu_+) = \frac{\int_{\mu_-}^{\mu_+} \mathcal{L}(D|M(\mu))P(\mu)d\mu}{\int_0^\infty \mathcal{L}(D|M(\mu))P(\mu)d\mu} \quad (2.35)$$

For a given confidence level, there are an infinite number of choices of confidence intervals, as there are with frequentist statistics. There is no requirement that confidence intervals be contiguous. However, useful intervals can often be found by requiring

$\mu_- = \hat{\mu} - \delta\mu$  and  $\mu_+ = \hat{\mu} + \delta\mu$ , where  $\hat{\mu}$  is the most likely value of  $\mu$  [36]. The resulting interval is central by definition, and in the limit that the probability density is symmetric about the maximum and is smaller everywhere outside the interval than it is inside the interval, it is minimal.

#### 2.6.4 Advantages and Disadvantages

Advocates of frequentist and Bayesian methods have unfortunately been polarized into two extreme camps, with only the most acrimonious communication between them. In fact, both methods are rather like a powerful hunting rifle. Used properly, they are efficient and successful at doing their job. Improper use may result in permanent catastrophic injury and/or death. We will briefly examine the objections to both methods, and in doing so find that the disagreements are actually objections to using the methods improperly.

The major objection to the Bayesian method is the use of a prior. It is said that the prior subjectivizes what should be an objective procedure, and therefore reduces the results to a sort of “modified best guess” of the experimenter. The Bayesian responds that that is exactly true; indeed, if we use probabilities to express our ignorance, then we should hope that the results of an experiment reduce our ignorance. Furthermore, the Bayesian claims that all assumptions and prior knowledge are made explicit under the Bayesian formulation. It is certainly clear that the prior is the Achilles’ heel of the Bayesian method. There is no objective, prescribed method for obtaining a prior. However, there is also no objective, prescribed method for choosing a traditional statistic. The use of  $\chi^2$ , for example, implicitly assumes that the errors in the measurements are Gaussian, which may or may not be the case.

The primary objection to traditional statistics is the *ad hoc* procedure of selecting a statistic. Statistics are chosen based on their power and appropriateness, to be sure, but the choice is also largely guided by experience. The justification for the choice of statistics is generally its past success, rather than any *a priori* reasoning. In contrast, the Bayesian method prescribes the calculation for any experiment: form the likelihood and weight by the prior.



A secondary objection is philosophical in nature. Bayesians prefer to treat the true value of the parameter as a random variable, with the experimental data as the fixed and unchanging measure of reality. The parameter then has some probability of falling within the confidence region. The traditional approach treats the true value of the parameter as fixed and unchanging, and the data as only one possible outcome in an imagined ensemble, a shadow or projection of the true reality. The confidence region that we calculate from this instantiation of the data then has some probability of covering the true value of the parameter. <sup>§</sup>

Despite these objections, the two methods are actually compatible, and under the right circumstances, equivalent. In most circumstances, the maximum likelihood method is equivalent (for parameter estimation) to the Bayesian result with a flat prior. Whenever the implicit assumptions of a traditional analysis are matched by the explicit assumptions of a Bayesian analysis, the results will be the same.

## 2.7 Calculating Upper Limits

A significant positive detection of a source is the goal of all telescopes. However, null results can also be useful [133, 200]. It is often valuable to set an upper limit on the  $\gamma$ -ray flux of a source known from X-ray, optical, or radio observations. Determining the value of the upper limit is a statistical endeavor that requires a very careful definition of the goal. It has been noted that “the question of how to calculate an upper limit in the vicinity of a physical boundary is one of the most divisive in high-energy physics” [5]. Unfortunately, this is precisely the limit in which we find ourselves. A negative source flux is unphysical; nevertheless, a measurement of a weak (or non-existent) source in the presence of a large background may easily result in a data set best fit with a negative source flux. In order to combine such a result with other results, the flux must be reported as negative, with the confidence region found as in §2.3

---

<sup>§</sup>The philosopher will note a certain correspondence to historically important epistemological viewpoints. Sartre may debate Plato on the true nature of reality, but both are crushed by the rock of Sisyphus.

under the maximum likelihood method [5]. Otherwise, any combination of results from different observations or different experiments would be biased.

Once we have agreed upon a point estimate of the parameter, we must consider the confidence region that we wish to comprise the upper limit. In analogy to the confidence regions around point estimates, we will define the “ $1\sigma$  upper limit” (in frequentist terms) to be the top of an interval which will, when constructed from an ensemble of data sets, contain the true value of the flux 68.3% of the time. In Bayesian parlance, this means that the integral of the posterior probability distribution from zero to the  $1\sigma$  upper limit will be 68.3%.

### 2.7.1 Upper Limits from LIKE

The upper limits generated by LIKE do not fulfill this definition. There are three situations for which LIKE must generate an upper limit. The first is when the flux measurement is positive, but the confidence region extends to negative flux; e.g., a measurement of  $5 \pm 10$ . The second is when the flux measurement is negative, but the confidence region extends into positive territory. The third is when the flux measurement and the entire confidence interval are negative.

LIKE handles these situations in the following way. An upper limit is always quoted, and the flux measurement is quoted only if certain conditions are met. If  $TS > 1$  and the flux is positive, the flux and confidence regions are quoted. The upper limit is the top end of the confidence interval. If  $TS < 1$  or the flux is negative, only an upper limit is quoted. (Note that this immediately introduces the bias discussed above.) If the flux is positive, the upper limit is the top end of the confidence interval. If the flux is negative, LIKE finds the width of the confidence region, then shifts it so that it is centered on zero. The upper limit is then the top end of the shifted confidence interval.

The upper limit calculated for strong sources with positive flux clearly does not fulfill our definition. The confidence interval on the point estimate will contain the true value 68.3% of the time. The interval between zero and the upper limit is larger

than the confidence interval, and so must contain the true value at least 68.3% of the time.

The upper limit for sources with positive flux whose confidence intervals extend to negative fluxes also does not fulfill our definition. The 68.3% upper limit is found from the one-sided confidence interval; that is, the value  $\sigma_{u.l.}$  such that

$$\int_{-\infty}^{\sigma_{u.l.}} f(\hat{\mu}|\mu_0) d\hat{\mu} = 68.3\% \quad (2.36)$$

where  $f(\hat{\mu}|\mu_0)$  is the probability of measuring  $\hat{\mu}$  given a true flux of  $\mu_0$ . In the case of a Gaussian function  $f$ , the confidence of the integral evaluated to  $\sigma_{u.l.} = \hat{\mu} + \sigma$  may be evaluated. In general, the confidence of an interval extending to an upper limit of  $\hat{\mu} + \sigma$  depends strongly on the shape of  $f$ .

The most difficult situation is when the maximum likelihood source strength is negative. Barrett, et al. [5] suggest “lifting up” the measured flux to zero, evaluating the likelihood function and taking the upper limit. Instead, **LIKE** finds the width of the confidence interval about the measured (negative) flux, then centers that confidence interval about zero. It is very difficult to estimate the probability that a confidence interval obtained in this way would cover the true source strength; one must consider, for each possible value of the true source strength, all possible data sets. Any one of those data sets could fall into any of the categories we have outlined.

## 2.7.2 Calculating More Accurate Upper Limits

The upper limits calculated in this way are not only confusing and non-intuitive, they also do not (in general) fulfill our requirement: a confidence interval from zero to the upper limit should cover the true value 68.3% (or some other specified fraction) of the time. A Bayesian approach is in this case more intuitive and fulfills our requirements.

Instead of considering the ensemble of data sets that might produce a given flux measurement, we start directly with the data, and consider the range of true flux values that might produce the data. The requirement that all fluxes must be positive is easily fulfilled; we form a prior that is flat for  $\mu \geq 0$  and zero for negative  $\mu$ . Our posterior probability distribution is identical to the likelihood, except that it is

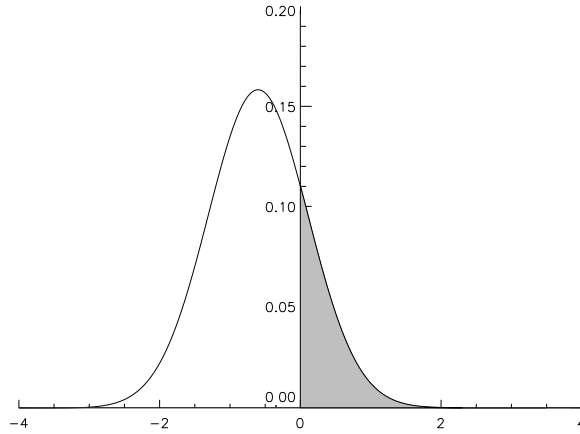


Figure 2.5: Upper limits calculated by Bayesian methods. This hypothetical likelihood function represents a measurement that gives a most likely value of some parameter to be less than zero. If the parameter is constrained by the physics to be positive, the Bayesian formalism suggests forming a prior which is zero for negative parameter values, and constant for positive parameter values. The posterior distribution would then look like the shaded portion of the curve.

zero for all negative values of  $\mu$ , and renormalized so that the integral over all values is unity. (Figure 2.5). The interpretation is then straightforward. The most likely value of the flux is zero; the 68.3% upper limit is found by integrating the posterior distribution from zero to some value  $\sigma_{u.l.}$  where the integral equals 68.3%.

### 2.7.3 Implications for Extant Conclusions

There are two sorts of conclusions typically drawn from *EGRET* upper limits. The first is generally qualitative. A known X-ray or radio source is not detected in the *EGRET* data. A “low” upper limit is taken as evidence that  $\gamma$ -ray emission is small or non-existent. A “high” upper limit is taken as weak evidence that there is little  $\gamma$ -ray emission, but that there was not sufficient data to draw a conclusion. For these sorts of conclusions, the LIKE upper limits are adequate (e.g., [109, 77]).

The second sort of conclusion is generally quantitative and statistical in nature. Often, possible source variability is examined in a number of observations. Some *EGRET* observations of a source (usually an AGN) yield significant detections, and

some yield only upper limits. Given flux measurements and confidence regions, it is a simple matter to formulate a  $\chi^2$  or likelihood test to determine if a constant flux model is compatible with the data. It is critical for such a test that upper limits have well-defined statistical properties. The upper limits generated by **LIKE** and quoted in the *EGRET* catalogs do not have these properties [195, 196, 65]. Unfortunately, catalogs of variability have been compiled based precisely on these upper limits [121]. All variability conclusions which involve upper limits are suspect, and should be treated as qualitative suggestions rather than quantitative results. Work by W. F. Tompkins is in progress to compile variability catalogs which have been calculated with statistically meaningful upper limits [199]; these should be used as soon as they are available.

# Chapter 3

## $\gamma$ -Ray Bursts

In the midst of the Cold War, in the late 1960s, a number of satellites were launched carrying  $\gamma$ -ray detectors. Sensitive to  $\gamma$ -rays between  $\sim 200$  keV and  $\sim 1.4$  MeV, the Vela satellites were designed to detect the testing or use of nuclear weapons. Between July of 1969 and July of 1972, four *Vela* satellites, equally spaced in the same circular orbit, detected 16 bursts of  $\gamma$ -ray energy. Comparisons of the  $\gamma$ -ray arrival times in different satellites determined that the origin of the bursts was more than 10 orbital diameters away. Thus, the first theory of  $\gamma$ -ray bursts, Soviet nuclear testing, was ruled out. Although national security concerns delayed the publication of these intriguing results by Klebesadel, Strong, and Olson [97] for a number of years, they would mark the beginning of the longest-standing mystery in astrophysics since the Shapley-Curtis debates.

A number of other bursts were observed over the next two decades [129, 208]. A consensus emerged fairly early that the source of the mysterious  $\gamma$ -ray bursts was Galactic in origin [53].\* Preliminary detections of flux over 1 MeV strengthened this conclusion [149]; Schmidt “showed” that detection of emission over 1 MeV required a Galactic origin, since the source luminosity required for bursts at more than  $\sim 100$  pc would imply an energy density that would result in  $\gamma$ - $\gamma$  pair production [175]—the optical depth to Earth for 1 MeV  $\gamma$ -rays would be  $>1$ . While there was never

---

\*This work will deal only with the so-called “classical  $\gamma$ -ray bursts.” Another class of transient  $\gamma$ -ray sources, the soft gamma repeaters, are clearly a different type of object.

significant evidence as expected that the bursts were preferentially located in the Galactic disk, it was presumed that the *BATSE* experiment on board *CGRO* would clear up any remaining ignorance about  $\gamma$ -ray bursts.

Despite the general consensus on the location of  $\gamma$ -ray bursts, the field attracted a wide variety of specific theories. Nemiroff identifies 99 distinct  $\gamma$ -ray burst theories put forth between 1968 and the end of 1991 [148]. Early theories placed bursts both locally and cosmologically distant, with energy generation mechanisms ranging from relativistic dust grains in the solar neighborhood to cometary collisions with neutron stars to white hole emission to vibrations of cosmic strings at  $z = 1000$  [4]. Nevertheless, by 1981, most models involved neutron stars in the Galactic plane. (Note, however, that Paczyński [157] put forth a theory of cosmological bursts with an optically thick  $e^-e^+$  plasma outflow in 1986. However, Paczyński also put forth a number of other unrelated theories of  $\gamma$ -ray bursts; thus it is unclear whether his apparent success is due to prescience or judicious covering of theory space.)

In September 1991, Gerald Fishman, representing the *BATSE* team at the first Compton Symposium, summarized the results of the  $\gamma$ -ray burst search since the launch of *CGRO* in April of that year. Everything that had been believed about the origin of bursts was shaken. The data, published first by Charles Meegan, Fishman, and others in *Nature* [123], showed an isotropic distribution of  $\gamma$ -ray bursts across the sky. Furthermore, there was already evidence of the so-called “edge” of the  $\gamma$ -ray burst distribution. That is, there were fewer low-flux bursts than would be expected if bursts were standard candles uniformly distributed in Euclidean space. The distribution was incompatible with a galactic disk population.

Old theories die hard, and much effort went into searches for the expected spatial and temporal correlations between bursts in the *BATSE* catalogs. While it appeared in the first *BATSE* catalog that some correlations might exist, additional bursts in the second catalog made isotropy much more likely [37]. Such statistical tests must be performed very carefully, due to the biases acquired from variable thresholds and exposures [160, 162, 107]. Similarly, only very marginal evidence could be found for repeating  $\gamma$ -ray bursts [161]. The distribution of all bursts observed to date (Figure 3.1) is compatible with a uniform distribution across the sky [125].

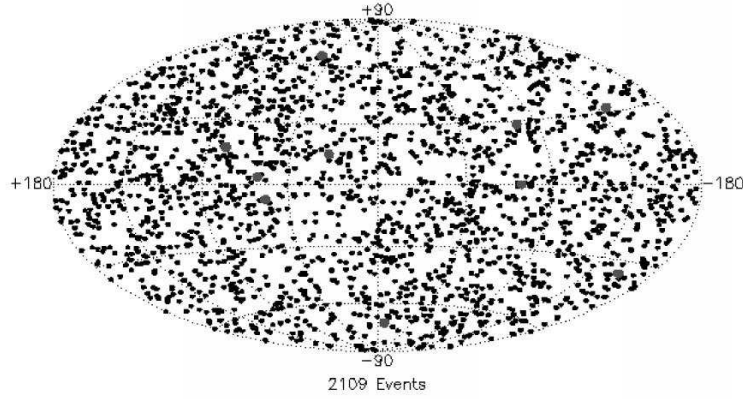


Figure 3.1: Locations of  $\gamma$ -ray bursts observed by *BATSE* as of July 3, 1998, in Galactic coordinates [125].

The *BATSE* data quickly winnowed away many  $\gamma$ -ray burst theories. But like opportunistic species after an ecological disaster, new theories quickly sprung up to fill the void (e.g., [186]). The new theories were classified primarily by the location of the bursts: locally (in the Oort cloud), in the hypothesized large Galactic halo, or at cosmological distances. The first of these was essentially abandoned when no suitable energy generation mechanisms could be envisioned. <sup>†</sup> Halo models generally involved interactions with old neutron stars that had been ejected from the plane into the halo. While the presence of a dark Galactic halo has been inferred from the rotation curves of other galaxies, its extent has not been conclusively measured [80]. The isotropy of the  $\gamma$ -ray burst distribution suggested that the radius of the halo would need to be many times the distance between the Earth and the Galactic center. Similarly, the halo of M31 (Andromeda) would be evident in the distribution once *BATSE* detected a large enough sample of bursts. The isotropy of the first 1122  $\gamma$ -ray bursts detected by *BATSE* [124] suggests if the bursts were in the Galactic halo, the halo would have a radius greater than 100 kpc. To be consistent with the lack of any excess toward Andromeda, the scale would have to be less than 400 kpc; a rather tight constraint. If the bursts were at cosmological distances, evolution effects conveniently explain the

---

<sup>†</sup>C. D. Dermer proposed a mechanism at a conference in Santa Barbara, California in 1995 involving antimatter comets annihilating with normal comets in the Oort cloud. This theory was apparently never published.



observed “edge” of the distribution. The energy required to produce the observed flux from such distances ( $\sim 10^{51}$ – $10^{54}$  ergs, modulo any beaming factor) is a few percent of the binding energy of a neutron star. Such an energy scale leads naturally to catastrophic theories involving neutron stars.

It had been realized quite early [175] that the large energy release required for distant  $\gamma$ -ray bursts would produce an environment that was optically thick to  $\gamma$ - $\gamma$  pair production. An assumption of cosmological origin of the  $\gamma$ -ray bursts led to a bifurcation of theories into those describing the energy generation mechanism and those describing the propagation of a large amount of compact energy, regardless of its source. The relevance of the latter theories for *EGRET* observation will be discussed in §3.2.

### 3.1 Recent Observations

In 1981, Fichtel & Trombka speculated that “identification of the [ $\gamma$ -ray burst] objects with observations at other wavelengths will probably be required before significant progress can be made in determining their origin” [41]. The day for which they were waiting arrived February 28, 1997, when the Italian satellite *BeppoSAX* discovered an X-ray afterglow to a  $\gamma$ -ray burst [30, 31]. The *BeppoSAX* satellite has a collection of instruments, including a  $\gamma$ -ray burst monitor, a wide-field imaging X-ray camera with a positional resolution of about 3 arcminutes, and a narrow-field X-ray camera with a position resolution of about 1 arcminute. Within 8 hours of the detection of the burst and its imaging with the wide-field camera, the narrow-field camera observed a source, consistent with the burst error circle, at  $\alpha_{2000} = 05^{\text{h}}01^{\text{m}}57^{\text{s}}$ ,  $\delta_{2000} = 11^{\circ}46'42''$  [50]. Optical and radio transients at the same position were quickly found [52, 159]. Some time later the optical transient was also seen by the Hubble Space Telescope [173]. The optical, radio, and X-ray sources were observed to decay as a power law consistent with the fireball blast wave theories of Mészáros and Rees [127] and Wijers et al. [210].

In the following months several other bursts would be found to be consistent with transient sources in other wavelengths. Another revelation came from GRB 970508,

observed May 8, 1997 by the wide-field camera on *BeppoSAX* and by its narrow-field camera 5.7 hours later. An optical counterpart was quickly found by Bond [17] and a radio counterpart found by Frail et al. [49] consistent with the narrow-field *BeppoSAX* position. Metzger and his colleagues at Caltech identified a set of absorption features implying a redshift of  $\geq 0.835$  [132]. By early June, they detected emission lines as well, at the same redshift [130]. For the first time since their discovery 30 years before, there was direct experimental evidence that  $\gamma$ -ray bursts were cosmological [131].

Another notable burst, GRB 971214 [67], was detected at a number of different wavelengths: optical [59], infrared [55], and ultraviolet [16], as well as being detected by a number of  $\gamma$ -ray and X-ray instruments including *BATSE*, *RXTE*, and *Ulysses* [95]. Absorption and emission lines have been detected from this burst as well, yielding a redshift measurement of 3.43—firmly establishing the cosmological nature of the  $\gamma$ -ray bursts [101]. Most recently, the redshift of the host galaxy of GRB 980703 has been measured at the Keck Observatory. Absorption and emission lines yield a redshift of  $z = 0.966$  [35]. A good review of the current state of observational affairs is given by Wijers [209].

Now that the observational mechanism for establishing  $\gamma$ -ray burst counterparts has been established, the field is changing rapidly. As of this writing, 11  $\gamma$ -ray bursts have been observed in radio and optical wavelengths [108]. These observations and others which will certainly be made in the near future have strongly affected, and will continue to affect, the leading theories of  $\gamma$ -ray bursts.

## 3.2 $\gamma$ -Ray Burst Models

Until the launch of *BATSE*,  $\gamma$ -ray burst theories outnumbered the bursts themselves. In light of the data provided by *BATSE*, *BeppoSAX*, and other satellites, it is worthwhile to examine the leading theories with an eye to understanding the consequences observable by *EGRET*. We will first look at the theories of the energy source powering  $\gamma$ -ray bursts, and then examine some of the theories of the  $\gamma$ -ray generating shock waves created by the bursting source.

### 3.2.1 Energy production mechanisms

Gigantic explosions hold fascination for the theoretical physicist as much as for the schoolchild. Cosmological  $\gamma$ -ray bursts require the largest explosions known, and thus attract theorists in droves (e.g., [60]). As long ago as 1975, Malvin Ruderman noted [172], “For theorists who may wish to enter this broad and growing field, I should point out that there are a considerable number of combinations, for example, comets of antimatter falling onto white holes, not yet claimed.” Mercifully, the considerable experimental data amassed since 1975 has largely narrowed the field to two general mechanisms: neutron star–neutron star mergers and massive stellar collapses known as “collapsars” or “hypernovæ.” Nevertheless, at this stage in our understanding of  $\gamma$ -ray bursts it is unreasonable to think that all theories could be placed in one of only two categories; these represent only the most prominent of the theories.

**Neutron star mergers.** The most popular theory at the time of this writing is the neutron star merger model [145]. The basic premise is very simple. Neutron star binary systems slowly lose energy as a result of gravitational radiation. Eventually, the neutron stars will spiral into each other, presumably resulting in a large release of energy. A variant of the model replaces one of the neutron stars with a black hole. Narayan [145] cites several advantages of such a model, as well as a number of issues to be resolved. First, the source population is known to exist. Neutron star binaries have been observed, and their energy loss corresponds with that expected from gravitational radiation to better than 1% [188]. Second, the energetics are of the right order. The energy release from such a merger would exceed  $10^{53}$  ergs in  $\sim 1$  ms within 100 km. Finally, the frequency of such mergers may be approximately right. Estimates of the merger rate include the range from  $10^{-6}$  to  $10^{-4}$  yr $^{-1}$  per standard galaxy, which matches the observed burst rate under a cosmological scenario and isotropic emission from the energy source.

An early objection to the neutron star merger model was the so-called “no host galaxy” problem. Optical observations of  $\gamma$ -ray burst error circles before the launch of *BeppoSAX* failed to find the galaxies expected as the hosts of the colliding neutron stars. However, it was realized that binaries can often acquire substantial recoil

velocities as a result of their two supernova explosions. For reasonable parameters, binaries may travel 1–1000 kpc before merging [201]. Therefore, by the time a binary neutron star system becomes a  $\gamma$ -ray burst, it may have left its progenitor galaxy. The diverse character of observed  $\gamma$ -ray bursts has been pointed out as a problem for the merger model. Neutron stars are expected to have a very narrow mass range. Merging binaries should almost always consist of about  $3 M_{\odot}$  collapsing in a very clean gravitational system. Such a homogeneous energy generation mechanism should result in a fairly homogenous population of  $\gamma$ -ray bursts, though beaming effects, magnetic fields, and an inhomogenous environment may explain the observed differences.

**Hypernovæ.** A much newer idea is the hypernova model due to Paczyński [158]. The idea is similar to Woosley’s “failed supernova” model [214]. A very massive star undergoes core collapse to form a  $\sim 10 M_{\odot}$  black hole. If the star is rapidly rotating, then the angular momentum of the star requires the formation of a rotating dense torus of material around the Kerr black hole. Any previously existing magnetic field will be significantly affected by the collapse; most possibilities strengthen the local magnetic field. Paczyński estimates that the rotational energy of the black hole should be of order  $10^{54}$  ergs. He also finds that the maximum rate of energy extraction is

$$L_{max} \approx 10^{51} \text{ ergs s}^{-1} \left( \frac{B}{10^{15} \text{ G}} \right)^2 \left( \frac{M_{\text{BH}}}{10 M_{\odot}} \right)^2 \quad (3.1)$$

Achieving the required energy release requires fields on the order of  $10^{15}$  G. No mechanism for generating such fields is offered, although many theorists are currently working on the details of the effects of the core collapse on the ambient magnetic fields.

The observed spectrum from either model of  $\gamma$ -ray bursts depends more on the details of the fireball model discussed in the next section than on the energy generation mechanism. The primary difference between these mechanisms is their location. While neutron star mergers are often expected far from galaxies, hypernovæ are found in star-forming regions, since their progenitors are rapidly evolving massive stars. The lack of optical observation of GRB 970828, despite fairly deep searches, combined with

the reported large hydrogen column density [142] has led Paczyński to conclude that the optical emission was not observed due to extinction by dust.

A substantial number of detections of  $\gamma$ -ray bursts at multiple wavelengths should illuminate this question in the very near future.

### 3.2.2 Blast wave theories

While very early experiments seemed to detect thermal radiation from  $\gamma$ -ray bursts, better instruments soon observed a characteristic power law emission in the X-ray and  $\gamma$ -ray regime. Theoretical explanations have centered on the blast-wave model, where the injection of a large amount of energy into a very small volume leads to an expanding fireball, optically thick to pair production, expanding into some surrounding medium. The simplest model—also due to Paczyński [157]—assumes the spherical expansion of an optically thick  $e^-e^+$  plasma with no surrounding medium. This model results in a blackbody spectrum. A series of more and more complicated models were based on this simplistic one, finally culminating in the model of Mészáros, Rees, and Papathanassiou [128], which calculated spectra expected for a variety of magnetic field configurations and particle acceleration efficiencies, including the shock fronts and reverse shocks which arise from the expansion of the burst ejecta into the surrounding medium.

Shock fronts in blast waves have become the baseline from which various energy generation mechanisms diverge. Their popularity stems from their success: they can naturally explain how energy can be reconverted into  $\gamma$ -rays from the particles that must emerge from the fireball, they can naturally explain the observed burst time scales, and, assuming the medium into which the fireball expands varies slightly from burst to burst, they can explain the wide variety of burst profiles and time scales observed [165, 204]. The observed afterglows may be explained as emission from the slowing, cooling shock [205, 203]. However, several theoretical issues remain. The mechanism of particle acceleration in relativistic shocks is not well understood, though it is widely assumed that such acceleration results in a power law energy

spectrum [6]. The magnitude and nature of the magnetic field is unknown. Pre-existing magnetic fields, if sufficiently strong, will provide significant synchrotron radiation in the particle blast wave. In addition, turbulent mixing in the shock can generate significant fields due to charge separation. Finally, the coupling between electrons, baryons, and the magnetic field is not well understood. Energy radiation from electrons is very efficient, but most of the energy is in the baryons, or perhaps the magnetic field, which do not radiate their energy so readily. The nature of their coupling affects the total radiated power as well as the time scale of the radiation [28, 168].

While a detailed investigation of the various blast-wave models is beyond the scope of this work, a general overview is given, based on that found in Chiang & Dermer [28]. The burst begins with the deposition of  $10^{51}$ – $10^{55}$  ergs of energy in a radius of about 100 km. The nature of this energy is not known. It is assumed that most of this energy will be transformed into kinetic energy of baryons, which expand adiabatically. The baryons soon become cold; that is, the baryon speeds in the comoving frame of the bulk flow become sub-relativistic. The bulk Lorentz factor is then given by  $\Gamma_0 \simeq E_0/M_0 c^2$  where  $M_0$  is the rest mass of baryons.

As this sphere freely expands into the surrounding medium, it sweeps up material. A shock front begins to form. At some “deceleration radius”  $r_d$  the shell can no longer be approximated as freely expanding, and the bulk kinetic energy of expansion begins to be reconverted into internal energy of the baryons. This radius is the point at which the integrated momentum impulse of the swept-up matter equals the original baryonic rest mass:  $r_d^3 \approx (3/4\pi\rho\Gamma_0)M_0$  where  $\rho$  is the density of the surrounding material.

Predictions of what happens at this deceleration radius form the core of most blast-wave models. A function  $\Gamma(r)$  is derived which expresses essentially the rate at which baryonic kinetic energy is converted to radiation. Since cosmological scenarios require high initial  $\Gamma_0$  of order  $10^2$ – $10^3$ , much of the energy release in all scenarios is compressed into the first few tens of seconds in the observer’s frame. Nevertheless, models of the blast wave at the deceleration radius and beyond make predictions about the observed spectrum at various times as well as the observed burst time scales.

Given the recent evidence that  $\gamma$ -ray bursts really are cosmological in origin, the energy required for the fluences observed on Earth make some sort of fireball almost inevitable. Blast-wave models have qualitatively reproduced some aspects of  $\gamma$ -ray burst observations, and appear to be a promising theoretical road to pursue. However, it should be noted that blast waves as they have been described cannot be the whole story. In either the neutron star merger model or the hypernova model, there is a natural symmetry axis associated with the source. A symmetric blast wave then seems rather unlikely. Asymmetry in the blast wave will lead to beaming on some scale. Beaming will of course reduce the energy required per burst, but increase the rate at which the bursts must occur. It is not clear how beaming would affect the radiation produced by shock waves. The radiation reaching the Earth has already been beamed into a cone of order  $1/\Gamma_0^2$ . This tight beaming means that all of the  $\gamma$ -rays observed at the Earth are emitted from a very small piece of the blast wave; therefore, the amount of large-scale symmetry in the wave may be irrelevant to the spectrum observed.

### 3.2.3 Observable consequences

Without the compass of observations, we are doomed to drown in an ever-deepening sea of theories. Fortunately, the tools of the experimental astrophysicist are becoming more and more powerful. A number of X-ray satellites are currently operating, with more planned, which produce error boxes small enough to allow radio astronomers to bring their substantial instruments to bear. *GLAST* will revolutionize high-energy  $\gamma$ -ray astronomy in the next decade just as *EGRET* did in this decade. And new types of astronomy, previously relegated to science fiction or crackpot dreams, are beginning to provide useful data. Air Čerenkov detectors can localize high-energy  $\gamma$ -rays from a few hundred GeV up to many TeV to much less than a degree. Böttcher & Dermer calculate the high-energy emission from proton synchrotron radiation and photopion-induced pair cascades, and find that future high-sensitivity Čerenkov telescopes with low energy cutoffs (or, it should be noted, good very-high energy response

from *GLAST*; see Chapter 6) could measure the level of the infrared background radiation [18], since high-energy  $\gamma$ -rays will interact with the infrared background to produce electron-positron pairs. While no current neutrino detectors have sufficient sensitivity, a measurement of the neutrino flux from a  $\gamma$ -ray burst could shed light on the energy generation mechanism [206]. Additionally, an intense gravitational collapse will produce gravitational waves, which could be detectable with the detectors currently under construction [99].

### 3.3 *EGRET* observations

While *BATSE* has enjoyed the spotlight for most of the contributions of *CGRO* to the  $\gamma$ -ray burst problem, *EGRET* has made some important observations as well. At least 16 bursts occurred outside the field of view of the spark chamber, but were nevertheless detected in the calorimeter [22, 103, 177]. Five  $\gamma$ -ray bursts have been detected in the *EGRET* spark chamber [34]. Each has characteristics worthy of some examination.

The first burst detected in the *EGRET* spark chamber occurred on May 3, 1991. Six photons were detected in the spark chamber in two seconds, coincident with the signal received from *BATSE* [176]. Measurements of the background before the burst suggested that 0.18 photons per two seconds were expected in the spark chamber. Additionally, the burst was evident in the TASC calorimeter data, as well as the anticoincidence trigger rate. The anticoincidence dome is sensitive to photons above about 20 keV via Compton scattering, while the TASC has four triggering levels, corresponding approximately to energies above 1.0 MeV, 2.5 MeV, 7.0 MeV, and 20.0 MeV. Firm detection of this event with all three systems, coincident with the *BATSE* trigger not only demonstrated  $\gamma$ -ray burst detection with *EGRET* but also measured the first  $\gamma$ -ray burst emission above 100 MeV: one of the spark chamber photons had an energy of approximately 230 MeV.

The next burst was detected a month later, on June 1, 1991 [103]. This burst was also seen in the TASC and anticoincidence dome, and four photons were detected in the spark chamber when 1.5 background photons were expected. The detection of



high-energy photons from these bursts began to shift the evidence toward power-law emission instead of thermal emission. Furthermore, the last photon to arrive in the spark chamber was nearly 70 seconds after the initial *BATSE* trigger.

Buffalo Bills quarterback Jim Kelly remembers January 31, 1993 as the day the Bills lost their third consecutive Super Bowl, this time to the Dallas Cowboys by a score of 52–17. High-energy astrophysicists worldwide remember that date for the detection of what still stands as the most intense *BATSE* burst ever seen [100]. *BATSE* count rates exceeded  $2 \times 10^6$  counts  $\text{s}^{-1}$ . Significant structure to the burst was observed at scales below 10 ms, and the first intense spike lasted 200 ms. Fortunately, the burst was in the field of view of the *EGRET* spark chamber, which detected 16  $\gamma$ -rays (compared to 0.04 expected by chance) in 25 seconds [181]. Two of the  $\gamma$ -rays had energies of nearly 1 GeV. *EGRET* measured a power-law photon spectrum with index  $\sim -2$ . The hard photon spectrum lent further credence to shock acceleration models, although the high-energy photons were taken as evidence that the burst was closer than  $\sim 50$  pc. A total fluence measurement could not be made by *EGRET*, since the dead time per spark chamber event is approximately 100 ms. It is likely that a number of high-energy  $\gamma$ -rays passed through the spark chamber in the first 100 ms.

It would be more than a year before *EGRET* would detect another burst, but that burst would provide plenty of fuel for the raging  $\gamma$ -ray burst debate. The burst, which arrived on February 17, 1994 and whose initial pulse lasted for 180 s, was detected by *COMPTEL* [96], *Ulysses*, *BATSE*, and *EGRET*. Of primary theoretical importance was a single *EGRET* photon, detected some 4500 s after the initial burst, with an energy of 18 GeV [76]. The probability of this photon originating in the background was  $5 \times 10^{-6}$ . In fact, *EGRET* detected a total of 28 photons from GRB 940217. Ten photons were detected during the first 180 s, concurrent with the *BATSE* detection, including a 4 GeV photon and a 3.5 GeV photon. The remaining 18 photons were detected over the next 1.5 hours. Hurley et al. [76] point out a number of conclusions which can be immediately drawn. While the universe is optically thin at  $\gamma$ -ray energies, the cosmic microwave background becomes an efficient medium for  $\gamma$ - $\gamma$  pair production for sufficiently high  $\gamma$ -ray energies. For a 25 GeV photon, this

consideration limits the source to  $z < 5.5$ . To avoid attenuation from the intergalactic infrared background, the source distance is further limited to  $z < 2.5$ , ruling out early universe theories [4]. Finally, they note that if the spectrum of the first 180 s of GRB 940217 is extrapolated to 1 TeV, the predicted fluxes would be detected by air Čerenkov telescopes and the Milagro air-shower array. Unfortunately, bursts with such high-energy emission are evidently somewhat rare, and the fields of view of air Čerenkov detectors are quite small. Nevertheless, the current network of fast burst position detections may allow observation of delayed emission like that of the February 17 burst. The very long delay of emission has also been the source of much theoretical speculation. The existence of such delayed emission is a natural consequence of blast-wave models. While the initial  $\gamma$ -ray burst is caused by the formation of a shock with the surrounding medium, the blast front will continue to radiate as it decelerates.

The most recent burst detected in the *EGRET* spark chamber arrived only a few weeks later, on March 1, 1994. This burst was similar to the first two which had been detected, with 7 photons of maximum energy 160 MeV, arriving within 20 s [177]. The spectrum of this burst was softer ( $\sim -2.5$ ) than the February 17, 1994 burst.

It is unlikely that any more bursts will be observed in the *EGRET* spark chamber, as instrumental lifetime concerns have reduced *EGRET* to Target of Opportunity observation only. Nevertheless, the observations made by *EGRET* create significant constraints on the models used to explain  $\gamma$ -ray bursts. The *GLAST* instrument, with its very wide field of view (§6.2) and large sensitive area up to very high energies (300 GeV), should further constrain the high energy behavior of  $\gamma$ -ray bursts.

### 3.4 Possible *EGRET*-only Bursts

Observations of  $\gamma$ -ray bursts in the last decade have shown conclusively that the high-energy emission has a power-law spectrum. If, for some bursts, the burst has a harder spectrum than the background, the signal-to-noise ratio should increase at higher energies. Some blast wave theories predict that a spectral break may occur at or just below *EGRET* energies [33]. In such models, the total peak spectral power early in the burst is emitted above 100 MeV.

It is thus possible that some  $\gamma$ -ray bursts will be detectable by *EGRET*, but not by lower-energy instruments such as *BATSE*. The evidence of such bursts would therefore be lurking in the *EGRET* photon database. As was discussed in §2.3, the best way to deal with the photon-by-photon nature of *EGRET* data is through the use of likelihoods. Buccheri et al. [20] developed a likelihood method to search *EGRET* data for  $\gamma$ -ray bursts. While they did find the known bursts in the data they searched, they apparently did not perform a comprehensive search of the *EGRET* database. The difficulty with such a search is that the exposure for each photon has to be calculated individually. This process is very time-consuming, due to the extended nature of the *EGRET* calibration files. Therefore, a comprehensive search required some adaptation of statistical methods [87]. Those methods, and their results, will be described below.

### 3.4.1 Statistical Methods

The  $\gamma$ -ray burst search algorithm was designed to be fast and efficient at finding bursts. From a statistical standpoint, a burst may be defined as a time interval with a measured rate which is, to some specified confidence, incompatible with Poisson fluctuations. The method, then, is fairly straightforward: first, find the background rate; second, find any time intervals with sufficiently high rates to rule out Poisson fluctuations at the given confidence level; and finally, verify that the spatial distribution of the photons is consistent with a point source. The sequential nature of this method makes it fast compared with a full likelihood analysis; however, it also involves some binning, and as we will see, complicates our estimates of the significance of detections.

To further speed the algorithm, we search for significant intervals in two steps. The first compares photon arrival rates only. The rate is defined as the number of photons from some area on the sky per second. It requires only the amount of instrument live time and a photon count. The second step will measure the photon fluxes (photons  $\text{cm}^{-2} \text{s}^{-1}$ ). This is certainly the more physically relevant quantity, but it is also computationally more expensive to determine the state of the *EGRET*

instrument for the entire interval. Therefore, promising candidate intervals will be found by comparing rates, and then checked for significance by comparing fluxes.

To establish a background rate, the field of view is binned into  $5^\circ \times 5^\circ$  squares. All photons in the viewing period with energies over 100 MeV and zenith angles less than  $100^\circ.5$  are sorted into these bins. The total instrument live time to the center of each square is calculated. This yields an array of approximate background count rates. The critical number of photons required for a significant interval,  $N_{crit}$ , is given implicitly by the Poisson formula

$$\alpha = \sum_{n=0}^{N_{crit}-1} \frac{e^{-\mu t} (\mu t)^n}{n!} \quad (3.2)$$

where  $\mu$  is the average rate,  $t$  is the time interval being searched, and  $\alpha$  is the confidence level. The probability of observing  $N_{obs} > N_{crit}$  is  $1 - \alpha$ .

To acquire a set of candidate events while avoiding specific time binning, each photon is considered to be the start of an interval. All photons arriving within the standard interval length (either 1 hour, 30 minutes, 10 minutes, or 3 minutes) and within  $5^\circ$  of the initial photon are considered part of the same event and counted. If the number of observed photons exceeds  $N_{crit}$  for that area of the sky, the candidate event is accepted for further evaluation.

Because the number of candidate events which pass the first cut is relatively small, it is practical to calculate instrument exposure and compare the candidate flux to the expected background flux. The single trial probability of such an event,  $P_S$ , is calculated as in equation (3.2), with the time  $t$  replaced by the exposure  $\mathcal{E}$  and the rate  $\mu$  replaced with the flux.

Unfortunately,  $P_S$  cannot be interpreted as the probability that the flux in a given interval is not a Poisson fluctuation. In fact, we have searched many different intervals, and the appropriate confidence level must take into account the number of trials. If the intervals had been fixed and preselected so as not to overlap, then each interval would be statistically independent. The total probability  $P_N$  that a given flux could not be attributed to Poisson fluctuations would be given by the complement of

the product of the chances that it would not be seen in each of any one interval:

$$P_N = 1 - P_S^N \quad (3.3)$$

where  $N$  is the number of independent trials.

However, preselecting non-overlapping time bins would not be a good way to search for  $\gamma$ -ray bursts. If a burst did not happen to fall entirely within one bin, but instead split its flux between two bins, it would probably not be significant in either bin. The sliding interval described above was designed to avoid this problem. Nevertheless, the sliding interval introduces its own problems: namely, that the intervals are no longer independent.

In order to evaluate the actual significance of an interval  $P_T$  as a function of  $P_N$ , a Monte Carlo simulation was performed. It was expected (and verified) that the significance of an interval should be monotonic in  $P_N$  (Figure 3.2). Approximately  $5.7 \times 10^8$  simulated photons were generated for the Monte Carlo data set; the actual data set searched contained  $1.2 \times 10^6$  photons. Each Monte Carlo photon was assigned an arrival time, drawn from a Poisson distribution with a given background rate. Each photon was also assigned a uniformly distributed  $x$  and  $y$  coordinate between  $0^\circ$  and  $40^\circ$ , simulating *EGRET* field of view. The data were simulated using actual *EGRET* exposure information calculated for a typical point on the sky over many viewing periods, yielding an exposure set representative of the windowing and non-continuous exposure actually obtained with *EGRET*. This exposure set was used as many times as necessary to generate the entire Monte Carlo data set. To determine appropriate background rates, 104 actual fluxes were measured from random points in differing viewing periods. These fluxes were sorted, and the highest and lowest 20% were discounted in order to exclude nonrepresentative outliers. The range of this tightened distribution of fluxes was used as the range for the uniformly distributed fluxes in the Monte Carlo simulation. This was done to ensure the use of typical, though not rigorously representative, background fluxes. Since all probabilities are found from the difference between measured and expected fluxes, they depend only

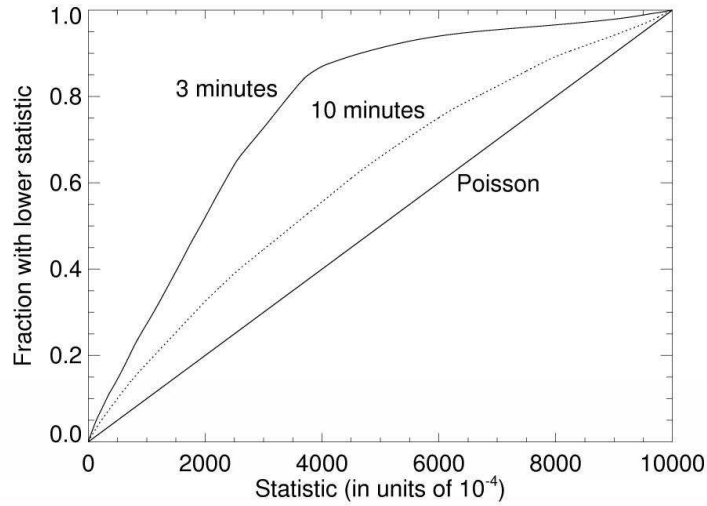


Figure 3.2: Overall significance  $P_T$  versus raw probability  $P_N$  from the Monte Carlo simulations.  $P_N$  is calculated for each Monte Carlo event from equation (3.2) and equation (3.3). A cumulative count of the Monte Carlo events yielding such a  $P_N$  yields the cumulative probability of that events,  $P_T$ , given by the vertical axis.

weakly on the precise values of the background fluxes. The range of backgrounds found was  $7.0 \times 10^{-7}$ – $4.8 \times 10^{-6}$  photons  $\text{cm}^{-2} \text{s}^{-1}$  for a  $5^\circ$  circle on the sky.

In some cases, the search algorithm may have detected the same event more than once; that is, the interval following the first photon in the event yielded a significant rate increase, and the interval following the second photon also yielded a significant rate increase. In these cases, the two probabilities must be independently combined, because the Monte Carlo distribution was found by counting all significant events, regardless of whether or not they were part of the “same” event.

In addition to exhibiting a flux increase,  $\gamma$ -ray burst photons should be statistically consistent with a point source origin. Candidate bursts found in the time series analysis were examined spatially using a likelihood analysis technique [36]. Likelihoods were calculated for all photons within approximately  $20^\circ$  of the first photon of the interval. A null model of smooth background was compared to a model with a variable position point source plus a background rate taken to be the average background found above. To simplify computation, errors in photon position were taken from the width of the energy dependent best fit Gaussian containing 68% of the *EGRET*

point-spread function given by equation (1.1). The usual *EGRET* test statistic is then defined [117] as in §2.5:  $TS \equiv -2(\ln \mathcal{L}_s - \ln \mathcal{L}_n)$ , where the  $\mathcal{L}_s$  and  $\mathcal{L}_n$  are the likelihoods of the source and null models, respectively. The spatial analysis required likelihood calculation for each individual photon. The standard *EGRET* likelihood software, *LIKE* [117], is designed to evaluate likelihoods based on maps of photon counts. Separate likelihood software was thus developed for this study. Simplifications in this implementation make direct comparison of these values of TS with those from *LIKE* inexact. For the purposes of source detection in *EGRET* analyses, a TS of 16 is considered to be a significant ( $4\sigma$ ) detection. This is based on the measured distribution of TS. However, the likelihood statistic calculated here suffers from a very low count rate; often the likelihoods are computed from less than 10 photons. The statistics of TS with very few counts are not well characterized. Furthermore, the background rate across the whole  $20^\circ$  is taken to be the same as that found for the central  $5^\circ$  circle. In regions where the background is spatially varying, this may distort the measured TS.

Nevertheless, the TS measurement adds valuable information to the evaluation of burst candidates. Candidates with a very low TS, corresponding to little or no point-like structure, should be discarded. A sharp variation in photon arrival rate across a large area of sky is probably not due to an astrophysical process. It should be remembered that there is already a selection effect of candidate events due to the fact that the time series analysis considers photons confined to a five degree circle. This selection effect as well as the low count statistics make translation of TS into a confidence level problematic. Note also that the spatial and time series probabilities are not completely independent.

### 3.4.2 Results

We analyzed 182 viewing periods using these methods, corresponding to observations between 1991 April 22 and 1996 March 21. Viewing periods after this time used new instrument modes to compensate for various instrument malfunctions and narrow-field viewing. This data was not searched, since the field of view was significantly

<i>Date</i>	<i>Time</i>	$\ell$	$b$	TS	<i>Number Expected</i>	<i>Number Observed</i>	<i>Max Energy (MeV)</i>	$P_T$
1993 Jan 31	18:57:12	287	51	33.1	0.048	6	1240	>99.994%
1994 Feb 17	23:03:05	152	-55	18.8	0.074	5	3382	98.8%
1994 Apr 27	01:31:01	121	-0.7	26.7	0.120	6	680	95.4%
1993 Mar 17	06:40:42	65	21	17.1	0.009	3	361	52.2%
1992 Oct 8	04:35:04	201	31	15.7	0.047	4	508	32.9%
1991 May 4	05:16:33	204	13	18.7	0.011	3	960	29.0%

Table 3.1: Three minute time scale results. Burst candidates are listed with their times (UT), galactic coordinates  $\ell$  and  $b$  of the maximum likelihood position, spatial TS, expected and observed numbers of photons, highest photon energy, and significance, as derived from the Monte Carlo simulations.

<i>Date</i>	<i>Time</i>	$\ell$	$b$	TS	<i>Number Expected</i>	<i>Number Observed</i>	<i>Max Energy (MeV)</i>	$P_T$
1993 Jan 31	18:57:12	287	51	33.1	0.160	6	1240	99.85%
1993 Jul 20	07:07:55	121	42	23.2	0.097	5	878	74.0%
1993 Feb 22	06:46:44	20	-52	21.8	0.099	5	615	72.2%
1992 Mar 22	08:25:50	333	0.4	29.6	0.623	8	11100	28.1%

Table 3.2: Ten minute time scale results, as in Table 3.1.

smaller, and the systematics of the new modes are not as well understood. Each viewing period was searched on four time scales: one hour, 30 minutes, 10 minutes, and 3 minutes. Results are presented in Tables 3.1—3.4. In each table,  $P_T$  is the probability that no such events would be detected in the entire *EGRET* data set for that time scale in the null hypothesis. All fluxes quoted below are found by dividing the number of photons by the total exposure in the scale time, even if the photons evidently arrived in a much shorter time. For events with very few photons, the flux is not very well defined, since an arbitrary change in cutoff time may reduce the exposure without changing the number of photons. Thus, the flux for the purposes below is always found by considering all of the exposure in the period.

Two of the bursts triggered by BATSE, the Super Bowl Burst of 1993 January 31 and the 1994 February 17 burst, were also independently detected with this algorithm. The other three *EGRET*-detected BATSE-triggered bursts were not strong enough to be independently detected. For comparison, these bursts and their characteristics are listed in Table 3.5. Several independent detections were made, the most significant occurring on 1994 April 27.



<i>Date</i>	<i>Time</i>	$\ell$	$b$	TS	<i>Number Expected</i>	<i>Number Observed</i>	<i>Max Energy (MeV)</i>	$P_T$
1993 Jan 31	18:57:12	287	51	33.1	0.387	8	1240	97%
1993 Jul 20	06:50:45	120	42	28.8	0.205	6	880	77%

Table 3.3: Thirty minute time scale results, as in Table 3.1.

<i>Date</i>	<i>Time</i>	$\ell$	$b$	TS	<i>Number Expected</i>	<i>Number Observed</i>	<i>Max Energy (MeV)</i>	$P_T$
1993 Jan 31	18:57:12	287	51	33.1	0.387	8	1240	97%
1994 Apr 27	21:34:18	169	3	26.0	1.146	10	522	70%

Table 3.4: One hour time scale results, as in Table 3.1.

### 3.4.3 Discussion

Each  $P_T$  is the chance that measured photon arrival times are *not* due to random Poisson noise in the entire *EGRET* data set for that particular time scale. Thus, an event  $P_T = 90\%$  in the one hour time scale would be a spurious detection in 10% of the ensemble of possible *EGRET* data sets searched on a one hour time scale. However, four time scales have been searched. If each time scale were independent, this would be counted as four trials. But the same data were searched in each time scale, so the trials are not independent. Rigorous evaluation of the overall number of independent trials is problematic, and is not attempted for fear of producing meaningless results.

The calculated probabilities also do not take into account the photon energies. However, high energy photons are rarer than lower energy photons, so the arrival of a similar number of high energy photons would constitute a more significant event. If the detected bursts exhibited a plethora or paucity of high energy photons, the event energy spectrum would be expected to differ appreciably from that of the background. Because each event has too few photons to meaningfully determine a spectrum, a hardness ratio was calculated. All photons from all bursts in each time scale were collected, and a hardness ratio for the set was calculated. Even such a collection suffers from poor counting statistics, as evidenced by the large errors (Table 3.6). The hardness ratio is defined as the number of photons with energies greater than 300 MeV divided by the number with energies between 100 and 300 MeV. A typical background spectral index of 2.0 corresponds to a hardness ratio of 0.5. The measured

<i>Date</i>	<i>Scale</i>	<i>Number Expected</i>	<i>Number Observed</i>	<i>P<sub>S</sub></i>	<i>P<sub>T</sub></i>
1991 May 3	3 min	0.202	3	99.88%	$< 10^{-300}$
	10 min	0.672	5	99.93%	$< 10^{-300}$
	30 min	1.288	5	98.97%	$< 10^{-300}$
	1 hour	1.288	5	98.97%	$< 10^{-300}$
1991 June 1	3 min	0.396	4	99.93%	$< 10^{-300}$
	10 min	0.633	5	99.95%	$< 10^{-300}$
	30 min	0.633	5	99.95%	$< 10^{-300}$
	1 hour	2.064	9	99.97%	$< 10^{-300}$
1994 March 1	3 min	0.102	3	99.98%	$< 10^{-300}$
	10 min	0.333	4	99.96%	$< 10^{-300}$
	30 min	0.569	4	99.72%	$< 10^{-300}$
	60 min	0.569	4	99.72%	$< 10^{-300}$

Table 3.5: Known *BATSE*-triggered  $\gamma$ -ray bursts not detected independently by *EGRET* in each time scale. The expected and observed numbers of photons are given, along with the single trial probability  $P_S$  and the significance  $P_T$  as determined by the Monte Carlo.

hardness ratios are consistent with the background hardness ratios, implying that the  $P_T$  would not be significantly modified if energy information were taken into account.

All probabilities are dependent on the statistical distribution found from the Monte Carlo simulation. Thus, any possible factors which might make the Monte Carlo an imperfect simulation of the real data must be examined. Edge effects may slightly affect the final distribution, since the  $5^\circ$  circles drawn around photons near the edge of the region will reach past the edge. However, a short simulation was done in a  $20^\circ$  by  $20^\circ$  square, and the resultant distribution did not differ significantly from that calculated with a larger area, indicating that edge effects play a small part.

The Monte Carlo simulation also assumed spatially uniform exposure and background rate in order to make computation time reasonable. These assumptions will be poor only when the exposure or rate varies significantly over the  $5^\circ$  circle. Exposure generally varies smoothly, so this is probably a good approximation. The background rate can vary extensively if a strong point source is nearby, but the diffuse background

<i>Time Scale</i>	<i>Hardness Ratio</i>
3 min	$0.723 \pm 0.338$
10 min	$0.385 \pm 0.202$
30 min	$0.500 \pm 0.433$
1 hour	$0.500 \pm 0.306$

Table 3.6: Hardness ratios for each time scale. The hardness ratio is defined as the number of photons above 300 MeV divided by the number of photons between 100–300 MeV.

does not vary rapidly on this scale. Thus, we may need to worry about the distribution if events in the real data are detected near steady point sources; otherwise, the constant background approximation should be relatively good.

Spatial correlations must also be considered in the evaluation of burst candidates. Unfortunately, rigorous treatment of spatial correlations is fraught with difficulty. The maximum likelihood distribution is not well characterized for low counts. Furthermore, the  $5^\circ$  search radius used will select for spatially correlated events. It was hoped that spatial analysis would add significantly to our understanding of these events; unfortunately, because of these biases and correlations the spatial analysis has yielded little additional insight.

The most interesting candidate event is clearly the 1994 April 27 01:31 event in the 3 minute time scale. The significance of this event, while much lower than the *BATSE*-independent detection of the Super Bowl Burst, is almost as high as the *BATSE*-independent detection of the 1994 February 17 burst. This detection occurred while *EGRET* was in its most common, largest effective area mode. The Earth zenith angle to the event was  $\sim 40^\circ$ , well away from the horizon. It was observed  $27^\circ$  off the instrument axis. It thus seems unlikely that it is a spurious detection caused by pushing the operating envelope of the instrument. In addition to the six photons within three minutes of elapsed time classified as good events, there were seven additional events which were rejected by the standard *EGRET* data analysis for a variety of reasons. One of these generated too few sparks in the spark chamber, one had its vertex in the wall of the chamber, and the rest failed to produce an acceptable time of flight measurement. Estimated trajectories of these events

suggest that they originated from the same area on the sky as the good events. Although a precise calculation of the significance of these events is impossible, there appear to be more such events from that direction on the sky than would otherwise be expected.

The time interval corresponding to the 1994 April 27 candidate was examined in the 30 - 100 MeV range as well. No photons were detected during that period. However, *EGRET* sensitive area to this energy range is comparatively small, so that only 0.046 background photons were expected (compared to 0.120 in the 100 MeV and above range.) The TASC and anti-coincidence dome rates did not show a significant change in rate. With such small numbers, it is difficult to assess the significance of the lack of low energy photons.

Furthermore, a check was done of BATSE detections nearby. No trigger occurred at that time, although BATSE triggering was enabled. The last previous trigger occurred some 20 hours earlier.

No other bursts were detected so significantly. However, there were several less significant detections, making it worthwhile to consider the probability that at least one  $\gamma$ -ray burst has been detected. In the three minute time scale, the April 27, 1994 burst is fairly significant by itself. However, it is interesting to calculate the joint probability that all the events in each time scale are due to random Poisson noise. We will exclude the Super Bowl Burst and the February 17 Burst, since they are already known to be  $\gamma$ -ray bursts. Table 3.7 shows the joint probabilities in each time scale from the arrival time data. There is apparently some evidence for burst occurrence in the short time scales, with no significant evidence for occurrence in the half-hour and hour long time scales.

The detected candidate events were compared to the Second BATSE Burst Catalog to see if any coincident detections were made. With the exception of the bursts actually triggered by BATSE, that is, the Super Bowl and February 17 bursts, no coincidences were found.

While the Poisson error analysis may be encouraging, it is important to consider the contribution of systematic errors before coming to any conclusions. The search for  $\gamma$ -ray bursts by the method used is most sensitive to systematic errors in the

<i>Time Scale</i>	Probability
3 min	99.0%
10 min	94.8%
30 min	77%
1 hour	70%

Table 3.7: Joint probabilities of detecting all the marginal candidates in each time scale. While systematic errors could be responsible, there is apparently evidence for burst activity at or below the three minute time scale.

determination of background rates. If the background is consistently underestimated relative to the burst photons, many apparently significant events are not actually significant.

The most likely source of systematic errors in the background rate is the error in the estimate of the instrument exposure. A subtle point should be explored here. *EGRET* switches observing modes every few minutes. Each mode has a different amount of sensitive area to a given position on the sky, as well as a different field of view. Approximately 80% of the time *EGRET* is in the single mode with the largest field of view and sensitive area. In the limit that the instrument is always in the same observing mode, any exposure errors will cancel each other, since the error induced in the background flux will be exactly the same as the error induced in the burst flux. However, if the exposure error is different for each instrument mode, then a burst candidate detected in a rare mode might exhibit considerable systematic error.

The sensitivity of *EGRET* diminishes as the gas in the spark chamber ages. This effect has been partially characterized and compensated for in the *EGRET* exposure data. The time scale for this drift is typically several months, much longer than the burst search scales and also at least twice as long as the longest background averaging time.

The nondetection of the 1994 April 27 candidate burst by BATSE must be considered in light of current models for  $\gamma$ -ray burst production. The relativistic fireball model of Mészáros, Rees, and Papathanassiou [128] suggests the possibility of a high energy flat spectrum tail. If the spectrum is flat down to the BATSE energy range, the signal would be lost in the soft-gamma background. However, that model does

not predict a flat spectrum at BATSE wavelengths. Significant redshift effects might move the break of the fireball model spectrum to below BATSE energies, but then x-ray detection would be expected. Nevertheless, other models [33] suggest that at the earliest times after the burst, the spectral break could be at *EGRET* energies.

### 3.5 Conclusions

The mystery of the  $\gamma$ -ray bursts has recently experienced its third major revelation. The first occurred in the late 1960s and early 1970s, when the energetic bursts were discovered. The next occurred in 1992, when *BATSE* made clear the isotropic, non-homogeneous distribution of the bursts—pointing to the almost inconceivable conclusion that the bursts were of cosmological origin. The third was the association, first by *BeppoSAX*, and then by many others of a few bursts with counterpart afterglows in many wavelengths, resulting in the measurement of cosmological redshifts.

One of the outstanding questions about  $\gamma$ -ray bursts has thus been answered. Nevertheless, we are far from a complete understanding of the burst mechanism. The central engine is probably either a merger of neutron stars or a hypernova. Energetic concerns suggest fairly strongly that the initial energy release goes into baryonic kinetic energy, and that the observed burst is radiation from a shock front created when the outflowing baryons sweep up surrounding material. The existence of shock fronts suggests high-energy power law emission, but the exact mechanism is still unknown.

Given the uncertainty of the field, it was judged prudent to examine the *EGRET* data for the presence of  $\gamma$ -ray bursts not detected in other wavelengths. One possible detection of a high-energy  $\gamma$ -ray burst event has been found in *EGRET* data independent of a trigger from *BATSE*. Two previously detected  $\gamma$ -ray bursts were independently detected, verifying the search method. The new event, occurring on 1994 April 27, was detected with a statistical significance of 95.4% on a 3 minute time scale although this does not include systematic errors. Pointlike structure and the presence of several additional photons which converted in the walls of the *EGRET* instrument lend qualitative support to the detection.

Taken together, several less significant events suggest burst activity on the three minute time scale with probability 99.0%. Activity is suggested at a somewhat lower probability on the ten minute time scale, and at significantly lower probability on thirty minute and one hour time scales.

## Chapter 4

# Periodic Time-Series Analysis

The full-sky map of the  $\gamma$ -ray sky that *EGRET* made in its first year of operation provided unprecedented discovery and localization of  $\gamma$ -ray sources (Table 1.1). However, *EGRET* also provides excellent arrival time information about individual photons. Combined with good directional information, this timing data can be used to look for coherent periodic variation. Six pulsars have been positively identified in *EGRET* data, and the precise rotation of pulsars makes them an obvious candidate for periodic analysis. X-ray binary systems also exhibit regular periodic behavior in the X-ray bands; it may be hoped that some of these could be detected by *EGRET* as well.

Since there have been extensive *EGRET* observations of pulsars, we will begin by looking at pulsar models for which *EGRET* (or *GLAST*) may have discriminating power, as well as the contributions made to pulsar understanding by *EGRET* so far. We will develop the necessary statistical apparatus to search for periodicity in a  $\gamma$ -ray signal. We will then see how to apply likelihood statistics to pulsar analysis, and the results of that analysis. Finally, we will see how the statistical tools for periodic time-series analysis may be applied to X-ray binary searches.



## 4.1 Pulsars

Two years before the Vela satellites would begin to secretly detect  $\gamma$ -ray bursts, Jocelyn Bell and Anthony Hewish detected a periodic radio signal that pulsed every 1.3 s [70]. The signal remained coherent for days at a time. However, the mysterious source of the signal would be divined before the  $\gamma$ -ray bursts would be declassified. The discovery of the Vela pulsar, with a period of 89 ms [106], and the Crab pulsar, with a period of 33 ms [183], would narrow the field of prospective sources to one: a rapidly rotating neutron star. Such an object is the only astrophysical object capable of radiating the power observed at the pulse frequencies observed without flying apart under its own rotation.

The basic description of the pulsar was worked out over the next few years. It had long been realized [24] that a sufficiently massive body would overcome its electron degeneracy pressure by self-gravitation. This situation can come about when a massive star ( $>M_{\odot}$ ) exhausts its nuclear fuel. Without the energy released by the fusion reactions in the core, the star collapses, the gravitational potential condenses the electrons and protons, and a central core of neutrons develops. The remaining outer material is blown off in a catastrophic explosion: the supernova. Conservation of some fraction of the original stellar angular momentum results in the central neutron star rotating with a frequency of 0.1–100 Hz. Conservation of the magnetic flux in the star (assuming it remains a perfect conductor) results in a magnetic field at the neutron star surface of order  $10^{12}$  G. The observed flux from pulsars, then, is the result of a rapidly rotating magnetic dipole (e.g., [43]).

Some basic pulsar parameters may be inferred from elementary mechanics. If we make the assumption that all radiated pulsar power comes from the rotational energy, then the power is given by the time derivative of the rotational energy  $\frac{1}{2}I\Omega^2$ , where  $I$  is the moment of inertia and  $\Omega$  is the rotation frequency. Converting this to the pulsar period and period derivative, we have

$$\dot{E} = (2\pi)^2 I \dot{p} / p^3 \quad (4.1)$$

Making some basic assumptions about a pulsar as a rotating dipole, Ostriker &

Gunn [153] find that the radiated power can be related to the magnetic field:

$$\dot{E} \simeq \frac{2}{3} \frac{B^2 a^6 \Omega^4}{c^3} \quad (4.2)$$

where  $B$  is the surface magnetic field and  $a$  is the radius of the pulsar (typically 10-15 km). Combining these two, we arrive at an estimate of the field strength in terms of the period and period derivative

$$B^2 = \frac{2}{3} (2\pi)^2 \left( \frac{c^3}{a^6} \right) I p \dot{p} \quad (4.3)$$

Typical values of pulsar parameters are given in Table 4.1. For any given pulsar, we assume that its radius and moment are constant. If we assume also that its magnetic field remains constant, we arrive at the differential equation  $p\dot{p} = k$  governing the pulsar's age. This equation is integrable, yielding

$$\frac{1}{2}(p^2 - p_0^2) = k\tau \quad (4.4)$$

where  $p_0$  was the pulsar period at time zero, and  $k$  is a constant formed from the parameters in equation (4.3). By convention, we assume that the final period is much larger than the initial period, and, solving for  $\tau$  above, designate the pulsar's characteristic age by

$$\tau = \frac{1}{2} p / \dot{p} \quad (4.5)$$

The characteristic age seems to be a reasonable approximation to the actual age for the only pulsar we can verify. The Crab pulsar was born in a supernova which was observed at Earth on July 4, 1054 [118, 197]. The Crab rotates with a period of  $\sim 33.39$  ms, and has a period derivative of  $\sim 4.21 \times 10^{-13}$ , yielding a characteristic age of about 1280 yrs. This is correct to within 30%, but the assumption of linear spindown is probably least accurate at very short times after the supernova explosion. This effect will diminish with pulsar age, while glitches in the pulsar period and its derivative will add error to our age estimate. One possible mechanism is gravitational wave emission due to mass multipoles [153]. Ostriker & Gunn find that to fully

Parameter	Typical Values
Period $p$	1.6 ms–6 s
Period derivative $\dot{p}$	$10^{-15}$ – $10^{-13}$ s/s
Magnetic Field	$10^{12}$ – $10^{14}$ G
Characteristic Age	$10^3$ – $10^6$ yr
Moment of Inertia	$\sim 10^{45}$ g cm <sup>2</sup>
Radiated Power $\dot{E}$	$\sim 10^{31}$ – $10^{34}$ erg s <sup>-1</sup>

Table 4.1: Typical pulsar parameters for  $\gamma$ -ray pulsars.

account for the age difference, approximately 1/6 of the Crab’s current luminosity would be in gravitational waves.

Some elementary physics gives a reasonable first approximation to a pulsar model. Nevertheless, physics is a fractal subject, and the number of questions still to be answered is seemingly independent of the number of questions already answered. Fortunately for *EGRET*,  $\gamma$ -rays turn out to be an excellent window on pulsar energy-generation mechanisms.

#### 4.1.1 *EGRET* Contributions

The *EGRET* instrument along with the other instruments on board the *CGRO* has revolutionized our understanding of at least one class of pulsars. Extensive reviews of those contributions [43, 46, 146, 152, 191, 194] have been published elsewhere; we will only review their highlights.

Six pulsars have been unambiguously discovered in high-energy  $\gamma$ -rays. All six share some common features. First of all, they tend to have double-peaked light curves, with the peaks separated by somewhat less than 180°.  $\gamma$ -Ray pulsars tend to have harder spectra than most sources (spectral indices range from  $-1.4$  to  $-1.8$ , compared to the average  $\gamma$ -ray source spectral index of  $\sim 2.3$ ). Five of the six have among the highest measured values of  $\dot{E}/D^2$ , the radiated power divided by the pulsar distance squared.  $\dot{E}/D^2$  should be proportional to the observed power at Earth. It may be calculated by assuming that all of the kinetic energy lost from the pulsar spin-down is radiated isotropically, and that the radio dispersion measure gives a good distance estimate to the pulsar.

The Crab pulsar was detected by both *SAS 2* [189] and *COS B* [8, 29] in  $\gamma$ -rays some ten years after its initial radio discovery [183]. It was strongly detected in many different *EGRET* viewing periods, yielding high quality light curves and spectra [151, 202, 43, 44]. All  $\gamma$ -ray pulsars are observed to have very steady luminosities; in fact, they have been used as constant calibration sources for some variability studies [121]. Early observers suggested, however, that the ratio of the luminosity in the two  $\gamma$ -ray light curve peaks of the Crab pulsar varied with a 14-year cycle [213, 155]. However, further observations ruled out significant variation on timescales of order 14 years [200].

When it was first discovered in radio observations [106], no one expected the Vela pulsar to be the brightest object in the  $\gamma$ -ray sky. Nevertheless, it was the strongest source detected by *SAS 2* [190], and remains the brightest steady source in the *EGRET* catalog [65]. Although there is significant timing noise (that is, the pulsar period fluctuates on short time scales), Vela is easily detected in a number of *EGRET* viewing periods [94].

The most fascinating  $\gamma$ -ray pulsar is Geminga. The third brightest object in the  $\gamma$ -ray sky after Vela and the Crab, it was unique when discovered by *SAS 2* in 1975 in that it had no obvious counterpart in other wavelengths [98, 40]. Most notably, it had no radio counterpart—a prominent feature of all other known pulsars. It would be 17 years before pulsation was discovered in the X-ray emission [58]. Using the X-ray ephemeris, pulsation was quickly detected in *EGRET* [11], *SAS 2* [114], and *COS B* [13] data. Indeed, the  $\gamma$ -ray signal is so strong that various period searching techniques would have independently discovered the pulsation in Geminga without the aid of an X-ray ephemeris (§4.2.3, [116]). Recently, there has been an unconfirmed report of pulsation detected in radio [102]; whether or not this detection can be confirmed, the radio emission is clearly very weak.

The remaining three  $\gamma$ -ray pulsars are less well-known, but no less important to our understanding (or lack thereof) of  $\gamma$ -ray pulsar physics. PSR 1706-44 was only discovered as a radio pulsar in 1992 [79] and soon thereafter in the *EGRET* data [192]. Unlike the other five  $\gamma$ -ray pulsars, which have two peaks separated by  $140^\circ$ – $180^\circ$  in phase, PSR 1706-44 exhibits a single peak in its  $\gamma$ -ray light curve.

Unexpected in its own way is PSR 1055-52. It was discovered as a  $\gamma$ -ray pulsar in *EGRET* data in 1993 [45], although it ranks approximately 29th in known  $\dot{E}/D^2$  [43]. Why PSR 1055-52 is observed when other, apparently more luminous pulsars are not remains a mystery. As a final confusion, PSR B1951+32—fourth in  $\dot{E}/D^2$ —was not observed as a pulsed source in *EGRET* Phase I. Further pointed observations in Phase III resulted in a weak pulsed signal [167].

*EGRET* observations of  $\gamma$ -ray pulsars pose a unique challenge for theorists. The small number of pulsars and the wide variety of observed behavior makes it difficult for any one model to match all the observations while remaining simple enough to make concrete predictions. Nevertheless, two main classes of models dominate the thinking of most pulsar theorists today.

### 4.1.2 Models

The theory and ramifications of  $\gamma$ -ray pulsar models are extensively discussed elsewhere [112, 43, 191]; we will review the highlights of the two major models. Most current  $\gamma$ -ray pulsar models may be categorized as either “polar-cap” or “outer-gap” models. These two classes differ mainly in the region where the energy is emitted.

#### Polar-cap models

The polar-cap models build on the early pulsar models of Goldreich & Julian [54], which defined the standard pulsar framework. Although many researchers have extended their work, Daugherty and Harding are largely responsible for developing the model for  $\gamma$ -ray emission [61, 32]. The “polar cap” is a region at the magnetic pole of the pulsar, which in general is not aligned with the rotation axis. Some magnetic field lines emerge from one pole and re-enter the pulsar at the other pole. However, since the pulsar is rapidly rotating, there is some radius (given by  $r = \Omega/c$ ) at which the field lines can no longer corotate with the pulsar without exceeding the speed of light. This radius defines the light cylinder. The closer the point from which the field line emanates is to the magnetic pole, the closer the field lines will approach the light cylinder. Field lines which emanate from within some critical radius will not return

to the pulsar; instead, they will close at infinity. The polar cap is that region around the magnetic pole inside the critical radius.

The polar cap is important because free charges placed on open field lines will escape to infinity. Potential differences across the polar cap can rip charge off of the pulsar surface. This charge then flows along the curved field lines, emitting curvature radiation. At the lowest altitudes above the pulsar surface, this curvature radiation is so energetic that it pair-produces in the magnetic field. Eventually, the charged particles have lost enough energy that the photons ( $\gamma$ -rays) no longer pair produce. These  $\gamma$ -rays are observed by *EGRET*. The details of the field shapes and the emission regions determine the  $\gamma$ -ray and radio light curves. Currently, it seems as if many  $\gamma$ -ray pulsar characteristics can be explained with the polar cap model. However, it has been suggested that general-relativistic frame-dragging effects may more strongly influence the  $\gamma$ -ray emission than the precise shape of the magnetic field [144, 143].

### Outer-gap models

A substantially different model of energy emission is the “outer-gap” model, first proposed by Cheng, Ho, & Ruderman [26, 27]. In these models, vacuum gaps may arise along the last closed field lines in the pulsar magnetosphere. The gaps separate charge of different sign on opposite sides of the last closed field line, causing significant electric potentials. Charged particles may be accelerated across these potentials, following the magnetic field and emitting curvature radiation. The details of the shapes of the emitting regions and the resultant light curves are not immediately obvious, but extensive work has been done to calculate the impact of the magnetosphere geometry on the  $\gamma$ -ray observations [171, 215]. The outer-gap models also seem to describe many of the qualitative features observed in  $\gamma$ -ray pulsars.

### Remaining Questions

It is still not clear which model of pulsar emission more accurately describes  $\gamma$ -ray pulsars. In general,  $\gamma$ -rays emitted from outer-gap regions will be emitted in a more fan-like pattern, while  $\gamma$ -rays emitted from polar-caps will be more tightly beams.

However, both models can reproduce a subset of the pulsar characteristics observed in *EGRET* data [152, 194, 44, 43].

Unfortunately, the sample of observed  $\gamma$ -ray pulsars is still small, and it is difficult to determine which observed characteristics are generally representative and which are particular to the observed pulsars. It is therefore critical to increase the number of observed  $\gamma$ -ray pulsars. The *GLAST* mission will bring a superior  $\gamma$ -ray telescope to bear on the problem (Chapter 6). However, it is possible that there are additional Geminga-like radio-quiet pulsars which have already been observed by *EGRET*. Our task is to find likely pulsar candidates, and determine their pulsation parameters.

## 4.2 Statistical Methods

Searching for pulsation in *EGRET* sources poses a unique set of problems to the pulsar researcher. Dispersion, the scourge of radio pulsar searches, is non-existent in  $\gamma$ -rays. However, since the flux is quantized into  $\gamma$ -rays, *EGRET* might detect a photon from a pulsar only once per thousand rotational periods. Long integrations of coherent pulsar emission are required to resolve the periodic behavior. Furthermore, the particular structure of *EGRET* data, organized by individual photon information, is significantly different than the flux information found in other wavelengths. Low count rates mean that the instrument state can vary significantly between the arrival of individual photons. The low rates also require that as much information as possible be extracted from each photon.

For these reasons, special statistical care must be taken in analyzing *EGRET* data for pulsar signals. Extensive coherent pulsation analysis has been already been done, and it will be instructive to examine the challenges specific to *EGRET* previously overcome (§4.2.1). First, however, we must approach some difficulties basic to all pulsation analysis.

In order to be sensitive to pulsed emission from the fastest pulsing sources known (a few milliseconds), we must have timing accuracy to a fraction of the pulse period. *EGRET* records photon arrival times to an absolute accuracy of 100  $\mu$ s, two and a half orders of magnitude smaller than the period of the Crab. However, the radius

of the Earth’s orbit is 8 light-minutes. Photons from source observations separated by six months time will have light travel times differing by hundreds of thousands of pulse periods. In order to compensate for the motion of the Earth, we will translate all measured arrival times into Solar System Barycenter (SSB) times. The SSB time is the time when a photon would have arrived at the solar system barycenter if none of the mass of the solar system were present. The conversion between measured time ( $t_{\text{UTC}}$ ) and barycenter time  $t_b$  has been worked out in detail elsewhere [43, 188]. The expression will be motivated and examined in Appendix A; the schematic result is:

$$t_b = t_{\text{UTC}} + \Delta_{\text{convention}} + \Delta_{\text{location}} + \Delta_{\text{Einstein}} + \Delta_{\text{Shapiro}} \quad (4.6)$$

where adjustments to Universal Time are made to correct for bookkeeping conventions such as leap seconds, for the current location of the spacecraft with respect to the barycenter, for the gravitational redshift (“Einstein delay”) effects, and for the delay due to the gravitational potential (“Shapiro delay”). The full result is given by equation (A.5).

### 4.2.1 Previous Methods

Two methods have been used to examine coherent periodicity in *EGRET* data. The first one, used for analysis of pulsars with known ephemerides, was implemented by Joe Fierro in a program called **PULSAR** [42]. **PULSAR** selects photons within an energy-dependent cone about the source position. The acceptance radius, chosen to maximize the signal-to-noise ratio, is given by equation (1.1). The pulsar period, along with the first and second period derivatives, are used to assign to each photon a *phase*, corresponding to the fraction of a rotation through which the pulsar has turned since a reference time  $t_0$ . Recall that a  $\gamma$ -ray will arrive, on average, only once per hundred or thousand rotations of the pulsar; by retaining only the fractional rotation, the emission from many rotations is added together coherently. This process is known as *epoch folding*. Plotting the resulting photon rate as a function of phase yields a light curve—the average profile of emission through a rotation. Photons can then be selected as a function of phase for further analysis.



The phase of a photon is determined from the pulsation period and its derivatives, as measured from some reference epoch:

$$\phi(t) = \phi(t_0) + \nu(t - t_0) + 1/2\dot{\nu}(t - t_0)^2 + 1/6\ddot{\nu}(t - t_0)^3 + \dots \quad (4.7)$$

where  $\nu = 1/p$  is the pulsation frequency and  $p$  the period. In practice, it is only rarely that the second-derivative term of the Taylor expansion is important; higher orders are negligible. The constant term in the expansion is kept only to allow  $\gamma$ -ray light curves to be compared with radio light curves.

Of primary importance in such an analysis is the determination of the presence of intensity modulation at the known frequency. Ephemerides for radio pulsars have been collected into a database stored at Princeton University [187].  $\gamma$ -Ray photon phases based on these ephemerides may be tested for periodicity.

### The $\chi^2$ test

The simplest test is the  $\chi^2$  test. Photons are sorted into  $m$  bins, based on their phase. Since photon count statistics are distributed as a Poisson, the variance in the number of photons in each bin is  $N_m$ , the number of photons in the bin. The usual  $\chi^2$  statistic is calculated, and the probability of the observation under the null model is computed. A sufficiently low probability of observation under the null model is taken as evidence for variability. While this method is simple, it has a number of undesirable aspects. First, the significance of the detection depends strongly on accidents of bin boundaries—a problem inherent to binning schemes. Second, the  $\chi^2$  is invariant under permutations of bins. We expect pulsar light curves to smoothly vary, with one or two main peaks, and would like our statistical method to have some power to identify such light curves.

### The $Z_m^2$ test

The  $Z_m^2$  test was developed to try to address some of these difficulties [9, 21, 43]. The basis of this test is the realization that the light curve is well represented by the phase density  $f(\phi)$ , which is the fraction of the integrated intensity in each  $d\phi$ . In

its simplest form, corresponding to  $m = 1$  and known as the Rayleigh statistic [113], this phase density will be compared to a sinusoid of unknown amplitude and phase. The general form uses more terms of the Fourier expansion. The best estimate of the phase density function is a series of  $\delta$ -functions:

$$f(\phi) = \frac{1}{N} \sum_{i=1}^N \delta(\phi_i) \quad (4.8)$$

We will define  $f_m(\phi)$  as the function composed of the first  $m$  Fourier components of  $f(\phi)$ . To calculate the  $Z_m^2$  statistic, we determine a comparison (or model) phase density function  $\tilde{f}_m(\phi)$ . We then find the squared difference from  $f_m(\phi)$  and  $\tilde{f}_m(\phi)$

$$Z_m^2 \equiv 2\pi N \int_0^{2\pi} [f_m(\phi) - \tilde{f}_m(\phi)]^2 d\phi \quad (4.9)$$

If we take the comparison density function to be constant, this is simply computed; it can be shown to be equal to  $2N \sum_{k=1}^m (\alpha_k^2 + \beta_k^2)$ , where  $\alpha_k$  and  $\beta_k$  are the even and odd Fourier coefficients from  $f_m(\phi)$ .  $Z_m^2$  is asymptotically distributed as  $\chi^2$  with  $2m$  degrees of freedom [7].

This approach clearly mitigates some of the problems with the  $\chi^2$  test. Primarily, photon binning has been eliminated. In addition, the Fourier decomposition expects a periodic signal—the degeneracy to permutation of flux peak location is removed. Unfortunately, the  $Z_m^2$  statistic has shortcomings of its own. The significance of a detection is a strong function of the number of harmonics chosen. It is not difficult to see why this should be the case. Retaining only  $m$  harmonics of a sum of  $\delta$ -functions amounts to smoothing the observed phase density function. Too much smoothing (a very small  $m$ ) washes out any signal that may be present. Too little smoothing (a very large  $m$ ) results in the signal being swamped by noise from the higher harmonics. To ameliorate this difficulty, another statistic was invented.

### The $H$ -test

In the quest to obtain more and more significant results, it naturally occurred to astrophysicists to try a variety of values of  $m$ , and see which one results in the most

significant value of  $Z_m^2$ . Fortunately, de Jager et al. realized that the set of  $Z_m^2$  obtained in this way would no longer be distributed as  $\chi_{2m}^2$ . At this point, there is no further guiding insight; an *ad hoc* limit of 20 is set on  $m$ , and the distribution of  $H \equiv \max_{1 \leq m \leq 20} Z_m^2 - 4m + 4$  is found from a Monte Carlo simulation. The inclusion of the term involving  $m$  favors models with fewer Fourier components, and the constant ensures that the statistic will be positive. This test has become the primary tool to search for a pulsed signal in *EGRET* data [43].

### Limitations of these statistics

Statistics for analyzing pulsar data have evolved, with each generation of statistics alleviating some of the problems of the previous generation, but creating problems of its own. The discussion of likelihood statistics in §2.3 sheds some light on why these difficulties arise. A full discussion of the application of likelihood statistics to this problem will be given in §4.2.2; here we will quickly examine the above statistical measures.

Since the  $H$ -test is the most sophisticated measure, we will focus on it. If we permit ourselves to use some Bayesian language, we see that the goal of the  $H$ -test is to eliminate the nuisance parameter  $m$ . The method is really to take  $H$  as a function of  $m$ , and maximize this  $H(m)$  with respect to  $m$ . Each  $Z_m^2$  has the form of the squared difference between the null model and a representation of the data comprised of  $m$  harmonics\*. This is just the logarithm of the likelihood of the “data representation,” assuming a null model and Gaussian errors of variance  $N_m$ . The constant term only insures positivity; clearly it does not affect the distribution of the statistic. The only remaining term contains an  $m$ . To see its significance, let us write the exponentiation of  $H(m)$ —that is, instead of the logarithm of the likelihood, the

---

\*Note that each representation, labeled by  $m$ , is derived from the data, which is not permitted in Bayesian analysis. Therefore, the likelihood formed is not “the likelihood of the data, given the model,” but “the likelihood of the representation, given the model.” Since the representation is a (lossy) smoothing of the data, we have no reason to expect a one-to-one relationship between the likelihoods. Nevertheless, the qualitative argument is still valid—this only means that multiplying the  $Z_m^2$  by a prior and integrating over  $m$  would still give incorrect numerical results.

likelihood itself.

$$\exp H(m) = \exp(Z_m^2 - 4m + 4) = (e^4 e^{-4m}) \exp \int [f_m(\phi) - \tilde{f}_m(\phi)]^2 d\phi \quad (4.10)$$

The integral is the likelihood; it is the exponential of a sum of squared differences, which of course is a Gaussian. The first term,  $e^{-4m}$ , is readily identified as the prior! The Bayesian would now integrate<sup>†</sup>  $H(m)$  over  $m$  to eliminate the unnecessary parameter  $m$  as described in §2.6.3. However, if  $H(m)$  is at all peaked as a function of  $m$ , then  $e^{H(m)}$  is even more peaked, and the integral of  $e^{H(m)}$  over  $m$  is very nearly equal to the maximum. The  $H$ -test, then, is an approximation to the integral over  $m$  of the likelihood times a prior of  $e^{-4m}$ .

This example makes the comparison of the frequentist and Bayesian schools quite explicit. The Bayesian makes arbitrary, subjective choices of priors. The frequentist makes arbitrary, subjective choices in the method of smoothing—for example, it is not clear that the basis of sines and cosines is the optimal smoothing for the  $H$ -test. The advantage to the Bayesian method is that it makes explicit when the subjective choices are to be made, and completely prescribes the rest of the analysis process.

As we have seen, the further disadvantage is that the scientist creating new statistics cannot always consider all the ramifications of his choices. Unfortunately, the  $H$  statistic cannot be easily adapted to a Bayesian analysis; for while  $Z_m^2$  may appear to be a true likelihood, it is not. The likelihood must represent the probability of the data.  $Z_m^2$  represents the probability of  $f_m(\phi)$ , which in general, does not have the same probability density as the actual data. Furthermore, it is not at all clear that  $e^{-4m}$  is the most suitable prior. If de Jager et al. had claimed to use such a prior, they would have had to spend some time justifying their choice. However, under the guise of creating an *ad hoc* statistic, they have surreptitiously inserted that prior into the analysis—probably fooling even themselves.

Is the  $H$ -test then worthless, or worse yet, misleading? No. Within the constraints of the simulations done to quantify its significance, and within the assumptions that it implicitly makes, it is completely valid. However, the likelihood approach offers a

---

<sup>†</sup>if only the  $Z_m^2$  were a well-formed likelihood.

method which is both simpler to understand, and at least as powerful. The correct generalization of the  $H$ -test will be discussed in §4.2.6.

### Fourier Transforms

The statistical tests described above have been used extensively in analyzing *EGRET* data, but have only had success when a pulsar ephemeris from radio or X-ray observations was used to find the photon phases  $\phi_i$ . The Geminga pulsar is the first known “radio-quiet” pulsar, with little or no radio emission despite a strong pulsed signal in X-ray and  $\gamma$ -ray observations [11, 120]. It is natural to search for other such radio-quiet pulsars in the *EGRET* data. A likelihood method of pulsar searching will be discussed in §4.3; here we will briefly touch on a Fourier transform method.

The traditional method of searching for periodic behavior at an unknown frequency is the fast Fourier transform (FFT). The main advantage of the FFT is its speed. Indeed, such an algorithm has been implemented to search for periodic signals from pulsar candidates [116]. It has been shown to be successful in detecting Geminga—although as we will later see, the signal from Geminga is so strong that this is not a definitive test. The drawbacks to the FFT are also significant. First of all, the FFT cannot detect a period derivative. Trial period derivatives must be removed from the photon phases, and a new FFT performed for each period derivative. The FFT also cannot naturally deal with noncontiguous variable exposure and backgrounds. In order to detect the weakest pulsar signals, we will need to identify, to the extent possible, the photons most likely to be source photons, and account for the instrument exposure on a photon-by-photon basis.

#### 4.2.2 Maximum Likelihood

The ideal statistical method for pulsed-signal analysis would be sensitive to variations in pulsed flux from the candidate source, rather than pulsed count rates in a region around the source. Given the success of the maximum likelihood method for spatial analysis (§2.4), it seems natural to apply likelihood to the problem of periodic signal analysis. Again, we will find that the mathematics may be interpreted in a maximum

likelihood framework or a Bayesian framework. Following a suggestion by Gregory & Loredo [56], we will generalize the binned  $\chi^2$  method to a maximum likelihood method. In §4.2.6 we will examine the possibility of generalizing an unbinned method.

The first thing we must do is to construct the likelihood—the probability of observing our data, given our model and the state of the instrument. Since the state of the instrument and the background are different for every photon, we first divide our time interval and spatial intervals into sufficiently small subintervals that there is either zero or one photon in each subinterval. We then have an array in parameter space of volume elements  $\Delta t \Delta \ell \Delta b$ . The probability that a given element has no photons in it will be the Poisson probability of detecting zero photons during a time  $\Delta t$  from a direction element  $\Delta \ell \Delta b$  with rate  $r(t, \ell, b)$ , which depends in general on time and observed position. The probability of detecting one photon follows similarly:

$$\begin{aligned} p_0(t, \ell, b) &= e^{-r(t, \ell, b) \Delta t \Delta \ell \Delta b} \\ p_1(t, \ell, b) &= r(t, \ell, b) \Delta t \Delta \ell \Delta b e^{-r(t, \ell, b) \Delta t \Delta \ell \Delta b} \end{aligned} \quad (4.11)$$

We identify each element in  $t$ ,  $\ell$ , and  $b$  with a sequential, unique label. Furthermore, let us suppose that  $N$  of these parameter-space volume elements contain one photon, and  $Q$  of them contain no photons.  $N+Q$  is then the total number of parameter-space volume elements, and  $N$  is the total number of photons. We may find the likelihood of this configuration by multiplying the probabilities of each element:

$$\mathcal{L} = \prod_{i \in \alpha_1} p_1(t_i, \ell_i, b_i) \prod_{j \in \alpha_0} p_0(t_j, \ell_j, b_j) \quad (4.12)$$

where  $\alpha_0$  is the set of  $Q$  volume elements with zero photons, and  $\alpha_1$  is the set of  $N$  volume elements with one photon. Plugging in our expressions from equation (4.11), we may factor out the exponential and arrive at

$$\mathcal{L} = (\Delta t \Delta \ell \Delta b)^N \prod_{i \in \alpha_1} r(t_i, \ell_i, b_i) \exp \left[ - \sum_{j=1}^{N+Q} r(t_j, \ell_j, b_j) \Delta t \Delta \ell \Delta b \right] \quad (4.13)$$

The sum in the exponential is over all volume elements. It is simpler to separate this

sum into three independent summations, one for each parameter. In the limit that  $\Delta t$ ,  $\Delta \ell$ , and  $\Delta b$  are very small, these sums become integrals. Now, the  $i$  are just arbitrary labels. We renumber the volume elements so that elements 0 through  $N$  contain one photon, and we have

$$\mathcal{L} = (\Delta t \Delta \ell \Delta b)^N \prod_{i=1}^N r(t_i, \ell_i, b_i) \exp \left[ - \int_t \int_\ell \int_b r(t, \ell, b) dt d\ell db \right] \quad (4.14)$$

Note that nowhere have we assumed that the  $\Delta t$  are contiguous. Thus, this likelihood expression is valid even if there are gaps in the data.

The rate  $r(t_i, \ell_i, b_i)$  is a function of both the source strength and background. We assume that the background is constant in time, and varies in space according to the standard *EGRET* gas map [10, 75]. The positional dependence of the source rate will be taken from the instrument point-spread function. We will thus take the rate to be

$$r(t_i, \ell_i, b_i) = A(t_i, \ell_i, b_i) \tilde{f}(t_i) + B(t_i, \ell_i, b_i) \quad (4.15)$$

where  $\tilde{f}$  is the time-dependent model source flux as before,  $A(t_i, \ell_i, b_i)$  represents the instrument response function, and  $B(t_i, \ell_i, b_i)$  is the background flux. We will worry about the detailed forms of  $A$  and  $B$  below; however, we note here that the time dependence of  $A$  and  $B$  is a result of the time dependence of the instrument sensitive area.

To simplify the products and exponents, we take the logarithm of the likelihood:

$$\ln \mathcal{L} = N \ln(\Delta t \Delta \ell \Delta b) + \sum_{i=1}^N \ln(A_i \tilde{f}(t_i) + B_i) - \int_\ell \int_b \int_t (A_i \tilde{f}(t_i) + B_i) d\ell db dt \quad (4.16)$$

where  $A_i$  and  $B_i$  are shorthand for  $A(t_i, \ell_i, b_i)$  and  $B(t_i, \ell_i, b_i)$ .

Now, eventually we will either maximize the likelihood, or find a ratio of likelihoods. Thus, constant additive terms in  $\ln \mathcal{L}$  may be dropped. We drop the first term and separate the integral to get

$$\ln \mathcal{L} = \sum_{i=1}^N \ln(A_i \tilde{f}(t_i) + B_i) - \int_{\ell} \int_b \int_t A(t, \ell, b) \tilde{f}(t) d\ell db dt - \int_t \int_{\ell} \int_b B(t, \ell, b) dt d\ell db \quad (4.17)$$

Although the last term is (implicitly) a function of source position, it will be constant for our purposes, as we take source position to be given. Since it is constant, we drop it. In the second term, we may split  $A$  into  $\text{PSD}(\ell, b)\text{SA}(t)$ , the point-spread density and the sensitive area. The point-spread function is normalized, by construction, for all times, and  $\text{SA}(t)$  depends only on the source position, not the photon positions. Therefore we may split the integral into

$$- \int_{\ell} \int_b A'(\ell, b) d\ell db \int_t \tilde{f}(t) \text{SA}(t) dt \quad (4.18)$$

The spatial integrals are normalized, and the resulting likelihood function is given by

$$\ln \mathcal{L} = \sum_{i=1}^N \ln(A_i \tilde{f}(t_i) + B_i) - \int_t \tilde{f}(t) \text{SA}(t) dt \quad (4.19)$$

Remember that  $\tilde{f}$  is the *model* source flux. It is this model that we will vary to find the model most likely to have produced our data. The data itself appears only implicitly in equation (4.19), in the  $A_i$  and  $B_i$ , and most importantly in the  $t_i$  at which the model flux is sampled.

### 4.2.3 Application to *EGRET*

We have not yet selected a functional form for  $\tilde{f}$ . It is tempting to follow the lead of the  $Z_m^2$  statistic, and let  $\tilde{f}$  be a function composed of some number of harmonics, perhaps with parameters to be determined. We will delay such an attempt to §4.2.6, and first develop a method based on  $\chi^2$  which we will find to be less computationally demanding.

The functional form of  $\tilde{f}$  that corresponds to  $\chi^2$  binning is stepwise constant, with  $m$  different steps. The immediate benefit of such a choice comes in the simplification



of the second term of equation (4.19):

$$\int_t \tilde{f}(t) \text{SA}(t) dt \longrightarrow \sum_{j=1}^m \tilde{f}_j \tau_j \quad (4.20)$$

where  $\tau_j$  is the sensitive area integrated over the livetime in bin  $j$ ; that is, the total exposure in bin  $j$ . Now equation (4.19) may be stated as a sum over bins

$$\ln \mathcal{L} = \sum_{j=1}^m \left[ \sum_{i \in \text{bin } j} \ln(A_i \tilde{f}_j + B_i) - \tilde{f}_j \tau_j \right] \quad (4.21)$$

Thus the maximum of  $\ln \mathcal{L}$  may be found by independently maximizing the  $\tilde{f}_j$  for each bin, instead of simultaneously maximizing all the parameters of  $\tilde{f}$ —an enormous computational savings.

The analysis is thereafter quite simple, and quite slow. A candidate pulsar is selected for analysis. All photons within some radius, usually  $15^\circ$ , are collected. Each photon with sufficient energy ( $>100$  MeV) which arrives from a position sufficiently far from the Earth's limb ( $<95^\circ$  from the instrument axis) during a valid instrument mode is accepted for analysis. For each of these photons, the arrival time is corrected to the Solar System barycenter, and the phase-independent likelihood factors  $A_i$  and  $B_i$  are calculated. For periods less than a minute, it may reasonably be assumed that the instrument exposure will be evenly distributed across the bins. For longer periods, such as X-ray binary orbital periods, all instrument exposure during the observation is calculated as a function of SSB time.

To ameliorate the primary objection to binning, namely, that the arbitrary placement of the bin boundaries may obscure a signal, we may allow an offset to the bin boundary. In practice, this means rebinning the data for a number of different boundary offsets. Of course, such an operation increases the number of trials.

### Sampling Density

A subset of parameter space is identified to be searched for pulsed signals. Some boundaries of the range of period and period derivative are set by the physics of the

system being examined; those will be motivated in §4.3 and §4.4. The sampling size required is determined by the statistics. To determine the number of steps required to sample the period space, we consider the difference in phase of the last photon in the observation as a function of the change in trial periods. If two trial periods differ by so little that the change in phase of the last photon as computed by equation (4.7) is less than the width of a bin, then the most likely  $f_j$ 's computed by maximizing equation (4.21) will be unchanged. So, we choose the minimum spacing so that the phase of the last photon will change by an amount of order the bin width, and calculate the number of steps to take in period across the desired range.

$$N_p = (\nu_{max} - \nu_{min}) m \delta t \quad (4.22)$$

where  $\delta t$  is the length of the observation. Note that a longer observation means more photons will be observed, increasing the signal-to-noise ratio, but the period space must be searched more densely.

Similarly, we can find the minimum period derivative we expect could make a difference. In this case, our condition is that  $\phi(\delta t) - \nu \delta t$  is an appreciable fraction of a bin. Neglecting higher derivatives, this happens when  $\frac{1}{2}\dot{\nu}\delta t \sim p/m$ . Since the frequency derivative  $\dot{\nu} = \dot{p}/p^2$ , we have

$$\dot{p}_{min} = \frac{2p^3}{m(\delta t)^2} \quad (4.23)$$

The maximum period derivative must be determined by the physics.

With the range of period derivatives for a given period in hand, we may compute the number of samplings in period derivative required. Again, we find the step size by equating the difference in computed phase with the bin size:

$$\frac{1}{2}\dot{\nu}(\delta t)^2 - \frac{1}{2}(\dot{\nu} + \delta\dot{\nu})(\delta t)^2 = 1/m \quad (4.24)$$

and thus the number of steps required in the period derivative:

$$N_{\dot{p}} = \frac{1}{2}(\dot{\nu}_{max} - \dot{\nu}_{min}) m (\delta t)^2 \quad (4.25)$$

### Significance Estimates

For each point in parameter space, the flux in each bin is estimated by maximizing the likelihood. Since the sampling of parameter space was chosen to make each point roughly independent, the number of points sampled in parameter space should be a good estimate of the number of independent trials. The significance is then the probability of measuring no likelihoods greater than or equal to that observed in the number of trials.

### Automated analysis with `timevar`

These methods have been automated into a tool for searching for periodicity in *EGRET* data called `timevar` [81]. Capable of running either interactively or in batch mode, `timevar` searches a given region of parameter space, for a given number of bins. It maximizes the likelihood for each period and period derivative, and reports the significance of the most likely period and period derivative. In addition, it yields a light curve, both as the most likely flux in each bin, and for comparison with `PULSAR`, the number of photons within the 68% containment radius in each bin.

To demonstrate the capabilities of `timevar`, we examine the Geminga pulsar. We will check viewing period 413.0, corresponding to observations between 7 March 1995 16:44:00 and 21 March 95 14:08:39. A small range around the known period was searched, and the results are presented in Figure 4.1. The light curves are shown in Figure 4.2. The probability of the observation in the null model is less than  $10^{-25}$ .

The great advantage of `timevar` over previous analysis methods is that it combines period and period derivative searching ability with a proper likelihood treatment of the source and background as perceived through the instrument point-spread function and sensitive area. `PULSAR` has been useful to examine known pulsars with radio ephemerides, although it does not optimally use the point-spread and background information about each photon. The disadvantage to `timevar` is its computational expense. Examining a single pulsar candidate over a reasonable range of period and period derivatives currently takes on the order of months of continuous running on a Sun Microsystems Sparc 10. Mattox et al. [116] have sidestepped this problem first by

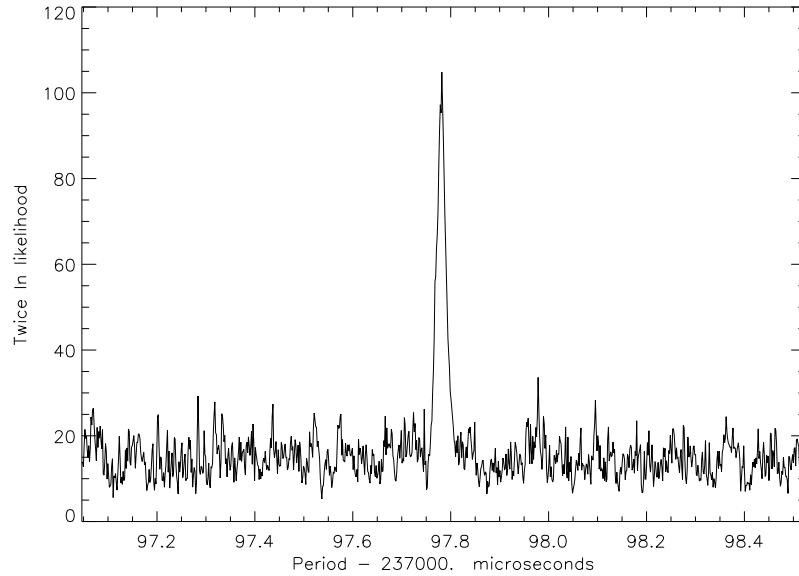


Figure 4.1: The likelihood of periodic modulation from Geminga, as a function of period, for a 30-bin light curve. Plotted on the  $y$ -axis is  $2 \ln \mathcal{L}$ , which is distributed as  $\chi^2_{29}$ , since the average intensity in the null model is a free parameter. The probability of the peak in the null model is less than  $10^{-25}$ . The maximum likelihood value of the period is 0.237097785 s, assuming a period derivative of  $1.09744 \times 10^{-14}$  s/s and a truncated Julian day epoch 8750.0.

turning to a Fourier algorithm—which is much faster, but cannot properly account for backgrounds and point-spread functions—and second by using a massively parallel computer. Further optimization may be possible to speed `timevar`, and certainly additional computing power will reduce the required search time. A similar program designed for *GLAST* will be slowed by the additional order of magnitude in the number of photons to process, but since the sensitive area will be larger, the elapsed time required to observe a sufficient number of photons will be shorter, allowing period space to be sampled less densely. In addition, faster computers will be available to do the calculations. The net effect will be that period searching with the *GLAST* equivalent to `timevar` will be quite feasible (Table 4.4).

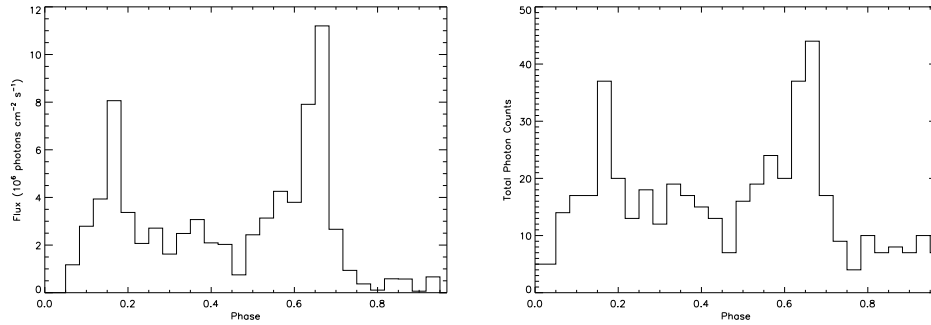


Figure 4.2: Light curves of the most likely period as found in Figure 4.1. The light curve on the left is the most likely flux in each bin, after accounting for the instrument point-spread function and sensitive area and the background. The light curve on the right is the raw photon count inside the 68% containment radius, as given by equation (1.1). This is the same as the light curve used by PULSAR.

#### 4.2.4 Bayesian Inference

A further advantage of the likelihood method employed by `timevar` is the ease by which results can be evaluated under a Bayesian framework. Strictly speaking, the plot shown in Figure 4.1 is meaningless in a maximum likelihood framework—only the maximum value, and not the entire likelihood function, is relevant. However, intuitively we expect the rest of the function to have some meaning. Local maxima should represent frequencies more likely to be present in the data. We would expect harmonics of the main pulse frequency to be present. As we saw in §2.6, the Bayesian formulation includes all this information into the posterior probability distribution. We simply multiply the likelihood function given in Figure 4.1 by the prior probability distribution. Then we may integrate the posterior distribution over interesting intervals, or simply present it as it is.

##### Appropriate Priors

The least-informative prior probability distribution for the pulsation period is scale-invariant. That is, it should not depend on the units used for measuring period, and it should be the same whether the search is done in period or frequency space. The appropriate solution is flat in the logarithm of the period. Therefore, we have

$P_{\text{prior}}(p) \propto 1/p$ . The upper and lower bounds of the period search define the cutoff, so that the prior can be normalized:

$$P_{\text{prior}}(p) = \left( \ln \frac{p_{\text{min}}}{p_{\text{max}}} \right) \frac{1}{p} \quad (4.26)$$

The least informative prior for the period derivative is uniform. The period derivative is a dimensionless number, and thus is the most natural unit in which to work. The last parameter of interest is the phase offset of the bin boundaries. This is also dimensionless, and thus the least informative prior is flat.

Gregory & Loredó [56] point out that marginalization over  $m$  yields the best light curve independent of the number of bins. This is exactly the spirit of the  $H$ -test. However, this is computationally impossible for a period search given the present state of the art. It is interesting to note here that the proper treatment of this problem is very difficult using frequentist statistics. Two models with different  $m$  have a different number of free parameters. The Bayesian framework takes care of this naturally; each free parameter (that is, each of the  $m$  fluxes) has its own prior; thus the complete prior for all the fluxes (assuming a flat prior between zero and the large cutoff) will be  $P_{\text{prior}}(\tilde{f}_m) = f_{\text{max}}^{-m}$ . This prior is a quantization of Ockham's Razor: models with more free parameters (that is, larger  $m$ ) are discouraged. The frequentist method compares each model to the null model, but cannot directly compare the two.

Figure 4.1 is actually one of three different likelihood functions measured for different phase offsets. It is the slice of the likelihood corresponding to the most likely offset. The perpendicular slice through the likelihood as a function of offset fixed at the best period is shown in Figure 4.3. The phase offset is a classic nuisance parameter; it arose by the arbitrary choice of  $t_0$  in equation (4.7). We therefore marginalize over the offset and arrive at the likelihood function shown in Figure 4.4.

To find the overall significance of a detection<sup>‡</sup> in the Bayesian framework, we multiply the likelihood function shown in Figure 4.4 by the period prior given in equation (4.26). The ratio of this probability with the probability of the null model

---

<sup>‡</sup>In our case, this will be the overall significance of a detection for all models with  $m$  bins. In principle, however, the parameter  $m$  could be marginalized over as well, yielding the true overall detection significance.

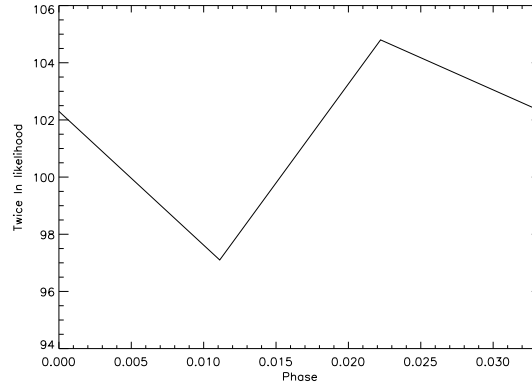


Figure 4.3: The likelihood of pulsation in Geminga as a function of the phase offset of the bin boundaries, for fixed period. The period chosen is that of the maximum likelihood for any offset, and corresponds to the peak seen in Figure 4.1. The width of the plot corresponds to one bin; therefore, the leftmost point and the rightmost point are the same.

( $m=1$ ) gives the odds ratio. In this case, the probability of periodic modulation is completely dominated by the peak, and the significance of the detection is  $1 - 7 \times 10^{-46}$ .

The Geminga pulsar is clearly detected by either method. The detections are so strong that even if a very large region of phase space had been searched, the detections would still be significant. Finding the significance that would have resulted from such a search may be calculated by assuming that the peak we found would be the maximum likelihood over the entire search, and that the number of trials would be the number of steps found in §4.2.3. A thorough search of viewing period 413.0 from  $50 \mu\text{s}$  to  $500 \mu\text{s}$ , over the appropriate period derivative ranges would require approximately  $7 \times 10^8$  trials. The significance of the detection in Figure 4.1 would still be  $1 - 10^{-20}$ . However, it is clear that weaker detections will not survive such a harsh attack. It is therefore also useful to develop some formalism for upper limits and detection thresholds.

#### 4.2.5 Upper Limits and Thresholds

The problem of upper limits was briefly touched upon in §2.7. There we noted that a desirable quality of an upper limit is that it be statistically well-behaved; that is, that

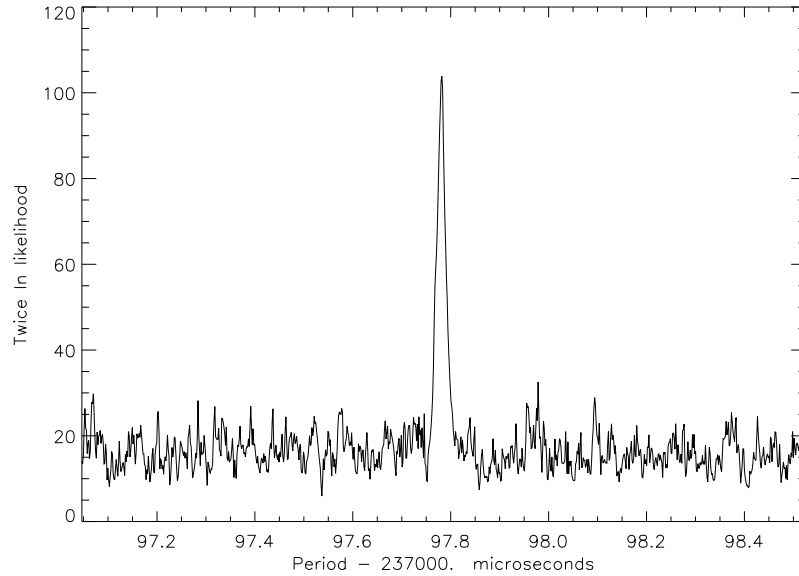


Figure 4.4: The likelihood of pulsation in Geminga. This likelihood function is similar to that shown in Figure 4.1, except that the likelihood has been marginalized over the phase offset.

a “ $1\sigma$  upper limit” be greater than the true value in 68% of the ensemble of possible data sets. The value of this upper limit depends on the details of the data.

In contrast, in some cases it may be more useful to calculate a threshold. We define a threshold to be the intensity (of a source, or of pulsation) that would be detected by our criteria in some fraction of the possible data that might be measured from that source. This may be quantified: an  $x\%$  detection threshold is that true parameter value for which  $x\%$  of possible data sets would result in detection. We make a statement about the outcome of a hypothesis test (is there pulsation?) instead of a statement about a point-estimate (is the pulsed fraction less than some value?).

There are three advantages to this. First of all, it more closely reflects the intuitive “upper limit” concept—that is, it is now reasonable to say, “The threshold for detection is  $f$ . Since we do not detect, then the actual value is probably less than  $f$ .” We will quantify this below. Second, we may calculate thresholds from the underlying distributions of the data; upper limits can only be calculated with the specific data



observed. This means that thresholds can be precalculated. This is a great advantage, especially for instruments which are still being designed or built. Finally, since we can use distributions, we can calculate thresholds (at least partially) analytically.

For the purposes of pulsation analysis, we will define the “pulsed fraction threshold” as the fraction of the flux (background plus source) that must pulse such that a fraction  $\xi$  of data sets observed with true sinusoidal variation with threshold amplitude will result in detection. We will assume that any data set with significance greater than  $\alpha$  will be a detection and the variation will be sinusoidal.

For simplicity, we define  $C \equiv 2 \ln \mathcal{L}$ . We will take  $\xi = 0.5$ , so that we may find the  $\alpha$ -point of the integral  $\chi^2$  distribution. That is, we seek  $C$  such that  $\int_0^{(C)} \chi^2(d, t) dx = \alpha$ , where  $d$  is the number of degrees of freedom, and  $t$  is the number of trials.<sup>§</sup> This follows from Wilks’ theorem (§2.5, [211]), which states that  $C$  is distributed under the null model as  $\chi^2$  with the number of degrees of freedom equal to the number of free parameters in the model. To find the mean value of  $C$ , we integrate over all data sets, weighted by their true probability:

$$\begin{aligned} \langle C \rangle &= \int_D \mathcal{L}_T(D) C(D) dD \\ &= \int_D \mathcal{L}_T(D) 2 [\ln \mathcal{L}_{BF}(D) - \ln \mathcal{L}_{BN}(D)] dD \end{aligned} \quad (4.27)$$

where  $\mathcal{L}_T(D)$  is the true likelihood of data  $D$ ,  $\mathcal{L}_{BF}(D)$  is the likelihood of the best model fit to data  $D$ , and  $\mathcal{L}_{BN}(D)$  is the likelihood of the best null model fit to data  $D$ .

To proceed, we turn once again to Wilks’ theorem. If the null model is true, then from equation (2.28) we have  $2(\ln \mathcal{L}_{BF} - \ln \mathcal{L}_{null}) \sim \chi_d^2$ . From the definition of the expectation value, we know that

$$\langle A(D) \rangle = \int_D P(D) A(D) dD \quad (4.28)$$

for any function  $A(D)$ . The expectation value of  $\chi_d^2$  is  $d$  [36], and the probability of

---

<sup>§</sup>Assuming that the mean of  $C$  is a good approximation to the median, so that roughly half of the realized values of  $C$  are greater than  $\langle C \rangle$ , and half are less.

the data is the likelihood of the data under the (unknown) true model  $\mathcal{L}_T(D)$ , so

$$\langle 2 [\ln \mathcal{L}_{BF}(D) - \ln \mathcal{L}_T(D)] \rangle = d \quad (4.29)$$

Therefore, we conclude that

$$\int_D \mathcal{L}_T(D) 2 [\ln \mathcal{L}_{BF}(D) - \ln \mathcal{L}_T(D)] dD = d \quad (4.30)$$

Substituting into equation (4.27), we have

$$\langle C \rangle = 2 \int_D \mathcal{L}_T(D) \ln \mathcal{L}_T(D) dD + d - 2 \int_D \mathcal{L}_T(D) \ln \mathcal{L}_{BN}(D) dD \quad (4.31)$$

We now make some further assumptions about the pulsation. As before, we will let  $f_m(\phi)$  to be the model flux as a function of  $\phi$  with  $m$  parameters. In particular, we will define the null model  $f_1(\phi) = f_1$ , with one parameter, the mean flux. We will further assume that the number of photons in each bin is large enough to approximate the Poisson distribution as a Gaussian (that is,  $n_i$  is large). Then in each bin  $i$  we may write

$$z_i = \frac{n_i - f_m(\phi_i)}{\sqrt{f_m(\phi)}} \quad (4.32)$$

where  $n_i$  is the number of photons in bin  $i$ , and  $f_m(\phi_i)$  is the model number of photons in that bin. Then  $\mathcal{L}_T(D) = \prod_i \frac{e^{-z_i^2/2}}{\sqrt{2\pi}}$ . For each bin, the first term of equation (4.31) becomes

$$\begin{aligned} \int_{D_i} \mathcal{L}_T(D) \ln \mathcal{L}_T(D) dD &= \int_{-\infty}^{\infty} \frac{1}{\sqrt{2\pi}} e^{-z_i^2/2} \left( -\frac{z_i^2}{2} - \ln \sqrt{2\pi} \right) dz_i \\ &= -\ln \sqrt{2\pi} - 1/2 \end{aligned} \quad (4.33)$$

This does not depend on the model  $f_m$  since for each bin, the best fit model should describe the data in approximately the same way. That is to say, the statistical deviation from the best fit model should not depend on the details of that model.

Using this result, equation (4.31) becomes

$$\langle C \rangle = -2m \ln \sqrt{2\pi} - m + d - \int_D \mathcal{L}_T(D) \ln \mathcal{L}_{BN}(D) dD \quad (4.34)$$

The last term contains the best fit null model. This must be related to the true null model in the same manner as equation (4.29).

$$\begin{aligned} \int_D \mathcal{L}_T(D) \ln \mathcal{L}_{BN}(D) dD &= \int_D \mathcal{L}_T(D) [\ln \mathcal{L}_{TN}(D) + 1/2] dD \\ &= 1/2 + \int_D \mathcal{L}_T(D) \ln \mathcal{L}_{TN}(D) dD \end{aligned} \quad (4.35)$$

Again assuming Gaussian fluctuations,  $\mathcal{L}_{TN}(D) = \prod_i \frac{1}{\sqrt{2\pi}} \exp \left[ - \left( \frac{n_i - f_1}{\sqrt{f_1}} \right)^2 \right]$ , yielding

$$\begin{aligned} \langle C \rangle &= -2m \ln \sqrt{\pi} - m + d - m + 2m \ln \sqrt{2\pi} \\ &\quad + \sum_{i=1}^m \int_{D_i} \frac{1}{\sqrt{2\pi}} \left( \frac{n_i - f_1}{\sqrt{f_1}} \right)^2 e^{-z_i^2/2} dD_i \end{aligned} \quad (4.36)$$

The number of degrees of freedom  $d$  is  $m - 1$ . To facilitate the integral, we write  $n_i$  in terms of  $z_i$ . The integral over the data  $D_i$  is properly normalized as an integral over  $z_i$ . We assume that  $n_i$  is large enough that expanding the bounds of integration from  $-\infty$  to  $\infty$  will introduce only a small error.

$$\langle C \rangle = -m - 1 + \sum_{i=1}^m \int_{-\infty}^{\infty} \frac{1}{\sqrt{2\pi}} e^{-z_i^2/2} \left( \frac{z_i \sqrt{f_m} + f_m - f_1}{\sqrt{f_1}} \right)^2 dz_i \quad (4.37)$$

The threshold is then given implicitly as a function of the parameters of  $f$  through  $z_i$ , as the value of the parameters such that  $\int_0^{(C)} \chi^2(d, t) = \alpha$ .

For example, one form of  $f$  might be a sinusoidal modulation plus a constant background:  $f(\phi) = B + A \sin 2\pi\phi_i$ . The average value over  $\phi$  is  $B$ , so  $f_1 = B$ . We may now ask the question: for a given background  $B$ , what is the threshold for detecting a modulation of strength  $A < B$ ? Comparisons of the threshold with the modulation expected on physical grounds can put null experiments into perspective (§4.4, [83]), as well as help identify potential candidate sources for pulsation detection.

### 4.2.6 Bin-free Maximum Likelihood

The application of maximum likelihood methods to pulsation searches binned photons to simplify and speed calculations. It is important to remember that this binning is not an essential element of likelihood methods. Recall from equation (4.19) that the likelihood function depends on a generic model function  $\tilde{f}$ . We may construct the maximum likelihood analogue of the  $Z_m^2$  by taking

$$\tilde{f}_m(\phi) = \alpha_0 + \sum_{k=1}^m (\alpha_k \sin 2\pi k\phi + \beta_k \cos 2\pi k\phi) \quad (4.38)$$

This function actually has  $2m + 1$  degrees of freedom. Given this, we can calculate equation (4.19), and maximize it with respect to the  $\alpha_k$  and  $\beta_k$ . In contrast with the binned case, we must now maximize the likelihood simultaneously for the model parameters. Instead of  $m$  one-dimensional maximizations, we must perform one  $(2m + 1)$ -dimensional maximization<sup>¶</sup> Since the  $A_i$  and the  $B_i$  are taken from numeric tables and the functions involved are rather complex, it is unlikely that it will be possible to maximize the functions analytically. Numerical methods for multidimensional maximizations are notoriously slow and prone to finding local minima [166]. Nevertheless, all the principles discussed above remain valid. The analogue to the  $H$ -test would be found by marginalizing over  $m$  with a suitable prior.

Sinusoids are familiar, and so are an obvious choice of basis. However, any set of basis functions may be used in a parameterization of  $\tilde{f}$ . Generalizing in a different way, we may imagine  $k$  bins with arbitrary boundaries, so that the bins may not be the same size. This would be represented by a stepwise function

$$f(\phi) = f_j, \quad \begin{cases} k_j \leq \phi < k_{j+1} \\ j \in [0, k) \end{cases} \quad (4.39)$$

where  $k_j$  indicates the beginning of bin  $j$ ,  $f_j$  is the flux in bin  $j$ , and there are  $k$  bins.

---

<sup>¶</sup>Reducing the number of Fourier components retained would not help this problem. Optimization with  $n$  Fourier components still requires an  $n$ -dimensional maximization, as opposed to  $n$  one-dimensional maximizations in the binned case.

Again, however, if the  $k_j$  are allowed to vary, the likelihood function is no longer separable, and all the model parameters must be simultaneously optimized.

### 4.3 Searching for Pulsars

Now that we have a statistical framework in which to search for pulsed flux in *EGRET* data, it is natural to use it to examine unidentified sources. A number of unidentified *EGRET* sources are positionally coincident (within large error regions) with known radio pulsars [43, 116, 136]. Other *EGRET* sources are concentrated in the Galactic plane. Since there are no other known strong Galactic  $\gamma$ -ray sources, and the Geminga pulsar is known to be radio-quiet, it is widely assumed [141, 163, 126, 116] that some or all of these sources are pulsars. It may be possible to detect pulsation from these sources without the use of ephemerides from other wavelengths.

One of the difficulties of such an analysis is the choice of the range of parameter space to search. The fastest millisecond pulsar has a period of 1.5 ms, and the slowest pulsars have periods of several seconds. The longest period pulsar observed in  $\gamma$ -rays is Geminga, with a period of about 237 ms. A reasonable search strategy would cover as much of this space as possible. The range of period derivative to search depends strongly on the period being searched. Equation (4.23) gives the minimum period derivative. Observed pulsars fall below an empirically determined cut-off in period derivative (Figure 4.5). All known  $\gamma$ -ray pulsars have period derivatives smaller than the cutoff. The known pulsar population occupies a relatively compact area on a plot of period versus period derivative, allowing the appropriate regions of parameter space to be searched for periodic signals.

Unfortunately, according to equation (4.23), the minimum period derivative to search decreases with decreasing period, and according to Figure 4.5, the maximum period derivative increases with decreasing period. Therefore, as we search shorter and shorter periods, the number of period derivative steps required increases rapidly. However, for periods larger than that where the sampling limit given by equation (4.23) crosses the period-derivative cut-off, we may ignore the period derivative. The time required to search a given region of parameter space thus depends weakly

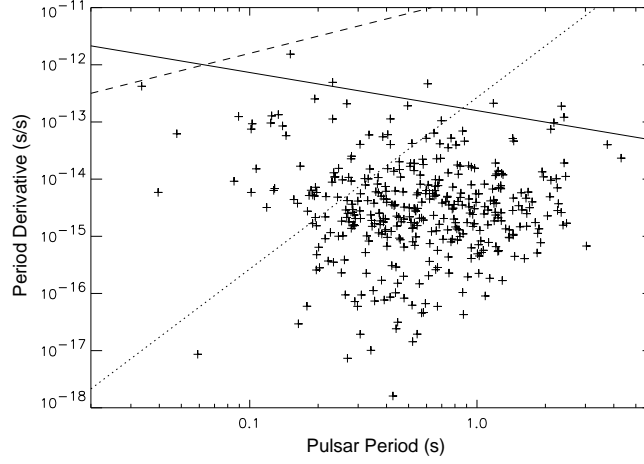


Figure 4.5: Periods vs. period derivatives for pulsars in the Princeton database [187]. The solid line is the high period-derivative cut-off line; almost all pulsars lie below and to the left of this line. The dotted line is the sampling limit; below it, period derivatives may be neglected for pulsar searches. This limit depends inversely on the square of the length of the observation; 10 days is assumed here. The dashed line corresponds to a characteristic age of 1000 years; no younger pulsars are expected.

on the maximum period to be searched, and strongly on the minimum period to be searched. A minimum period of 50 ms and a maximum period of 500 ms would contain all of the known  $\gamma$ -ray pulsars except the Crab. This range of period, and the appropriate range of period derivative for each period, is taken as the canonical search range.

### 4.3.1 Measurement of Known Pulsars

To verify that `timevar` is both statistically accurate and bug-free, several known pulsars were examined as if they had been the subject of a search. The results of those analyses are summarized in Table 4.2. Each known  $\gamma$ -ray pulsar was examined in one viewing period, chosen for good exposure to the source. A periodicity search was carried out for a small range around the known period, and the significance of the detection is given as if a single period had been tried. To find the total detection probability, the number of trials is found by calculating the number of parameter space

Pulsar	VP	True Period (ms)	<b>timevar</b> period	One-trial probability	Trials Needed <sup>a</sup>	Final <b>timevar</b> significance
Geminga	310.0	237.097785	237.097784	$4.8 \times 10^{-47}$	$5.5 \times 10^{12}$	$1 - 2.6 \times 10^{-34}$
Crab	001.0	33.38981606	33.38981541	$9.5 \times 10^{-146}$	$5.1 \times 10^{16b}$	$1 - 4.8 \times 10^{-129}$
Vela	301.0	89.29607605	89.2960604808	$6.7 \times 10^{-76}$	$8.7 \times 10^{12}$	$1 - 5.8 \times 10^{-63}$
B1706-44	232.0	102.4544637	102.24544626	$2.6 \times 10^{-14}$	$8.8 \times 10^{12}$	0.7712
B1055-52	014.0	197.1102023	197.110146607	$4.3 \times 10^{-4}$	$8.4 \times 10^{12}$	0
1951+32	203.0	39.530908008	39.5308978685	$2.0 \times 10^{-4}$	$1.7 \times 10^{17} \ b$	0

<sup>a</sup> Searching a period range from 50 ms to 500 ms

<sup>b</sup> Searching from 10 ms to 500 ms

Table 4.2: Detection of known  $\gamma$ -ray pulsars by **timevar**. The one-trial probability is the chance of observing the maximum likelihood value in a single trial. The number of trials is determined from the required sampling (§4.2.3) to search a period range from 50 ms to 500 ms, with the period derivative range appropriate for each period. For the Crab pulsar and PSR 1951+32 the search range is 10 ms to 500 ms. The total significance is the chance that no such likelihood would be observed in the given number of trials under the null model.

samplings required for the canonical search range for that observation. Unfortunately, we will find that this range is too ambitious to search with current technology.

The three brightest steady-state *EGRET* sources are Vela, Geminga, and the Crab. All three of these objects would have been easily discovered by **timevar** in a search of *EGRET* data with no prior information about their periods. Their significance is definitive; there would be no doubt about the validity of the detection. A light curve from Geminga is shown in Figure 4.2. A plot of likelihood versus period for the Crab is given in Figure 4.6, and the light curves associated with the most likely period are given in Figure 4.7. The likelihood peak in Figure 4.6 is very sharp. Note, however, that the probabilities given in Table 4.2 are taken only from the peak value of the likelihood. The Bayesian significance would be found by multiplying the likelihood function by the prior, and integrating over the width of the peak.<sup>||</sup> In this case, the choice of prior is largely irrelevant, since the likelihood is so sharply peaked. Figure 4.7 shows the maximum likelihood light curve as the flux measured in each bin, as well as the raw photon count within the energy-dependent 68% containment radius as given by equation (1.1) for the same pulsar period.

<sup>||</sup>In principle, one would integrate over the entire range. Since Figure 4.6 represents  $\ln \mathcal{L}$ , the contribution of all points not in the peak is negligible.

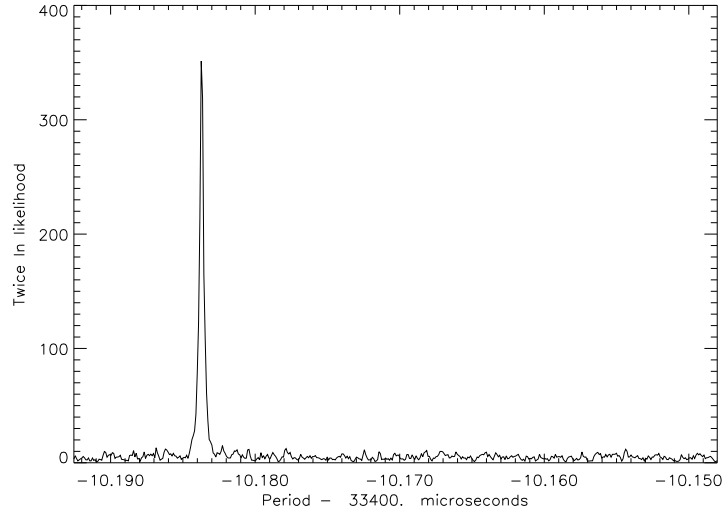


Figure 4.6: Twice the likelihood ( $C$ ) of flux modulation from Crab as a function of trial period for a 10 bin light curve.  $C$  is distributed as  $\chi^2_9$  in the null model. The maximum likelihood period is 33.38981541 ms.

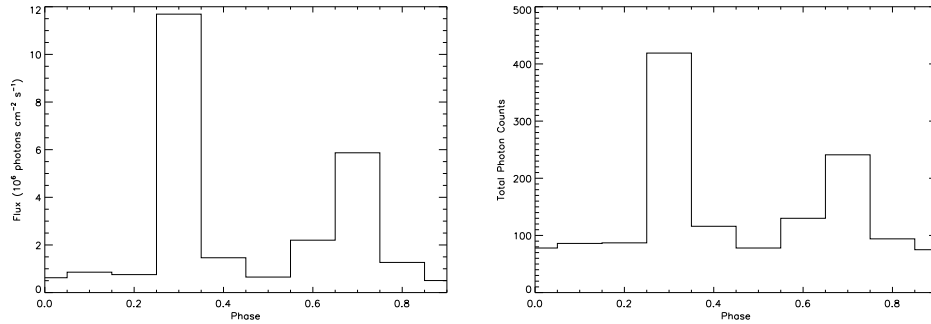


Figure 4.7: Light curves of Crab at the maximum likelihood period. The left light curve is the maximum likelihood flux in each bin. The right light curve is the raw photon count within the energy-dependent 68% containment radius.



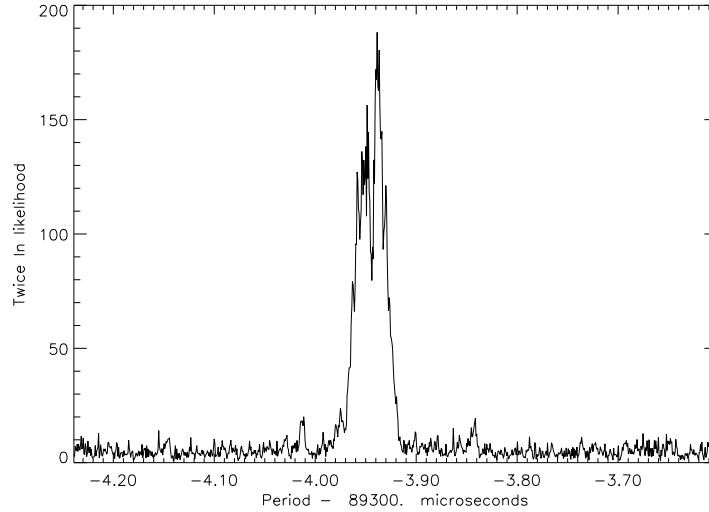


Figure 4.8: Twice the likelihood of flux modulation in Vela as a function of trial period for 10 bin light curves. The maximum likelihood period was 89.2960605 ms.

The likelihood peak for Vela in Figure 4.8 is not nearly as sharp as that for the Crab. The viewing period analyzed began on 22 August 1991 and ended on 5 September 1991, soon after a pulsar glitch on 20 July 1991 [48]. It is likely that Vela's period was not very constant during this observation, causing the broad likelihood peak observed.

In addition, PSR 1706-44 would have been detected with a significance of  $\sim 77\%$  (Figure 4.10 and 4.11). While this is not high enough to conclude that the emission is truly pulsed, it is based on the data from a single viewing period. Such detections should be rare enough that a small search in a different viewing period would be feasible to confirm the detection.

The remaining two known  $\gamma$ -ray pulsars, 1055-52 and 1951+32, were not detected significantly.

### 4.3.2 Searches for Geminga-like Pulsars

Of course, given the presence of Geminga, largely invisible to radio observations, as well as the large number of unidentified *EGRET* sources near the plane, it is natural to

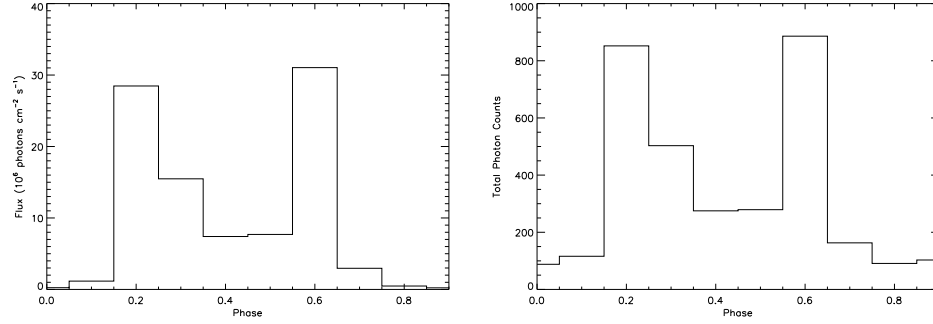


Figure 4.9: Light curves of Vela at the maximum likelihood period. The left light curve is the maximum likelihood flux in each bin. The right light curve is the raw photon count within the energy-dependent 68% containment radius.

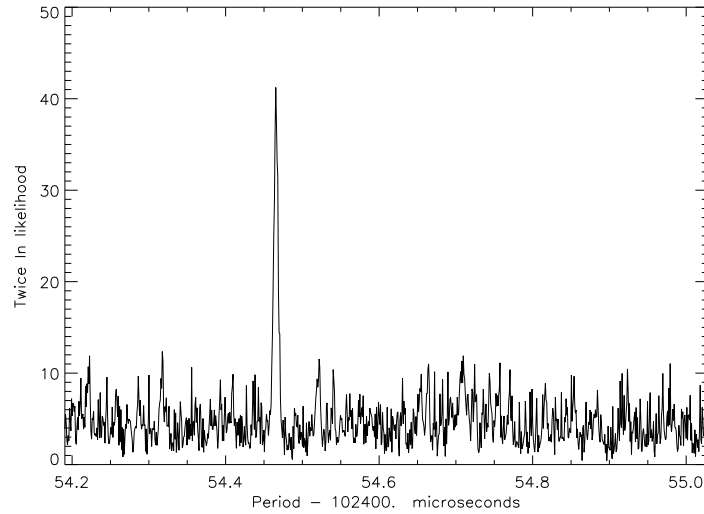


Figure 4.10: Twice the likelihood ( $C$ ) of flux modulation from PSR 1706-44 as a function of trial period for a 10 bin light curve. The maximum likelihood period was 102.24544626 ms

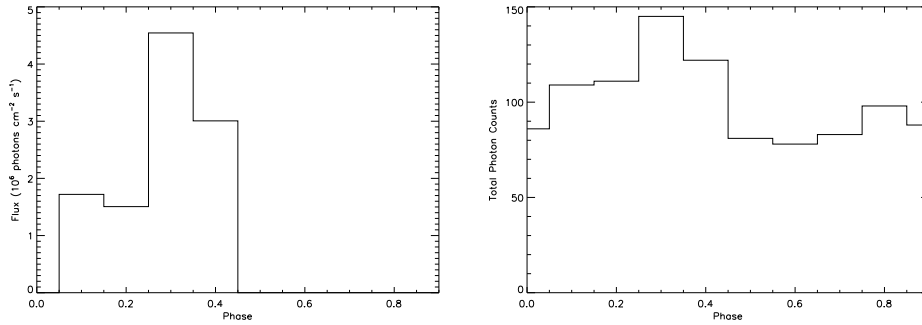


Figure 4.11: Light curves of PSR 1706-44 at the maximum likelihood period. The left light curve is the maximum likelihood flux in each bin. The right light curve is the raw photon count within the energy-dependent 68% containment radius.

suspect that some of these sources are Geminga-like pulsars (e.g., [141, 126, 163]). To begin the gargantuan task of examining the unidentified *EGRET* sources, we separate those which are likely to be good pulsar candidates. The criteria for determining good candidates are steady emission, a hard spectrum, and close proximity to the Galactic plane [43, 116].

One promising candidate is 2CG075+00, which is also known as GRO J2019+3719, and hereafter will be referred to as 2CG075. It lies very close ( $<0.5^\circ$ ) to the galactic plane, and has a very hard photon spectrum ( $\alpha = -1.40 \pm 0.14$ ) with a break occurring at about 1 GeV. Similar behavior is seen in Vela, Geminga, PSR 1706-44, and perhaps PSR 1055-52 [43]. There are no known radio pulsars inside *EGRET*'s 95% error contours of 2CG075.

The brightest unidentified  $\gamma$ -ray source is known as GRO J1745-28, and is positionally coincident with the Galactic center. While it is unlikely that the Galactic center is occupied by a pulsar, it is quite possible that a pulsar may be nearby. In addition, a significant spectral break has made it a popular choice as a pulsar candidate [116].

The *EGRET* error box on 2EGS J1418-6049 is smaller than the field of view of one of the X-ray cameras on the *ASCA* satellite. Analysis of the *ASCA* data in the *EGRET* error box has identified a potential X-ray counterpart [170]. The

Source	VP	$\langle B \rangle$	$I_{\text{TH}}$	$I_{\text{TH, trials}}$	$\langle I \rangle$	Detection Possible?
Geminga	310.0	443	66	131	562	Yes
Vela	8.0	1937.18	138	277	3699	Yes
Crab	310.0	1638	127	279	218	Possible
1706-44	232.0	2162	146	293	170	Unlikely
2CG075	203.0	2736	184	367	314	Possible
J1745-28	5.0	2134	162	377	158	Unlikely
J1418-61	314.0	1507	136	316	184	Unlikely

Table 4.3: Thresholds for pulsed sources. For each source, a viewing period is selected for observation.  $\langle B \rangle$  is the expected number of background photons within  $5^\circ 85'$  of the source.  $I_{\text{TH}}$  is the minimum number of source counts needed to detect pulsation in a single trial, and  $I_{\text{TH, trials}}$  is the number of counts needed to detect pulsation in a period search.  $\langle I \rangle$  is the expected number of source counts, based on the source flux and exposure in the viewing period.

*EGRET* data was searched for periodicity over a small region of parameter space in coordination with the X-ray effort.

Before too much computer time is spent examining candidate pulsars for fluctuation, it is worthwhile to consider the thresholds for pulsation detection. We can find the threshold for pulsed signal detection, assuming that all of the source flux is pulsed, and using the background in the direction of the source. The thresholds and actual flux levels for some sources of interest are given in Table 4.3. In accordance with what we have already seen, Vela, Geminga, and Crab significantly exceed their threshold flux. PSR 1706-44 is somewhat below threshold; in fact, in the absence of independent data to confirm our detection, we would not have considered PSR 1706-44 to be detected in a  $\gamma$ -ray period search.

Another useful application of threshold analysis is the estimation of the number of radio-quiet, Geminga-like pulsars that may be observed by *GLAST*. There have been many estimates of the Galactic population of such sources, based on the predictions of various pulsar models [215, 141, 126, 216]. Here we will estimate the instrumental threshold. As we have seen, the threshold depends on the amount of exposure to the source. Assuming we do not already know the pulse period, then a longer exposure means that we must search period space more densely (§4.2.3). This requires more trials, and thus, more computation time. An example is shown in Table 4.4. The

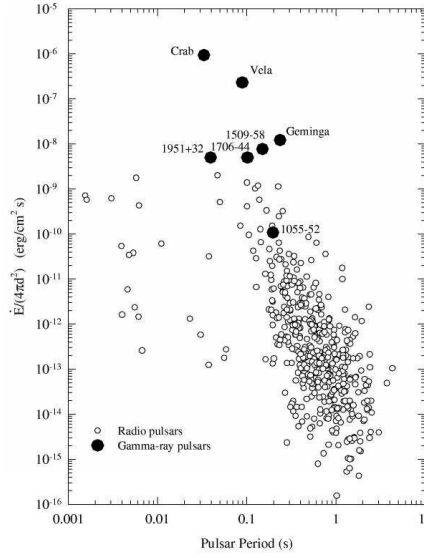


Figure 4.12:  $\dot{E}/D^2$  vs. pulsar period. Pulsars most likely to be identified have the highest apparent luminosities. The *EGRET* threshold is approximately  $5 \times 10^{-11}$  [191].

*EGRET* gas map is integrated over a hypothetical *GLAST* 68% containment radius of  $1.5^\circ$  to obtain a background flux ( $1.9 \times 10^{-7} \text{ cm}^{-2} \text{ s}^{-1}$ ). The detection threshold for a period search from 50 ms to 500 ms is given. The threshold continues to decline for longer exposures, while the number of trials required increases. The threshold includes the statistical effects of the number of trials, so the only limiting factor is computation time.

While the exact value of the detection threshold will depend on the details of the structured background at the point of interest, and the details of the instrument exposure, we may take  $1.5 \times 10^{-7}$  to be a reasonable threshold for the detection of pulsation in radio-quiet pulsars in a period search. Yadigaroglu & Romani [216] list 35 unidentified *EGRET* sources near the plane. Thirty of these have fluxes well above our threshold; three more are close to the threshold, and three are below it. While *GLAST* will detect many more sources than *EGRET*, it is unlikely to detect many new bright sources. It seems likely, then, that *GLAST* will be capable of definitively searching 25–30 radio-quiet pulsar candidates, either detecting pulsation or setting

Elapsed Time (Days)	Exposure ( $10^8 \text{ cm}^2 \text{ s}$ )	Threshold (known period)	Trials	Threshold (period search)
1.7	1.5	11.1	$1.7 \times 10^{10}$	20.7
3.4	3.0	7.9	$1.3 \times 10^{11}$	15.0
5.1	4.5	6.4	$4.3 \times 10^{11}$	12.4
6.8	6.0	5.6	$1.0 \times 10^{12}$	10.9

Table 4.4: *GLAST* thresholds in units of  $10^{-8} \text{ cm}^{-2} \text{ s}^{-1}$  for the detection of pulsed sources near the Galactic plane for known ephemerides, and for period searches. The number of trials is that required to search from 50 ms to 500 ms, with appropriate period derivatives.

stringent upper limits, effectively eliminating pulsars as an identification of these sources.

### 4.3.3 Results

Searching *EGRET* data for unknown-period pulsations is a very slow process. 2CG075 was analyzed with an array of approximately five Sparc 5 and Sparc 10 processors. Part of one viewing period (203.0) was searched from 137.8 ms to 500 ms in period and the requisite range of period derivative (§4.2.3). The analysis required approximately three months of continuous computation. The most significant pulse period and period derivative, while unlikely in a single trial ( $P = 5.6 \times 10^{-7}$ ), was not significant given the number of trials ( $4.6 \times 10^8$ ). To make sure that the detection was a statistical anomaly, a different viewing period (2.0) was searched in a very small window around the best ephemeris. There was no significant pulsing in the independent data.

J1418–604 was searched for periodic modulation in viewing period 314.0. No significant pulsation was seen. J1745–28 was searched in viewing period 5.0. While a very low significance detection was made, examination of the candidate pulse period in viewing period 223.0 revealed no significant modulation.

Candidate	VP	Period Range	Best Period	Significance
2CG075	203.0	137.8–500 ms	140.950161	$1.19 \times 10^{-34}$
J1418–604	314.0	226.5–300 ms	271.870713	0.55%
J1745–28	5.0	235.3–400 ms	277.760942	87.7%

Table 4.5: Results of period search with `timevar`. The infinitesimal significance of the 2CG075 detection stems from that fact that the single-trial significance of the most significant period would be expected to be observed about 260 times in the number of trials performed.

## 4.4 X-Ray Binaries

X-ray binary systems offer an excellent example of the advantages of coherent pulsation analysis with the methods used in `timevar`. Most orbital periods are between tens of minutes and several hours. This is comparable to, or longer than, the typical time scale of exposure changes in *EGRET*; thus any attempt to resolve orbital flux modulation must take explicit account of exposure changes. Meanwhile,  $\gamma$ -ray fluxes of X-ray binaries are low enough that direct observation of a single period of modulation is impossible. As with pulsar analyses, epoch folding offers a way to improve the signal-to-noise ratio and increase chances for the detection of orbital flux modulation. However, not only must the arrival times of photons be epoch folded, but also the changing exposure must be folded at the same period and phase to find accurate fluxes. [83]

X-ray binaries consist of a neutron star or black hole accreting material from a normal star. They constitute the brightest sources in the X-ray sky. X-ray binaries are divided into “low-mass” and “high-mass” systems, in reference to the normal companion. Low-mass X-ray binaries have an older star as a companion that generates little or no stellar wind. In order to emit significant X-ray power, the companion star must overflow its Roche lobe. The overflowing material then accretes onto the neutron star or black hole. If the system contains a neutron star with a large magnetic field, the material will flow along the field lines and accrete onto the polar cap. Otherwise, the material will form a thick accretion disk. X-ray emission can come from either the polar caps [137] or the inner edge of the accretion disk [179]. High-mass X-ray binaries have O or B stars as companions, which generate substantial stellar winds,

depositing  $10^{-6}$ – $10^{-10} M_{\odot}$  per year onto the compact object. This wind is sufficient to generate the observed X-ray luminosities [207].

Two major features are observed in X-rays over the binary orbit period. The first is a simple eclipse of the compact object, resulting in a rapid drop in the X-ray luminosity. The second is a dip in the X-ray luminosity, presumably caused by the obscuration of the compact object by the thick accretion disk [207]. Individual X-ray binaries may exhibit one or both of these features. The periods of the observed X-ray binary orbits range from 11.4 minutes to 398 hours.

#### 4.4.1 Thresholds and Searches

The low-mass X-ray binaries listed in Table 4.6 and the high-mass X-ray binaries listed in Table 4.7, taken from the lists in White, Nagase, & Parmar [207], were found to have a non-zero average flux with a significance of greater than  $1\sigma$ . However, without a detection of pulsation at the X-ray period it is not justified to claim an association of the  $\gamma$ -ray excesses with the X-ray binaries. Only one source, Cygnus X-3, was detected at the  $5\sigma$  level in *EGRET* data.

Thresholds for detection of periodicity were calculated using the method described in §4.2.5 for an extensive list of X-ray binary candidate sources. It was assumed that the source variation was sinusoidal. For any given values of source and background strengths, the detection threshold is a strong function of the duty cycle of the source. While it may be hoped that some X-ray binaries have duty cycles as short as 20%, it is more likely that  $\gamma$ -ray emission is fairly constant for most of the orbit, then drops sharply but briefly during eclipse. It was further assumed that the number of photons in any bin was large enough so that the Poisson distribution is well approximated by a Gaussian. This required a rather coarse division into five phase bins.

X-ray binaries which would be near the *EGRET* detection threshold if all their flux were modulated at the orbital period were examined with `timevar`. All photons from the source were epoch folded for a small range of periods around the known X-ray orbital period. They were assigned likelihood values with regard to the source and background strengths. The instrument exposure to the source was also epoch folded,



and the exposure for each bin was obtained. The likelihood of source fluctuation could then be calculated as in §4.2.3.

#### 4.4.2 Results

Most X-ray binaries [207] have source-to-background ratios so low that even if their orbital modulation fraction were 100%, the modulation would be undetectable. It would still be possible to detect modulation in such sources if the duty cycle were sufficiently short, but under the standard model of X-ray binary emission, this is unlikely. For candidate sources that have parameters near threshold, a maximum likelihood period search is done. The sinusoidal assumption is dropped in favor of a five independent bin light curve model. The choice of five bins was made to maximize flexibility in the model while retaining sufficient numbers of photons in each bin. Photons are barycenter corrected and epoch folded with trial periods in a small range ( $\pm 10\text{-}20\%$ ) of the known X-ray orbital periods. In contrast to the pulsar searches, the longer periods of X-ray binaries made it necessary to epoch fold the instrument exposure as well. While the exposure was fairly evenly distributed among bins in the shortest period binaries, it could be quite uneven for longer period X-ray binaries. Some sources were observed in more than one viewing period; Fourteen promising low-mass X-ray binaries (Table 4.8) and four promising high-mass X-ray binaries (Table 4.9) yielded no periodic signal detections significant at the 99% level.

Several sources were analyzed despite a low signal-to-noise ratio, in case they were to display variation with a very short duty cycle. Only Cyg X-3, which has been extensively studied in gamma rays [105, 135, 139], was bright enough to have a non-negligible chance of being detected, assuming a sinusoidal light curve. No evidence for variation was found in any of the sources.

Name	VP	Photons/bin	Max Modulation	Threshold
X0543–682 = Cal 83	329.0	8	14.4%	>80%
X0547–711 = Cal 87	224.0	13	33.2%	75%
	17.0	57	13.6%	45%
X1124–685 = N’Mus 91	230.0	22	14.6%	65%
X1323–619 = 4U1323-62	23.0	63	4.7%	40%
X1455–314 = Cen X-4	217.0	14	15.3%	75%
X1625–490	23.0	94	7.2%	35%
	529.5	76	9.0%	40%
XB1636–536	27.0	135	1.8%	30%
X1656+354 = Her X-1	9.2	37	6.7%	50%
XB1658–298	232.0	226	2.0%	25%
	5.0	438	1.2%	~10%
X1659–487 = GX339-04	336.5	98	2.6%	35%
	270.0	136	5.3%	30%
	226.0	127	2.1%	30%
	323.0	178	2.1%	27%
	210.0	31	4.4%	60%
	214.0	38	7.6%	52%
	5.0	246	2.2%	22%
	219.0	12	18.8%	75%
	302.3	68	2.2%	40%
	423.0	54	1.7%	45%
X1735–444	226.0	183	0.4%	27%
X1755–338	226.0	183	0.7%	27%
	229.0	18	4.9%	68%
X1820–303	323.0	260	0.4%	17%
X1822–371	508.0	47	2.5%	47%
	529.5	46	3.1%	47%
X1908+005 = Aql x-1	43.0	24	14.7%	60%
X1957+115 = 4U1957+11	331.5	42	3.1%	50%
X2023+338 = V404 Cyg	303.2	62	13.4%	42%
X2127+119 = AC211	19.0	46	1.6%	47%

Table 4.6: Low mass X-ray binaries. For each source, the viewing period of the observation is listed, along with the average number of photons in each phase bin, the modulation fraction that would be measured if all the source flux were modulated, and the threshold modulation fraction that would yield a 99% significance detection in half of all possible data sets.

Name	VP	Photons/bin	Max Modulation	Threshold
X0532–664 = LMC X-4	6.0	44	16.1%	50%
	17.0	52	13.6%	45%
	224.0	12	37.3%	80%
X0538–641 = LMC X-3	6.0	42	7.9%	50%
X0540–697 = LMC X-1	17.0	55	24.0%	43%
	6.0	46	10.9%	47%
X1119–603 = Cen X-3	14.0	164	3.7%	27%
	402.5	31	18.6%	57%
	402.0	27	19.3%	57%
	208.0	19	21.5%	70%
	215.0	8	22.3%	>80%
X1538–522 = QV Nor	516.1	20	1.2%	70%
X1700–377 = HD153919	508.0	36	5.4%	54%
X1956+350 = Cyg X-1	318.1	60	7.3%	44%
	601.1	36	15.8%	54%
X2030+407 = Cyg X-3	203.0	476	13.3%	15%
	2.0	296	14.4%	21%
	7.1	133	10.8%	30%
	212.0	243	14.8%	23%
	303.2	77	16.1%	38%
	328.0	67	27.9%	42%
	331.0	30	26.4%	57%
	331.5	48	15.9%	47%
	333.0	64	3.6%	42%
	601.1	32	26.1%	57%
	34.0	54	5.1%	47%
	p12 <sup>a</sup>	1039	10.6%	12%

---

<sup>a</sup>Combined data from Phases 1 and 2.

Table 4.7: High mass X-ray binaries. For each source, the viewing period of the observation is listed, along with the average number of photons in each phase bin, the modulation fraction that would be measured if all the source flux were modulated, and the threshold modulation fraction that would yield a 99% significance detection in half of all possible data sets.

Source Name	X-ray Orbital Period (hr)	Significance of $\gamma$ -ray modulation
X0543-682	25.0	0.23%
X0547-711	10.6	56.0%
X1124-685	10.4	0.7%
4U1323-62	2.93	0.25%
Cen X-4	15.1	54.4%
X1624-490	21.0	54.2%
XB1636-536	3.8	8.8%
Her X-1	40.8	5.0%
XB1658-298	7.1	49.7%
GX339-04	14.8	60.4%
X1755-338	4.46	1.0%
4U1957+11	9.3	0.25%
X2023+338	5.7	94.0%
X2127+119	17.1	0.65%

Table 4.8: Low-mass X-ray binaries that were searched with `timevar`, their orbital periods, and the significance of  $\gamma$ -ray flux modulation as found by `timevar`.

Source Name	X-ray Orbital Period (hr)	Significance of $\gamma$ -ray modulation
LMC X-4	33.6	77.5%
LMC X-3	40.8	10.1%
LMC X-1	101.28	54.5%
Cyg X-3	4.8	17.8%

Table 4.9: High-mass X-ray binaries that were searched with `timevar`, their orbital periods, and the significance of  $\gamma$ -ray flux modulation as found by `timevar`.

# Chapter 5

## Conclusions

Most astrophysicists consider the study of statistics and statistical methods only slightly more interesting than taxonomy and speeches by university presidents. While this feeling is by no means unique to astrophysics, it is particularly unfortunate in a field where statistics play such a pivotal role in our understanding of the scientific data.

Astrophysics may be differentiated from other specialties by the unique nature of experimentation. In fact, we have a separate word to describe experimental astrophysics: observation. The choice of language highlights the fact that in astrophysics more than any other realm of physical study we are most often passive collectors of data, rather than active experimenters manipulating controlled environments. This is not to say that astrophysicists are lazy; indeed, enormous amounts of work have gone into the design, construction, and analysis of all kinds of observatories. Concentrating on high-energy astrophysics, we have seen the great contribution of *SAS 2*, *COS B*, and *EGRET*. We anticipate further advances from *GLAST*.

Unfortunately, the institutional disinterest in statistics has put some of this tremendous effort to waste.  $\gamma$ -Ray instruments are carefully designed to have great sensitivity to individual photons. The scarce quanta are jealously collected, for they each contain a great deal of information. Indeed, the entire theoretical field of  $\gamma$ -ray burst mechanisms has been forced to account for a single *EGRET* photon [76]. It seems puzzling, then, that after all the quality efforts made to improve the capabilities of

each of the previous  $\gamma$ -ray telescopes, the statistical analysis methods were developed as an afterthought. The result [117] was that the capabilities of the *EGRET* instrument were not fulfilled until very late in the mission [65]. Since *LIKE* does not fully use all the information in the data, various attempts have been made to cajole the standard analysis programs into being more efficient with the data.

An example will help clarify the point. *LIKE* applies the average photon point-spread function to all photons in the data set. Of course, the width of the *EGRET* point-spread function depends strongly on the photon energy. This causes *LIKE* to understate the information in the location of high-energy photons, and overstate the information in the location of low-energy photons. The net result is that the error estimates of point-source locations is significantly larger than it needs to be. The data set may be restricted to a smaller energy range [104], thereby making the average point-spread function a better estimate of the actual point-spread function for more of the photons in the data set. However, this improvement comes at the expense of cutting drastically the number of photons available. The efforts of the instrument designers to capture more photons have been wasted.

There are many factors that go into the design of statistical tools to analyze  $\gamma$ -ray data. Simplicity of design and computational speed are often taken as the driving considerations. A better approach, however, is to begin with a correct statistical implementation that uses all of the information in the data. This theoretical implementation can then be simplified to achieve speed and simplicity requirements. The advantage of the “top-down” approach is that the approximations and simplifications can be made rationally, fully weighing the losses in accuracy against the gains made in other areas. This is the spirit in which *timevar* has been designed for periodic signal analysis. Tompkins [199] has developed a successor to *LIKE* along these lines. The result is a statistical method which is no more complicated than *LIKE* that computes in reasonable speed and offers much better position estimates and much smaller error regions. Such an approach avoids the pitfalls of an empirical design of statistical methods, in which *ad hoc* adaptations may have unforeseen consequences (§4.2.1).

We stand now on the brink of the next generation of  $\gamma$ -ray astronomy. The efforts of scores of scientists at dozens of institutions throughout the world are producing

the design of a  $\gamma$ -ray telescope that will revolutionize high-energy astrophysics. While experts make extensive computer simulations of the instrument to optimize the design, and engineers carefully design the electronic, mechanical, and thermal structures of *GLAST*, relatively little effort is going into the design of the statistical apparatus to analyze the wealth of data that will someday pour forth. Unfortunately, this is not a project which can profitably be left until the design stage is over. Realistic interpretations of computer simulated data rely on high-quality data analysis software. The design of that software depends (§2.2) on the instrument design.

The final goal of any telescope is to make observations which lead to increased understanding of astrophysical objects. In the case of  $\gamma$ -ray telescopes, this is achieved by the design of an instrument that simultaneously optimizes various scientific goals (sensitive area, point-spread function, energy range and sensitivity, photon timing) with various spacecraft limits (power consumption, heat production, telemetry limits). It does so by optimizing different instrument subsystems: the  $e^-e^+$  tracking system, the calorimeter, and the triggering system, among others. A well designed instrument would consider the data analysis methods and software to be a separate subsystem, just as important to the success of the instrument as the other systems. In fact, instrument design choices must take into consideration the impact on data analysis. Various instrument design choices, such as pointing modes, zenith cuts, and instrument modes can have significant impact on the data analysis process, and in some cases, can limit the precision of the results.

The purpose of this work is to elucidate the statistical methods best suited to the analysis of periodic flux modulation in  $\gamma$ -ray data. These methods should be appropriately modified for use with *GLAST*. In addition, the calculation of thresholds for various *GLAST* configurations and modes can be used to concentrate analysis efforts on objects that seem most likely to be detected. It is likely that some simplification of the methods will be necessary to enable the analysis to be performed in a useful and timely way; but these simplifications can now be made from a basis of a well-developed statistical method, rather than in an *ad hoc* manner which may unnecessarily degrade the quality of *GLAST* results.

Statistical techniques are the double-edged sword of high-energy astrophysics.

Without them, the field would not exist. The existence of high-energy emission from some  $\gamma$ -ray bursts would be unknown. Our understanding of pulsar energy-generation mechanisms would be strikingly curtailed. Nevertheless, their misuse has caused large segments of the astrophysical community to doubt their validity. So called “ $4\sigma$ ” results are believed with a confidence of about 90%—far from the nominal 99.9937% which they claim. This lack of confidence comes from the misuse and misunderstanding of statistics and statistical methods, which is in turn a direct result of the general disinterest in statistical methods in astrophysics. I hope that this work has inspired interest in developing useful and correct statistical methods that dispel the indifference and improve the results of future high-energy astrophysical experiments.



## Part II

The October 1997

*GLAST*-prototype Beam Test

## Chapter 6

# *GLAST*: The Next Generation

The success of the *EGRET*  $\gamma$ -ray telescope has answered many questions, but it has also given rise to new ones. The bounty of unidentified *EGRET* sources undoubtedly holds the key to understanding a wide variety of astrophysical systems. Several of these sources at low Galactic latitude are likely to be Geminga-like pulsars [215, 126, 163]. High-latitude sources may be unobserved AGN, or may be a new class of sources not yet associated with  $\gamma$ -ray emission [156]. Furthermore, *EGRET* has positively identified many  $\gamma$ -ray sources that deserve further study. While a number of  $\gamma$ -ray pulsars have been extensively studied [46, 152], additional high-quality  $\gamma$ -ray data would discriminate between competing models of energy-generation mechanisms [61, 26, 171]. Multiwavelength campaigns to simultaneously observe AGN from radio wavelengths to  $\gamma$ -rays have become an important tool in understanding energy generation in these distant yet powerful galaxies [64, 138]. The recent discoveries of optical counterparts to  $\gamma$ -ray bursts [31] underscores the need for a large field-of-view, high-energy  $\gamma$ -ray detector. In order to achieve these goals we require a  $\gamma$ -ray telescope with a large effective area, a narrow point-spread function, and good energy and timing resolution.

A proposed future telescope to that end is *GLAST*, the Gamma-ray Large Area Space Telescope (Figure 6.1). *GLAST* will be based on solid-state silicon strip detector technology to provide high-quality  $e^-e^+$  tracks from pair conversion events which can be reconstructed to give good directional information about the incident  $\gamma$ -ray. A

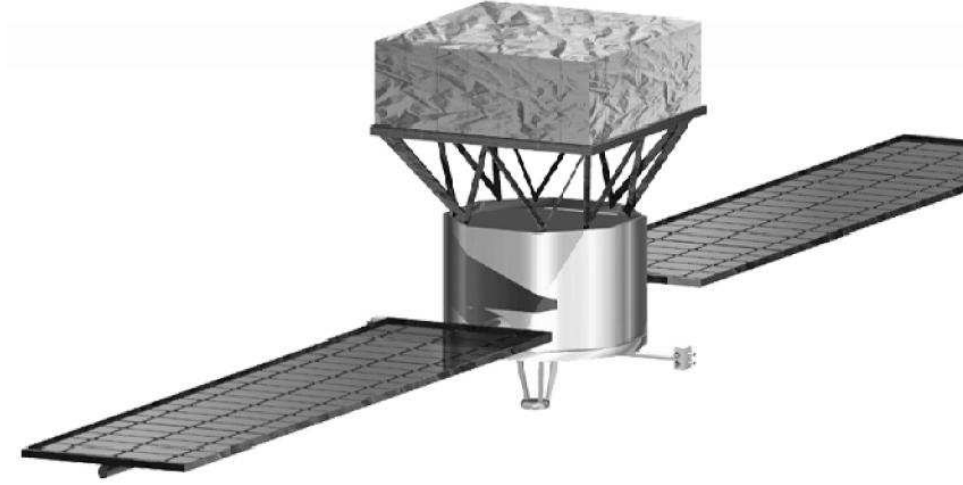


Figure 6.1: Artist's conception of the *GLAST* satellite. The square detector array is held away from the spacecraft bus to minimize background. Courtesy of the *GLAST* Facilities Science Team.

calorimeter will provide energy information and possibly some directional information as well [134, 2, 14, 15].

## 6.1 Potential Improvements

Given the great success of *EGRET*, is there any call to spend significant time, energy, and resources to build the next generation  $\gamma$ -ray telescope? Potential budget ramifications are beyond the scope of this work; nevertheless, it is useful to look into the science gains that might be hoped for. We will focus on the  $\gamma$ -ray bursts, pulsars, and X-ray binaries, the subject of Chapter 3 and Chapter 4.

**$\gamma$ -Ray Bursts.** As we discussed in Chapter 3, only a handful of  $\gamma$ -ray bursts were detected by *EGRET*. It seems likely that some bursts have a very soft spectrum, or perhaps a spectral break, so that the  $\gamma$ -ray luminosity was far below the *EGRET* threshold. However, there are also a number of instrumental limitations on *EGRET*  $\gamma$ -ray burst observations. The first of these is the instrument field-of-view. *BATSE* observes approximately one burst per day in the entire sky. The *EGRET* field-of-view

is somewhat less than 1.5 sr; an instrument with a field-of-view closer to  $2\pi$  sr would observe a bursts approximately every day as well. At any given time, *EGRET* has a sensitive area of 800–1000 cm<sup>2</sup>. Increases in the sensitive area translate directly into increases in the number of photons observed from each burst, yielding better information on burst flux, time profile, and position. Perhaps most importantly, *EGRET* estimates of  $\gamma$ -ray burst flux were strongly constrained by dead-time considerations. With the *EGRET* instrument inactive for about 100 ms after every trigger, many  $\gamma$ -ray burst photons are probably missed in the initial spike of  $\gamma$ -ray flux. There is no way to estimate the missed flux without recourse to another instrument, since the burst time scale is of the same order as the dead time. Thus, the ideal high-energy  $\gamma$ -ray burst instrument would have a wide field-of-view, large sensitive area, good angular resolution at low energies, and very short dead times.

**Pulsars and X-ray binaries.** The two primary difficulties in searching for flux modulation from pulsars are the low signal-to-noise ratios, and the large region of parameter space that must be searched. The instrumental parameters which alleviate these issues are increased sensitive area, and improved point-spread function. Increasing the sensitive area means that more photons are detected in less elapsed time. The sampling density required (§4.2.3) depends on the total observation time, so the increased sensitive area means that, for the same signal-to-noise ratio, period space may be searched less densely. The increased sensitive area combines with an improved point-spread function to improve the signal-to-noise ratio. This lowers the thresholds for both pulsar and X-ray binary pulsed flux detection. It is likely that X-ray binaries other than Cygnus X-3 will be detected with *GLAST* in steady state, and many of the X-ray binaries listed in Table 4.6 and Table 4.7 will be above the threshold for the detection of flux modulation. In addition, the sensitivity of *GLAST* to photons down to  $\sim 20$  MeV will greatly enhance the sensitivity to soft sources like X-ray binaries.

The proposed *GLAST* instrument will excel at all three of the desired capabilities. As described in the next section, the sensitive area will be nearly an order of magnitude greater than that of *EGRET* at high energies. The point-spread function

$\gamma$ -ray Telescope Characteristic	<i>GLAST</i> Baseline Performance
Energy Range	20 MeV to 300 GeV
Energy Resolution	$< 25\%$ , 10 MeV to 300 GeV $< 10\%$ , 100 MeV to 10 GeV
Effective Area	8000 cm <sup>2</sup> above 1 GeV 4000 cm <sup>2</sup> at 50 MeV
Point-Spread Width	$3.1^\circ \times 100 \text{ MeV}/E$ (68% containment)
Off-axis <sup>a</sup> width	$1.4 \times$ on-axis width
Field of View (FWHM)	2.6 sr
Point Source Sensitivity	$3.5 \times 10^{-9}$ photons cm <sup>-2</sup> s <sup>-1</sup> (1 year, $E > 100$ MeV, $5\sigma$ significance)
Point Source Location	30 arcsec–5 arcmin
Mission Life	5 years (2 year minimum)
Mass	3000 kg
Power	600 W
Telemetry (average)	100 kbps
Orbit	600 km low-inclination

<sup>a</sup>where the sensitive area drops to half of its on-axis value

Table 6.1: Characteristics of the baseline *GLAST* instrument. Values found by *glastsim* simulation of the baseline instrument [15].

will be almost a factor of two smaller in radius, and the dead time will be about 100 times less than the *EGRET* dead time. These factors will combine to make *GLAST* an excellent instrument for observing  $\gamma$ -ray bursts, pulsars, and X-ray binaries.

## 6.2 The Baseline *GLAST* Instrument

*EGRET* has revealed the  $\gamma$ -ray sky to be a vast resource of astrophysical information. As described fully in §1.2, the *EGRET* instrument is composed of three sections: a calorimeter, an  $e^-e^+$  tracker, and an anti-coincidence system. *GLAST* will follow the same paradigm, although the technologies used for each component have advanced significantly in the two decades since *EGRET* was designed.

The instrumental requirements for *GLAST* are driven by the scientific questions we wish to answer. Locating point sources and separating nearby sources requires

compact point-spread functions. Observing  $\gamma$ -ray bursts requires large photon collection area and very short dead times at the lowest energies, where burst photons are more plentiful. Pulsar timing also requires large photon collection area, but the hard spectra of pulsars necessitates good sensitivity to higher energy photons. Spectral measurements of all sources require good energy resolution. Monitoring for transient events like AGN flares and  $\gamma$ -ray bursts requires a large field of view (FOV). In addition, all of these goals must be achieved while maintaining excellent ( $> 1 : 10^5$ ) background rejection to eliminate cosmic ray contamination, while staying within the structural and power constraints dictated by the spacecraft design.

The *GLAST* instrument is still in the planning stages, and as such many options for achieving these goals are being discussed. Most of these discussions take place as variations on the baseline design as developed by an international collaboration of scientists from many institutions around the world (Table 6.2). This design was proposed for funding to the Department of Energy and NASA in 1998, as well as to other international agencies [15]. The baseline design currently calls for a  $5 \times 5$  array of modular towers. Each tower would consist of 17 trays arranged to hold 16 layers of silicon strip detectors. Each layer would measure the location of passing charged particles in  $x$ - and  $y$ -projections. plane. In addition, each tower would contain 80 CsI(Tl) blocks of approximately  $2.3 \text{ cm} \times 3 \text{ cm} \times 31 \text{ cm}$  arranged horizontally in eight layers of ten blocks in alternating  $x$ - $y$  orientations to measure the total energy of the  $\gamma$ -ray. PIN diodes attached to each end of each block allow differencing of the light detection in order to determine a lateral displacement. The baseline anticoincidence detector (ACD) covers the entire instrument to identify cosmic rays. It consists of plastic scintillator tiles 1 cm thick and approximately the size of a single tower, arranged in two offset layers to cover all cracks.

The baseline tracker design consists of planes of silicon strip detectors (SSDs). Although some alternative designs (gas microstrip detectors [74] and scintillating fiber detectors) are being considered, the prototype instrument tested in the October 1997 beam test was based on silicon strip technology. Therefore, we will concentrate on the silicon strip baseline.

Optimization studies have been performed [15] using Monte Carlo simulations for

Aerostudi, S.r.l.	Shibaura Institute of Technology
Boston University	Sonoma State University
Commissariat a L'Energie Atomique (CEA)	Stanford Linear Accelerator Center
École Polytechnique	Stanford University
Hytex, Inc.	Texas A&M University–Kingsville
ICTP and INFN, Trieste	U.S. Naval Research Laboratory
Kanagawa University	University of California, Santa Cruz
Laboratory for High Energy Astrophysics	University of Chicago
Lockheed Martin	University of Rome
Max Planck Institut für Extraterrestrische Physik	University of Tokyo
NASA Ames Research Center	University of Utah
NASA Goddard Space Flight Center	University of Washington

Table 6.2: Institutions in the *GLAST* Collaboration

a variety of tracker configurations. Some of the considerations that go into such an optimization are discussed in §7.2.1. The best design found so far consists of 17 trays of detectors, with 3.5% radiation length ( $X_0$ ) Pb radiators to convert  $\gamma$ -rays to electron–positron pairs (§8.1), and 400  $\mu\text{m}$  thick SSDs with a 195  $\mu\text{m}$  pitch, or distance between strips. Each tray has detectors on the top and bottom of a thick wafer of low-density material. Thus the SSDs on the bottom of one tray are close to those on the top of the next. Such a pair of SSD layers are treated as one logical “plane” for the purposes of  $e^-e^+$  measurements. Since there are no SSDs on either the top of the first tray or the bottom of the last tray, we have 16 detector planes in the tracker. Each layer will consist of a  $5 \times 5$  array of SSDs, each one of which is 6.4 cm  $\times$  6.4 cm. The SSDs will be connected into chains along their strip axis, resulting in an effective size of 6.4 cm  $\times$  32 cm. The signal-to-noise ratio in each strip is approximately 23:1 for a minimum ionizing particle.

## Chapter 7

# Testing the *GLAST* Science Prototype

In order to demonstrate the feasibility of the *GLAST* project, as well as to confirm observational parameters measured in simulations of the instrument, a science prototype was constructed at the University of California, Santa Cruz, the Naval Research Laboratory, and Goddard Space Flight Center. It was tested in the parasitic electron beam at the Stanford Linear Accelerator Center (SLAC) in October of 1997 [169]. Modeling instrument response, both analytically and through Monte Carlo simulations, and verifying those results experimentally has become a viable way to optimize instrument design while minimizing costs [88].  $\gamma$ -Ray reconstruction software was developed and tested with Monte Carlo simulations (Chapter 8), and then was used to analyze the experimental results. Comparison of the actual beam test results with simulation confirmed that the simulations represent an accurate model of the beam test instrument, and by extension, of the baseline *GLAST* design [86]. These results will be discussed in Chapter 9.

### 7.1 The SLAC $e^-$ Beam

The October 1997 beam test was conducted in End Station A at the Stanford Linear Accelerator Center [169]. End Station A is located at the end of the main linear



accelerator beam (Figure 7.1). This choice of testing location was a combination of design requirements and practical considerations. For the purposes of our test, we desired a beam of incident electrons arriving approximately one at a time, which we could either directly measure with our apparatus, or first convert to high-energy  $\gamma$ -rays. End Station A accommodates such a beam with the linac in *parasitic beam* operation [23].

Parasitic mode means that the beam consists of particles which have been scraped away from the main beam. The main experiment at SLAC during October 1997 was SLD, a search for  $Z_0$  vector bosons. SLD required rapid, well-focused bunches of approximately  $10^{11}$  electrons or positrons for collision. The main linac produces bunches of electrons or positrons at a rate of 120 Hz, and accelerates them to 50 GeV. The SLD beam profile was defined with a small aperture to achieve a compact, nearly monoenergetic beam. Electrons (and positrons) in the wings of the profile would stop in the massive shields around the aperture. Bremsstrahlung  $\gamma$ -rays would continue forward, while the rest of the main electron beam was magnetically steered into the SLC arcs. These  $\gamma$ -rays could then be converted back to electrons by passing through a high-Z foil. The number of electrons per pulse could be limited by adjusting the size of the momentum acceptance in the transport line [38].

This resulting beam of “parasitic” electrons then consisted of a mix of electrons and positrons with a broad range of energies. Steering magnets selected electrons of the desired energy and delivered them to End Station A. The electron energy was tunable from approximately 5 GeV to approximately 40 GeV. The number of electrons per bunch was tunable over a wide range from less than one to many tens of electrons.

Once the electron beam had been delivered to End Station A, we modified it appropriately for our own uses. For several runs, we took the beam directly as it came; usually a 25 GeV electron beam. This was useful to calibrate the calorimeter, to do backslash studies with the anti-coincidence detector (ACD) and to look at straight tracks in the silicon tracker. However, most of the data was taken with a thin Cu radiator (usually 3.5%  $X_0$ ) inserted in the electron beam. Between the radiator and the instrument was a large magnet known as B $\emptyset$ . By adjusting the

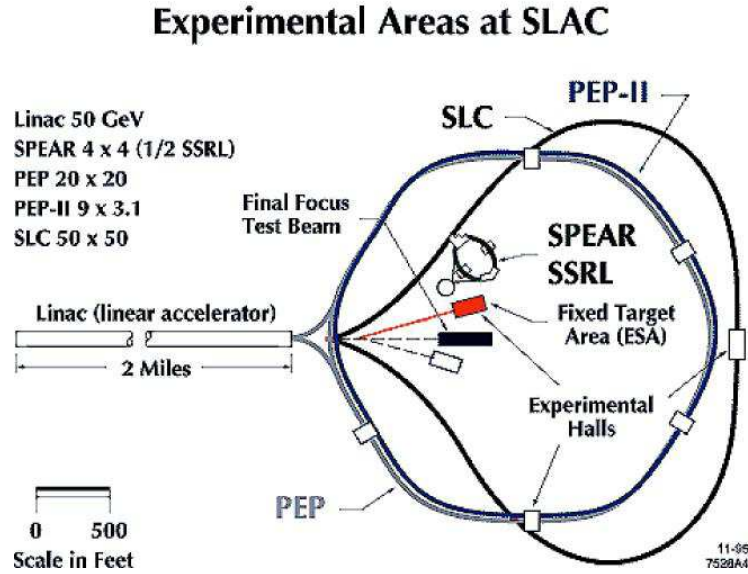


Figure 7.1: Location of End Station A at SLAC. The October beam test took place in End Station A (ESA), also known as the Fixed Target Area. The linac was simultaneously providing beam for SLC.

magnetic field in  $B\theta$ , the electron beam could be steered aside and deposited in a hodoscopic calorimeter. If the electron in the beam shed a bremsstrahlung photon in the Cu foil, then its energy was reduced, and its deflection in  $B\theta$  was greater. The hodoscopic calorimeter had 88 fingers arrayed horizontally to measure this deflection. This allowed us to tag the energy of  $\gamma$ -rays incident on our instrument to an accuracy of about 250 MeV.

Events with multiple  $\gamma$ -rays in the tracker were quite undesirable. It was likely that only one of the  $\gamma$ -rays would be detected in the tracker, while both would deposit energy in the calorimeter. The apparent energy of such an event could be strikingly different than its true energy, and recognizing such events in the data would be very difficult. Therefore, it was desirable to keep the number of  $e^-$  per pulse small; for most of the runs, the momentum slits were set to allow approximately one  $e^-$  per pulse on average. Of course, the number of  $e^-$  in a pulse is a Poisson process, so there was exactly one electron in each pulse approximately one-third of the time. When

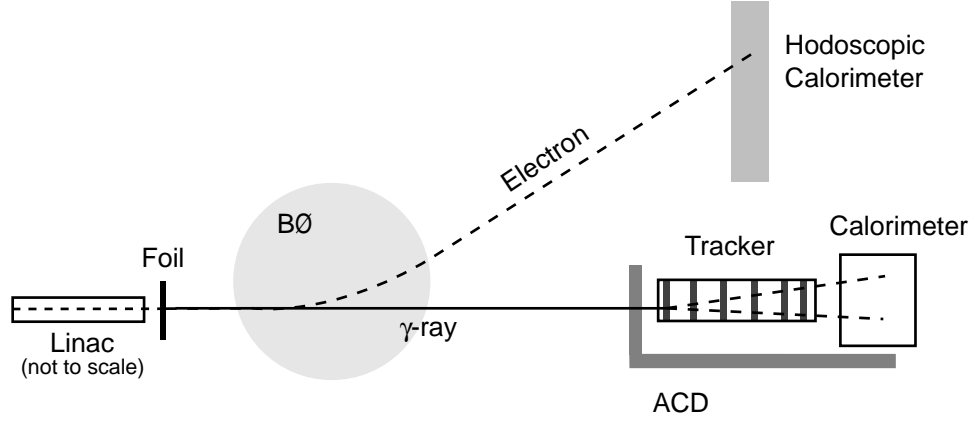


Figure 7.2: Diagram of the beam test experimental scheme. The 25 GeV electron beam entered from the left, incident on a high-Z foil. Some electrons emitted a bremsstrahlung photon, which continued through the ACD, and into the silicon tracker. Some  $\gamma$ -rays converted to  $e^-e^+$  pairs in the tracker. The  $\gamma$ -ray energy could be measured with the calorimeter. A magnet,  $B_0$ , deflected the original electron into the hodoscopic calorimeter. The angular deflection caused by  $B_0$  was roughly proportional to the bremsstrahlung  $\gamma$ -ray energy.

the Cu radiators were in the beam to produce  $\gamma$ -rays, the rate could be a little higher, since not all  $e^-$  shed bremsstrahlung photons.

## 7.2 The Beam Test Instrument

The *GLAST* science prototype instrument was divided into three parts. The tracker consisted of 6 planes of silicon strip detectors, for precision measurement of the  $e^-e^+$  tracks. The calorimeter was composed of segmented blocks of CsI to measure deposited energy. The anti-coincidence detector (ACD) was a set of plastic scintillators read out to photodiodes via wave-shifting fibers. Each of these three components was connected to the data acquisition system of End Station A [1].

### 7.2.1 Tracker

Competing physical effects lead to the adoption of a number of tracker design configurations. Multiple scattering of the  $e^-e^+$  pair is the dominant source of error in

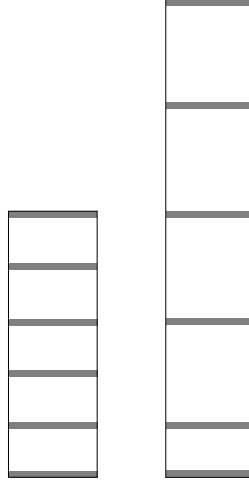


Figure 7.3: Pancake (left) and Stretch (right) tracker configurations, illustrated to scale. The gray bars represent the locations of the planes. The distance between the planes in pancake configuration was 30.0 mm; in stretch, 60.0 mm, except for the last gap, which was 30.0 mm.

reconstructing the incident angle of low-energy  $\gamma$ -rays. Multiple scattering (§8.1) refers to the process by which an electron passing through a material is deflected by many small scatters; it is generally inversely proportional to the electron energy [5]. However, at high energies the granularity of the strip pitch can cause significant errors in the angle estimations. These two competing effects make two parameters relevant to the design of a silicon-strip  $\gamma$ -ray telescope: the ratio of the strip pitch to the gap between planes, and the amount of radiator inserted between planes to facilitate conversions. Reducing the pitch-to-gap ratio improves the resolution of the instrument at high energies at the expense of increasing the number of channels—corresponding to greater instrument complexity and power usage—or of reducing the field of view. Reducing the amount of radiating foil between planes decreases the amount of multiple scattering that each electron experiences, at the expense of fewer  $\gamma$ -ray pair conversions—corresponding to a reduced detection efficiency and thus less exposure.

In order to explore this two-dimensional parameter space, the beam test instrument was built with adjustable spacing between planes, and with adjustable lead radiating foils between planes. Each of the six cards built for the instrument had two

silicon-strip detectors (SSDs) attached to it; one with strips in the  $x$  direction and one with strips in the  $y$  direction. For consistency with *GLAST* documentation, a single detector in either direction will be referred to as a *layer*, while an  $x$ - $y$  pair of detectors will be referred to as a *plane*. The test box was built with ten slots on 3 cm centers to accommodate the cards, allowing us to vary the pitch-to-gap ratio by putting the cards in different slots. The beam test SSDs were 5 cm by 5 cm square, with a strip pitch of 236  $\mu\text{m}$  and a thickness of 500  $\mu\text{m}$ . Each SSD had 192 instrumented strips, corresponding to 6 readout chips responsible for 32 strips each, and a total instrumented area of 4.6 cm by 5 cm [169].

In addition, each slot could accommodate a *radiator card*, a special card with no SSDs, but instead with a thickness of lead (Pb) foil. The distance between the lead radiators and the silicon detectors was approximately 2 mm. Radiator cards were prepared with approximately 2%  $X_0$ , 4%  $X_0$ , and 6%  $X_0$  to allow us to vary the total radiator in the instrument.

Simulations before the beam test [84] suggested two instrument configurations that were adopted for study. The first, so-called “pancake” mode, consisted of 6 planes of silicon, each containing an  $x$  and  $y$  layer, separated by 3 cm. This relatively compact configuration maximized the number of pair electrons contained within the tracker. However, at high energies when multiple scattering is small, the squat aspect ratio of this configuration accentuated the measurement error. The second mode, called “stretch,” placed the planes as far apart as experimental conditions would allow. The first five planes were spaced 6 cm apart, and the last one was spaced 3 cm apart. This configuration allowed more low-energy pairs to escape the tracker, but minimized measurement error for the high-energy pairs.

Data was taken in the stretch configuration with 2%  $X_0$ , 4%  $X_0$ , and 6%  $X_0$

Pancake	Stretch
0.00%	0.00%
1.71%	1.71%
3.71%	3.71%
	5.4%

Table 7.1: Radiation lengths of Pb available

Band Number	Energy Range	Center
0	10–20 MeV	14 MeV
1	20–50	33
2	50–100	72
3	100–200	140
4	200–500	330
5	500–1000	720
6	1–2 GeV	1.4 GeV
7	2–5	3.3
8	5–10	7.2
9	10–20	14.4

Table 7.2: Energy bands used for analysis. The approximate geometric center of the energy band was often used as the average energy, implicitly assuming an  $E^{-1}$  spectrum.

radiators, as well as with the radiator cards removed (“0%  $X_0$ ”). In the pancake configuration, data was taken with no radiators, 2%  $X_0$ , and 4%  $X_0$ . There was not enough time to take 6%  $X_0$  data in pancake configuration.

In most cases, analysis was done in ten standard energy bands to improve the statistics. The energy bands are defined in Table 7.2.

### 7.2.2 Calorimeter

Behind the silicon tracker was a prototype calorimeter made of segmented blocks of CsI(Tl). For all of the tracker data runs, the calorimeter consisted of eight layers of 6 logs, each 3 cm by 3 cm by 28 cm. Thirty-two blocks were made of CsI(Tl), and fully instrumented with photodiodes on each end. The other 16 blocks were made of Cu with holes bored into the material to simulate the equivalent number of radiation lengths of CsI(Tl). A diagram of the locations of the instrumented blocks is given in Figure 7.4. The calorimeter, built at the Naval Research Laboratory, is fully described elsewhere [57]. For the purposes of the silicon tracker data analysis, the only calorimeter measurement used was the total energy deposited in all instrumented blocks. This was found by summing the counts from the analog-to-digital counters

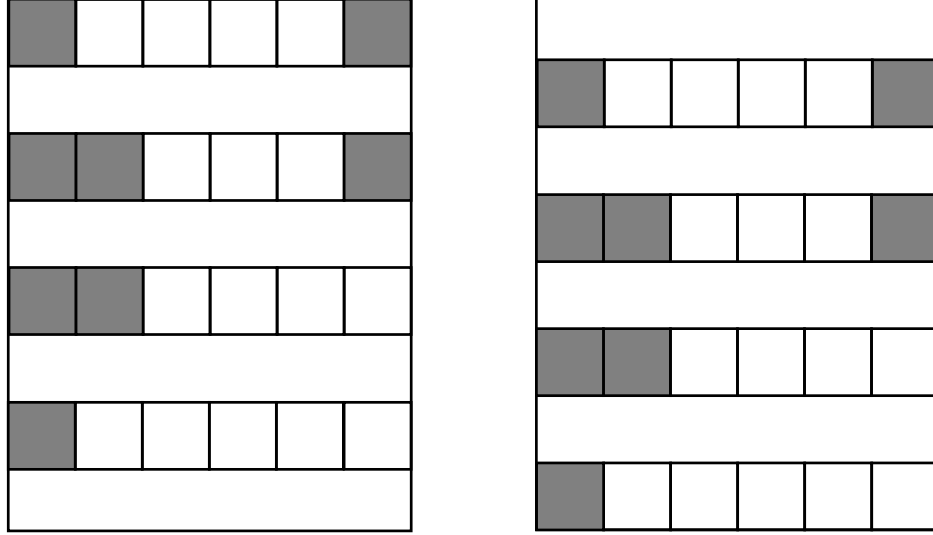


Figure 7.4: CsI(Tl) Calorimeter in each projection. Shaded blocks are non-instrumented Cu. Unshaded blocks are CsI(Tl) with PIN diodes on each end. The beam was incident from the top of the diagram.

(ADCs), subtracting the pedestals, and adjusting for the gain:

$$E_{meas} = \alpha \left( \sum \text{ADC} - 1660 \right) \quad (7.1)$$

where  $\alpha$  is 1.6 for gain 1, 0.25 for gain 4, and 0.06 for gain 7. The gain setting of the photodiodes used for measuring the energy deposition in the calorimeter blocks was recorded for each data run.

### 7.2.3 Anti-Coincidence Detector

*GLAST* will be equipped with an anti-coincidence detector (ACD) to distinguish  $\gamma$ -rays from the charged-particle background. While the ACD is designed to reject background charged particles, it is also very sensitive to the array of particles emitted from a  $\gamma$ -ray or other particle interaction in the calorimeter. High energy  $\gamma$ -rays may “self-veto” as secondary particles created in the calorimeter activate the ACD. *EGRET* was especially prone to this type of event due to its monolithic anti-coincidence scintillator, and in fact displayed a precipitous decline in sensitive area

at high energies [193]. The *GLAST* ACD will be an arrangement of plastic scintillator tiles covering the instrument which will register the passage of charged particles. The segmented tiles will provide independent measurements to facilitate background rejection while not reacting to backslash events. To test the scintillators and the associated electronics, an ACD was developed for the beam test [169].

The system set up for the beam test consisted of 15 plastic scintillators. Nine of these were arranged along the side of the silicon tracker and calorimeter, and six were placed in two layers in front of the silicon tracker. The segmented design allows the discrimination of true charged particle events from backslash by lending position information. The scintillators along the side of the beam test instrument were designed to verify this procedure.

All of the beam test scintillators were read out via waveshifting fibers to photomultiplier tubes. These fibers allowed the scintillators to be placed very close to one another, minimizing cracks through which charged particles might penetrate undetected.

### 7.3 Summary of Data

Data was collected in runs of up to two hours. The length of the run was limited by the amount of data that could be stored by the data acquisition system on one tape [1]. Over 400 runs were made over 30 days in October 1997, running 24 hours each day, 7 days each week. Approximately 30 collaboration members worked shifts to monitor the experiment and change instrumental or beam parameters as necessary. The data acquisition system recorded  $2.1 \times 10^8$  triggers, which required more than 200 gigabytes of tape. Only the  $\gamma$ -ray runs were useful for the tracker study; electron runs were used for backslash and calorimeter studies. Useful  $\gamma$ -ray events were filtered from these triggers; this process will be described in §9.2.



## 7.4 Simulations

The October 1997 beam test was just as critical for the evaluation of *GLAST* simulation techniques as it was for the evaluation of *GLAST* technology. The verification of simulation results for the beam test indicated to what extent simulations of the full *GLAST* instrument could be trusted to accurately represent instrument performance in orbit.

Simulations of the *GLAST* instrument have been successfully done using computer code called `glastsim`. The code is based on `gismo`, a toolbox of routines that simulates the interaction physics for a large number of particles with a large number of materials [3]. These particles and their interactions are taken from EGS, a highly-tuned analytical model of quantum electrodynamical interactions and transport established by the particle physics community for the simulation of high-energy physics experiments [147, 25].

For the purposes of the science prototype beam test, we further modified `glastsim` to simulate the prototype instrument that we would actually be using. In the interest of realism, as much of the experimental apparatus was included in the simulation as possible. The SLAC electron beam is nearly monochromatic (to within a few percent in energy) because of the large steering magnets which are used to bring the beam to End Station A. The simulations thus assumed a monochromatic 25 GeV electron beam, directly incident on a 3.5%  $X_0$  foil radiator. The electrons would bremsstrahlung in the radiator according to the interaction cross-section. A magnetic field then swept away the incident electron, allowing any bremsstrahlung photons to continue into the instrument. Once the  $\gamma$ -ray entered the silicon tracker, it was allowed pair-produce using the standard EGS  $\gamma$ -ray interactor.

Upon exiting (or missing) the tracker, the resulting particles were collected in a CsI(Tl) calorimeter. Since tracking the particle shower in simulations of the calorimeter are complicated and thus quite slow, some simulations were done with monoenergetic incident  $\gamma$ -rays, without a calorimeter. When a calorimeter was used, it was composed of 8 layers of 8 CsI(Tl) blocks, each 3 cm by 3 cm, for a total of 13 radiation lengths. When the Monte Carlo data was read into the analysis code, energy

deposition into blocks that were not instrumented was ignored. Furthermore, since only a few percent of the electrons incident on the Cu foil shed a bremsstrahlung  $\gamma$ -ray, it was significantly faster to simply inject a bremsstrahlung spectrum of  $\gamma$ -rays directly.

## Chapter 8

# Reconstructing Events

All telescopes require a method of converting the raw data recorded by the instrument into relevant observational parameters. For a  $\gamma$ -ray telescope, these parameters consist of information about individual photons. A bright astrophysical  $\gamma$ -ray source might have an intensity of  $10^{-6} \text{ cm}^{-2} \text{ s}^{-1}$ . *EGRET* might measure 30 photons per hour from such a source. Compare this to an ordinary light bulb, which emits something like  $10^{20}$  photons per second. Of course, each optical photon is very much less energetic. Nevertheless, if the total energy from our hypothetical  $\gamma$ -ray source had been emitted at optical frequencies instead of  $\gamma$ -rays, our telescope would receive around two billion photons per hour.

Clearly, the fact that photons arrive so rarely will profoundly influence the way we analyze our data. “Imaging” must be done statistically, with long integration times. Sometimes it may even be more advantageous to look at maps of some statistical measure, rather than directly at maps of intensity. Likelihood techniques used in analyzing photon information to derive astrophysical information for *EGRET* were discussed in Part I. Here we will concentrate on the process of deriving photon information for the basic instrument response, beginning with the mechanism of  $\gamma$ -ray pair production.

## 8.1 Pair Production

High-energy  $\gamma$ -ray telescopes work on the principle of pair production. According to the rules of quantum electrodynamics (QED), a photon passing through matter may convert into a electron-positron pair.

$$\gamma + \text{nucleus} \longrightarrow e^+ + e^- + \text{nucleus} \quad (8.1)$$

The probability of such a conversion taking place is roughly independent of the energy of the incident photon above 1 GeV, and falls off at lower energies. However, not all interactions result in pair production. At low energies, photons tend to Compton scatter more readily than pair produce. At 20 MeV, approximately 70% of interactions in Si result in pair production. At 10 MeV, close to half of interactions in Si are Compton scatters [5]. The total interaction cross section for all processes is fairly constant down to about 10-20 MeV. While the full pair-production cross section is quite a complex function of incident  $\gamma$ -ray energy, electron energy, positron energy, nuclear recoil energy, opening angle, azimuthal angle, and recoil angle [140], several simplifying assumptions give simple estimates of bulk behavior [5]. For a homogeneous material, the intensity of the incident  $\gamma$ -ray beam falls off like

$$I = I_o \exp\left(-\frac{7}{9}t/X_o\right) \quad (8.2)$$

due to all interactions, where  $t$  is the thickness of material and  $X_0$  is the radiation length of the material. Therefore the probability of a particular  $\gamma$ -ray interacting in the material is

$$P(t) = 1 - \exp\left(-\frac{7}{9}t/X_o\right) \quad (8.3)$$

**Pair Production  $\gamma$ -Ray Telescopes.**  $\gamma$ -Rays that pair produce offer an opportunity for detection. By tracking the resulting  $e^+e^-$  pair, we can estimate the incident  $\gamma$ -ray energy and direction. The reconstructed energy will be the sum of the  $e^+$  and  $e^-$  energies, corrected for energy loss in the instrument, and the incident direction of

the  $\gamma$ -ray must be the momentum-weighted average of the  $e^+$  and  $e^-$  directions. All but the lowest energy electrons detected by *GLAST* will be relativistic, so we may use the energy-weighted average of their directions to calculate the incident  $\gamma$ -ray direction.

Accurately reconstructing the particle tracks is therefore of great importance. Two effects hinder our efforts to do this. The first is multiple scattering of the electrons. ( $e^+$  and  $e^-$  will be referred to collectively as “electrons.”) At large angles, it is not Gaussian; however, the core of the distribution (out to approximately  $3\sigma$ ) is approximately Gaussian [5], with a projected width of

$$\theta_o = \frac{13.6\text{MeV}}{E} \sqrt{x/X_o} (1 + 0.038 \ln x/X_o) \quad (8.4)$$

for relativistic electrons, where  $E$  is the electron energy and  $x$  is the thickness of material traversed. In addition, there is some lateral displacement of the electron from one side of the material to the other. The rms width of the displacement distribution is given by

$$y_{rms} = \frac{1}{\sqrt{3}} x \theta_o \quad (8.5)$$

Note that multiple scattering becomes smaller, on average, with increased electron energy, and with thinner radiating material.

The second effect which complicates track reconstruction is measurement error. Most technologies proposed or used for  $\gamma$ -ray telescopes are based on wires or strips made of various materials. When an electron passes near the strip, it “fires” or records a hit. The strip pitch clearly affects the resolution of the telescope. The strip pitch divided by the gap between planes roughly determines the minimum angle that the telescope can resolve.

Given a set of strip addresses which have been hit, we must reconstruct the electron tracks and determine the parameters of the incident  $\gamma$ -ray. There may be noise hits, spurious tracks, missing hits, or ambiguous tracks. We are limited by measurement error, and by energy-dependent multiple scatter. Even if we have two well-defined tracks, we may not know the energy in each electron, only the combined energy deposited in the calorimeter. Furthermore, the  $x$  and  $y$  projections of the instrument are

read out separately. Given a track in the  $x$  projection, the question of which  $y$  track corresponds to it is ambiguous. Clearly, a good method of finding and fitting electron tracks will be critical to the accurate estimation of the incident  $\gamma$ -ray direction.

## 8.2 Track Reconstruction

The problem of establishing the most likely electron tracks falls naturally into two steps: finding and fitting. The first step consists of choosing which hits in the tracker are part of the track in question. Designing good algorithms to do this is an art; in fact, it is similar in some ways to the pattern recognition problems being worked on by computer scientists. The second step consists of making the best estimate of the track of the electron that caused those hits. The latter is a science—an optimization problem—and is by far the more tractable problem. We will address the simpler problem first.

**Least-squared Methods.** The simplest method of track fitting is the linear least-squares fit. We simply fit a straight line to all of the hits in the track. Since we expect that the total angle scattered should increase as the track proceeds through additional layers, we assume the uncertainty in the measurement to grow increasingly larger as we travel down the tracker. This method has the advantage of being very simple and fast. At high energies, the track should be very nearly straight, so the least-squared fit line will be a good approximation to the real track. However, at energies where multiple scattering is significant, a straight line is a poor approximation to the actual track. A line fit in this way will have reasonable information about the incident track direction, but its estimation of the final track position and direction may be quite poor. If we wish to extrapolate the track to the calorimeter below, we will require better estimates of the track parameters at the bottom of the silicon tracker. Furthermore, a linear least-squares fit rolls the multiple scattering and measurement error into one general error. As we have seen, these errors behave very differently in different energy limits.

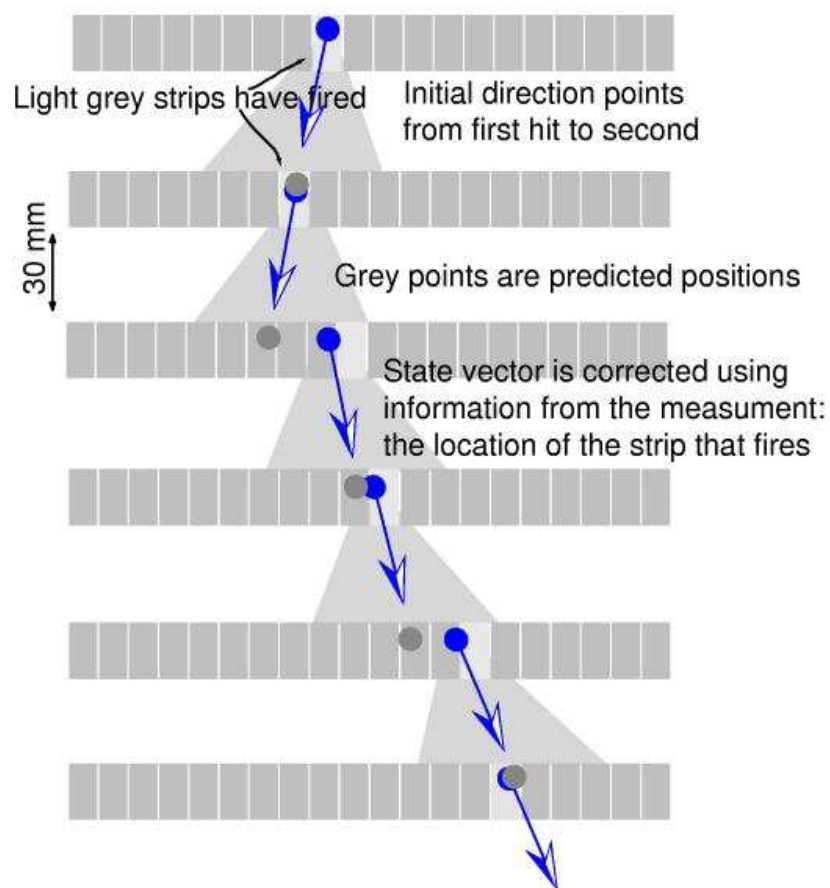


Figure 8.1: The Kalman Filtering process. A passing electron causes a strip to fire in each plane (light grey). The Kalman filter uses the current track direction (black arrow) to predict the hit location on the next plane (grey circle). The light grey area represents the range of likely directions after multiple scattering. The location of the strip which fires is used to correct the track location, and predict the track direction to the following plane.

**Kalman Filters.** Given a set of hits that make up a track, the optimal linear fitting method is called Kalman filtering [91, 85]. “Kalman filtering” is really a two-step process, consisting of a “filter” and a “smoother.” The filter begins at the first hit of a track, and makes a prediction for the location of the next hit. That prediction is refined in light of the measured hit location, and the error matrices are updated. This process, called “filtering,” continues to the end of the track (Figure 8.1). Once a track has been filtered, it is then “smoothed.” When the filtering process is finished, our estimation of the track in any given plane has no information about the locations of hits in subsequent planes. Smoothing incorporates that information. It steps back up the track from the bottom, further refining the track parameters at each step based on the information found further down the track (Figure 8.2). Frühwirth [51] developed a practical implementation of Kalman filters that is applicable to particle track fitting.

The filter must balance the competing effects of multiple scattering and measurement error. The problem simplifies immensely if either one of these is negligible. If the measurement error were negligible compared to the multiple scattering, as expected at low energies, the filter would simply “connect the dots,” making a track from one hit to the next. Most of the information about the  $\gamma$ -ray direction would come from the first two hits, where the cumulative effects of multiple scattering are the smallest. However, if the measurement error is significant and multiple scattering is negligible (as it will be for high energy photons), all hits have information, and we should essentially fit a straight line to the hits. The Kalman filter balances these limits properly for all energies, and thus earns its title as the optimal linear filter; in the limit that all errors and multiple scattering are Gaussian, it is the optimal filter. That means that if all is Gaussian, it is completely equivalent to both a  $\chi^2$  fit and a maximum likelihood fit. The Kalman Filter was chosen for analysis of the beam test data. Accordingly, we will examine the method and its implementation in some detail in §8.3.

**Track finding.** Track finding is a more subjective problem. The identification of which hits belong to a track is a pattern recognition problem which does not admit



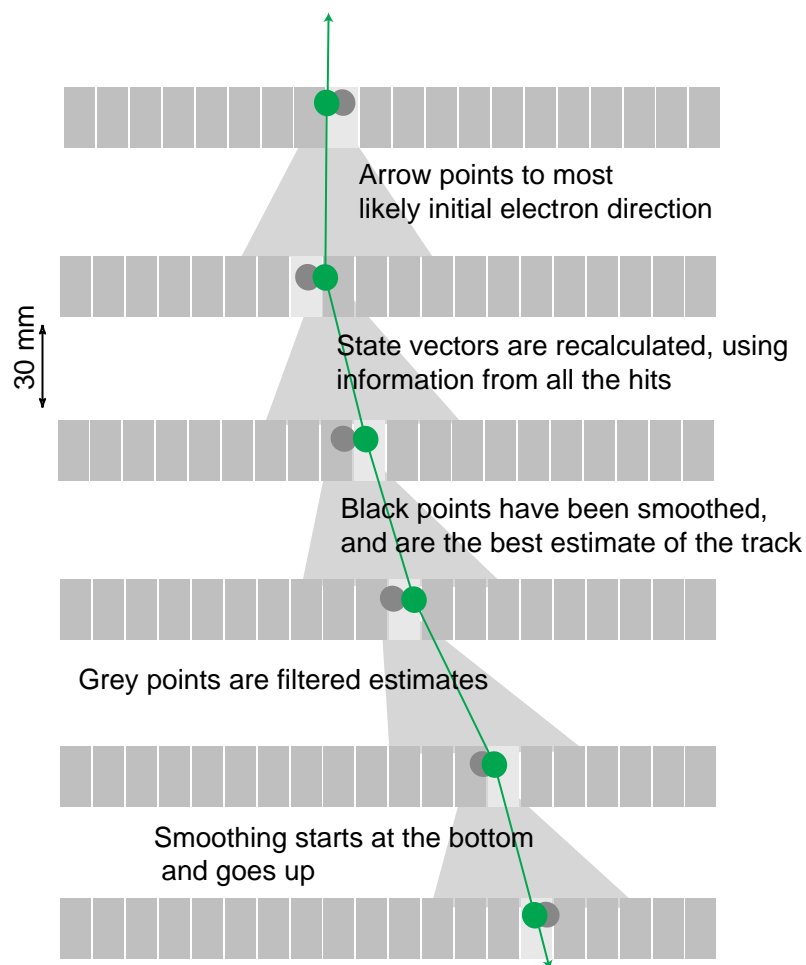


Figure 8.2: The Kalman Smoothing process. Starting at the bottom and working up, the track estimate (grey circles) is corrected further (black track), based on information about the track below the plane in question.

an analytic solution. The basic algorithm we have adopted is based on the filtering procedure described above. At each plane, we use a Kalman filter to predict the most likely location of the hit. We then assume, in most cases, that the nearest hit to that predicted location is the one which belongs to the track. This simple criterion is complicated by caveats that allow for tracks leaving the tracker and for tracks sharing the same hit. The complete algorithm will be discussed in §8.4.

### 8.3 The Annotated Kalman Filtering Formulae

We base the Kalman filtering equations on those found in Frühwirth [51]. At each instrument layer, we have the projected state vector, the “filtered” state vector, and the “smoothed” state vector. The Kalman filter will successively calculate these estimates of the track parameters. The state vector will contain all parameters of interest about the track. These might include the lateral position in  $x$ ,  $y$ , or both; the height  $z$  in the instrument; the direction of the track as either angles or slopes; and the energy of the track. The state vector may be chosen to contain information from only one projection, separating the problem into fitting the  $x$  and  $y$  projections separately, or it may contain all parameters for a simultaneous fit. However, a state vector of length  $n$  will require inversion of  $n \times n$  matrices. Computationally, it may be advantageous to separate independent variables into separate state vectors, and fit them separately. For each layer, then, we have a system equation of the form

$$\mathbf{x}_k = \mathbf{F}_{k-1} \mathbf{x}_{k-1} + \mathbf{w}_{k-1} \quad (8.6)$$

where  $\mathbf{x}_k$  is the state vector containing track parameters in plane  $k$ , the  $\mathbf{F}$  matrix is the propagator from one layer to the next, and the random variable  $\mathbf{w}_{k-1}$  is the multiple scattering.

The  $\mathbf{F}$  matrix takes the state vector on one plane to the state vector on the next plane. In general, this means it will combine directional information with position information to compute a new position. In the absence of a magnetic field, the direction will not change. The  $\mathbf{F}$  matrix is indexed since it implicitly contains information

about the gap between one plane and the next, which may not be the same for all planes.

The Kalman filter must also consider the measurement process. Given a true track position  $\mathbf{x}$ , we will measure

$$\mathbf{m}_k = \mathbf{H}_k \mathbf{x}_k + \epsilon_k \quad (8.7)$$

where  $\mathbf{m}_k$  is the measurement that we make,  $\mathbf{H}$  is the measurement matrix, and the random variable  $\epsilon_k$  is the measurement error.

Also note that the dimensions of  $\mathbf{x}$  and  $\mathbf{m}$  may not be the same. If all properties of the track are not directly measured,  $\mathbf{H}$  will not be square. Again, remember that we can have a separate  $\mathbf{H}_k$  for every plane. If silicon tracker data were combined with data from a sampling calorimeter, the calorimeter's  $\mathbf{H}$  matrix would include a term indicating an energy measurement.

The second part of the system and measurement equations is the random variables we use to represent multiple scattering ( $\mathbf{w}_k$ ) and measurement error ( $\epsilon_k$ ). If their expectation values are zero, it will be sufficient to consider their covariance matrices. By suitably defining our state vectors and other matrices, this condition can always be satisfied. For notational convenience, following Frühwirth, we define

$$\mathbf{Q}_k = \text{cov} \{ \mathbf{w}_k \} \quad (8.8)$$

$$\mathbf{V}_k = \mathbf{G}_k^{-1} = \text{cov} \{ \epsilon_k \} \quad (8.9)$$

$$(8.10)$$

It is helpful to make the semantic distinction between multiple *scattering* and measurement *error*. Both appear as random variables in our equations, but it is important to remember that measurement error is a description of our imperfect measurement, while multiple scattering is a physical distribution.

The displacement in the detector plane of the track due to multiple scattering is correlated with the angle through which the track scatters [5]. If  $z$  is the thickness

of the detector, and  $\theta_o$  is the rms multiple scattering width given by equation (8.4), then the multiple scattering covariance matrix is

$$\mathbf{Q} = \begin{pmatrix} z^2\theta_o^2/3 & z\theta_o^2/2 \\ z\theta_o^2/2 & \theta_o^2 \end{pmatrix} \quad (8.11)$$

assuming  $\mathbf{w}$  has two components, horizontal position  $x$  and track angle  $\theta$ .

Finally, we have the covariance matrix of our state vector:

$$\mathbf{C}_k = \text{cov} \{ \mathbf{x}_k - \mathbf{x}_{k,true} \} \quad (8.12)$$

This will provide our estimate of the errors in our estimate of the track parameters; that is, the estimate of the point-spread function for each electron track. The details of this estimation may be found in §8.9.

### 8.3.1 The Filtering Equations

Now, we can write down the prediction, filtering, and smoothing equations. Note that the equations are only stated as found in Frühwirth, not derived here. First, we predict the next position, using the propagator and the position on the previous plane:

$$\mathbf{x}_{k,proj} = \mathbf{F}_{k-1}\mathbf{x}_{k-1} \quad (8.13)$$

and the next covariance matrix, found by adding to the predicted covariance the effects of the multiple scattering that happens in plane  $k - 1$ :

$$\mathbf{C}_{k,proj} = \mathbf{F}_{k-1}\mathbf{C}_{k-1}\mathbf{F}_{k-1}^T + \mathbf{Q}_{k-1} \quad (8.14)$$

These equations express the propagation, according to  $\mathbf{F}$ , of the position and errors, with the addition of the multiple scattering covariance.

The filtering process refines the predicted position by using information from the measurement on that plane. We must first refine the covariance matrix:

$$\mathbf{C}_k = \left[ (\mathbf{C}_{k,proj})^{-1} + \mathbf{H}_k^T \mathbf{G}_k \mathbf{H}_k \right]^{-1} \quad (8.15)$$

Recall that  $\mathbf{G}_k$  is the inverse of the measurement error covariance matrix. If measurement errors were huge, then the measurement would contribute very little information.  $\mathbf{G}_k$  would be nearly zero, and the error matrix would be just the previous error matrix propagated to the next plane.

This is a good place to consider a limiting case. If all of our state vectors were scalars,  $\mathbf{C}$  would look like  $\sigma^2$ . Then (8.15) would look like

$$\sigma_{filtered}^2 = \left( 1/\sigma_{predicted}^2 + 1/\sigma_{measurement}^2 \right)^{-1} \quad (8.16)$$

We are simply weighting our estimate of  $\sigma$  by the quality of the measurements.

Using our refined  $\mathbf{C}_k$ , we can calculate

$$\mathbf{x}_k = \mathbf{C}_k \left[ (\mathbf{C}_{k,proj})^{-1} \mathbf{x}_{k,proj} + \mathbf{H}_k^T \mathbf{G}_k \mathbf{m}_k \right] \quad (8.17)$$

Again, the size of  $\mathbf{G}_k$  controls how heavily the measurement is weighted.

In our limiting case, we now weight our track estimate by the quality of the measurement: (8.17) becomes

$$\frac{x_{filtered}}{\sigma_{filtered}^2} = \frac{x_{predicted}}{\sigma_{predicted}^2} + \frac{x_{measured}}{\sigma_{measured}^2} \quad (8.18)$$

### 8.3.2 The Smoothing Equations

So far, all the equations have only used information about the measurements taken either on the same plane, or “upstream” of the current plane. Smoothing is the process of further refining each position estimate in light of the information from all the measurements, upstream and downstream of the current plane. We first calculate an auxiliary matrix  $\mathbf{A}$ :

$$\mathbf{A}_k = \mathbf{C}_k \mathbf{F}_k^T (\mathbf{C}_{k+1,proj})^{-1} \quad (8.19)$$

Then the smoothed position and covariance estimates are

$$\mathbf{x}_{k,smooth} = \mathbf{x}_k + \mathbf{A}_k(\mathbf{x}_{k+1,smooth} - \mathbf{x}_{k+1,proj}) \quad (8.20)$$

$$\mathbf{C}_{k,smooth} = \mathbf{C}_k + \mathbf{A}_k(\mathbf{C}_{k+1,smooth} - \mathbf{C}_{k+1,proj})\mathbf{A}_k^T \quad (8.21)$$

The difference between the smoothed and projected versions of  $\mathbf{x}_k$  and  $\mathbf{C}_k$  may be thought of as the effect on the state vector and covariance matrix of the data from planes  $k$  and below. Now we need to know how to calculate the influence of that data on the estimates for the current plane. The key is  $\mathbf{A}_k$ . First, consider the case with no multiple scattering, when  $\mathbf{Q}_k$  is zero. Plugging into (8.19) from (8.14) after adjusting indices, we find

$$\mathbf{A}_k = \mathbf{C}_k \mathbf{F}_k^T ((\mathbf{F}_k^T)^{-1} \mathbf{C}_k^{-1} \mathbf{F}_k^{-1}) = \mathbf{F}_k^{-1} \quad (8.22)$$

In this case,  $\mathbf{A}$  is just the back-propagator, taking  $\mathbf{x}_{k+1}$  to  $\mathbf{x}_k$ . Then (8.20) just propagates  $\delta\mathbf{x}_{k+1}$  back to plane  $k$ , exactly what we would expect with no multiple scattering to complicate the issue.

The limit that multiple scattering is large compared to the covariance matrix is more complicated. Returning to the scalar case, the various  $\mathbf{C}$ 's become  $\sigma^2$ , and  $\mathbf{F}$  becomes a scalar. Then our  $\mathbf{A}$  becomes

$$a = \frac{f\sigma_{k,filtered}^2}{\sigma_{k+1,proj}^2} \quad (8.23)$$

Again plugging in from the scalar equivalent of (8.14), we end up with

$$a = \frac{f\sigma_{k,filtered}^2}{f^2\sigma_{k,filtered}^2 + \sigma_{ms}^2} \quad (8.24)$$

In the limit that  $\sigma_{k,filtered}^2 \ll \sigma_{ms}^2$ , this simplifies to

$$a \approx \frac{f\sigma_{k,filtered}^2}{\sigma_{ms}^2} \quad (8.25)$$

So, the bigger the expected multiple scattering, the more we discount the information

in the planes below. In fact, both extremes can be seen in the scalar version: as multiple scatter goes to zero in (8.24),  $a$  approaches unity—the information from later planes is not discounted at all.

Now we have calculated the smoothed state vectors and covariance matrices at all points along the track. These revised estimates represent the optimal linear filter of the particle track. If the measurement and multiple scattering errors were Gaussian, it would be the optimal estimate of the track, and equivalent to a maximum likelihood estimate. The smoothed state vector for the first plane gives us the initial track direction, while the smoothed covariance matrix for the first plane gives us the “point-spread width” for that track.

### 8.3.3 Goodness of Fit

If the Kalman filter, under some assumptions, is identical to both least-squared fitting and maximum likelihood, we should demand that it produce a  $\chi^2$  value or a likelihood as a measure of its goodness of fit. In fact, it does produce a “running  $\chi^2$ ” as it filters and smooths.

For each plane, we find the residual vector

$$\mathbf{r}_k = \mathbf{m}_k - \mathbf{H}_k \mathbf{x}_k \quad (8.26)$$

and the covariance matrix of the filtered residuals

$$\mathbf{R}_k = \mathbf{V}_k - \mathbf{H}_k \mathbf{C}_k \mathbf{H}_k^T \quad (8.27)$$

The incremental  $\chi^2$  is then

$$\chi_+^2 = \mathbf{r}_k^T \mathbf{R}_k^{-1} \mathbf{r}_k \quad (8.28)$$

The total  $\chi^2$  of the track is given by the sum of the  $\chi^2$  contributions for each plane.

The smoothed incremental  $\chi^2$  can be similarly calculated:

$$\mathbf{r}_{k,smooth} = \mathbf{m}_{k,smooth} - \mathbf{H}_k \mathbf{x}_{k,smooth} \quad (8.29)$$

$$\mathbf{R}_{k,smooth} = \mathbf{V}_k - \mathbf{H}_k \mathbf{C}_{k,smooth} \mathbf{H}_k^T \quad (8.30)$$

$$\chi_+^2 = \mathbf{r}_{k,smooth}^T \mathbf{R}_{k,smooth}^{-1} \mathbf{r}_{k,smooth} \quad (8.31)$$

The incremental  $\chi^2$  for each plane is distributed as  $\chi^2(m_k)$ , where  $m_k$  is the dimension of  $\mathbf{m}_k$  [51]. In fact, it is precisely in this sense that we may call it  $\chi^2$ . Since it measures residuals due to multiple scattering as well as those due to measurement error, strictly speaking it is  $-2 \ln \mathcal{L}$ , which of course is distributed as  $\chi^2$  [211, 36].

This test may be used as a way to identify track outliers. A measurement with a  $\chi^2$  value corresponding to the  $(1 - \alpha)$  quantile may be rejected as not belonging to the track. This process will reject a measurement which actually is part of the track with probability  $\alpha$ .

The complete set of Kalman filtering equations is summarized in Appendix B.

### 8.3.4 Kalman Filter Implementation for the Beam Test

In order to analyze the data from the October 1997 beam test, the Kalman filtering equations above were implemented in a C++ program called `tjrecon`. This program combined track finding and track fitting into one package which could analyze both beam test and Monte Carlo data. The track finding algorithms will be discussed in §8.4.

To maintain generality, the implementation was designed to be as flexible as possible. The  $x$  and  $y$  projections were fit separately, and their results combined after the fitting process. The state vector was chosen to be:

$$\mathbf{x}_k = \begin{pmatrix} \text{horizontal position} \\ \text{track slope} \\ \text{current energy} \end{pmatrix} \quad (8.32)$$

The propagation matrix was then simply (aside from unit conversions)

$$\mathbf{F} = \begin{pmatrix} 1 & 1 & 0 \\ 0 & 1 & 0 \\ 0 & 0 & 1 \end{pmatrix} \quad (8.33)$$



Recall from equation (8.4) that the multiple scattering *angle* is approximately Gaussian distributed. Since we are using the slope of the track, the (1,2) component of  $\mathbf{F}$  should really be  $\tan(\text{track slope})$ . Of course, this destroys the linearity of the propagation equation, and with it the Kalman filter. So, we assume that the track slope will be small so that  $\tan \theta \approx \theta$ . Consequences of relaxing this requirement will be discussed in §8.10.

We assumed a measurement vector  $\mathbf{m}_k$  with an energy component, to allow the possibility of extending the Kalman filter to the calorimeter.

$$\mathbf{m}_k = \begin{pmatrix} \text{strip number} \\ \text{current energy} \end{pmatrix} \quad (8.34)$$

Since there was no energy measurement information in the tracker, our  $\mathbf{H}$  matrix was, for all planes,

$$\mathbf{H}_k = \begin{pmatrix} 1 & 0 & 0 \\ 0 & 0 & 0 \end{pmatrix} \quad (8.35)$$

## 8.4 Track Finding Algorithm

Track finding is significantly more difficult than track fitting in the following sense: it is impossible to rigorously prove that one track finding algorithm is better than another. One must implement both algorithms and run them on the data in question.

### 8.4.1 The Exhaustive Search

An exhaustive combinatorial search is the exception; it is guaranteed to find the best track. It is also simple to implement: for every possible combination of hits for each of the two tracks, apply the Kalman filter and look at the  $\chi^2$ . The best tracks are the combination that give you the lowest total  $\chi^2$ . However, the method soon becomes computationally infeasible. For a single track, the number of combinations  $n$  to try is roughly

$$n = p^h$$

where  $p$  is the number of planes and  $h$  is the average number of hits. For the beam test,  $p$  was 6, and  $h$  was typically between zero and 6. This would imply several hundred possibilities for each track in each event; an achievement which would be possible, though probably not at real-time speed. However, a single tower of *GLAST* will have 16 planes and could have as many as 10 hits per plane. An exhaustive search would require  $10^{12}$  trials, which is clearly not feasible for the expected data rates.

### 8.4.2 Beam Test Algorithm

In an attempt to avoid the computational complexity of an exhaustive search, we will try to make a good initial guess for the track, then vary that guess in order to optimize the goodness of fit. The Kalman filter naturally suggests the outline of a track finding algorithm, based on the prediction of the track location in the next plane. However, there are myriad details of such an algorithm left unconstrained. Unfortunately, there is no continuous metric to guide our choices—the only metric by which to compare different algorithms is to implement them, and see which one does the best. The specific choices we made in designing an algorithm for the beam test were verified on Monte Carlo data to succeed rather well in reconstructing events. However, we can make no claim that this algorithm is optimal, nor that it will be the basis for an algorithm for use in *GLAST*.

To make an initial guess for the track location, we find the first plane with a hit. Presumably, the  $\gamma$ -ray converted in the lead above this plane, or in the plane itself. We assign the leftmost hit in the first plane to the track, and the leftmost hit in the second plane to be the second hit in the track. These will serve as initial guesses, but we will explore other possibilities later. Given these two hits, we may run the Kalman filter, predicting a state vector, and therefore a position, for the third plane. We assume that the closest hit to the predicted position is part of the track. Continuing this procedure to the bottom of the tracker yields our initial guess.

The metric for determining a good track is the total  $\chi^2$  calculated in equation (8.29) in a slightly modified form. Because of the existence of noise, double hits, and the possibility of tracks leaving the instrument, we construct penalties which

we add to the total  $\chi^2$  when a track makes an undesirable choice of hits. This is perfectly acceptable in the language of likelihoods—we have additional information to suggest that such a track is unlikely, so we subtract from the  $\ln \mathcal{L}$  of that track. However, while the relative sizes of some penalties may be rigorously derived, their actual values must be determined empirically.

There are two special cases that must be considered when making our initial track guess. The first is the possibility that the track projects to a horizontal location outside the tracker. In that case, the code creates a “virtual” hit with a position outside the tracker. The track must pay a substantial penalty to its  $\chi^2$  in order to use this hit.

The second special case involves the so-called “noisy strips.” It was found (§8.6) that a number of strips were defective. They were either completely unresponsive, never recording a hit, or they were very noisy, recording a hit even when no electron passed through. All of these strips were marked as “noisy,” and masked off. Nevertheless, the possibility remained that an electron actually did pass through the noisy strip. In order to allow that possibility, the algorithm checks for noisy strips near the projected track position. It then creates virtual hits at each noisy strip within a small (10 strip) radius around the projected position. The track must add a penalty to its  $\chi^2$  in order to use a noisy hit.

It is assumed that each event contains an  $e^-e^+$  pair. Once the first track guess has been made, a second track is proposed, starting with the same hit in the first layer and the rightmost hit in the second layer. This track guess is made in the same way as the first, yielding a pair of initial track guesses.

**Track Optimization.** Once an initial track is established for each electron, several steps are taken to optimize the choice of hits. First, the two tracks are untangled so they do not cross, regardless of whether the respective  $\chi^2$  values decrease by doing so. Subsequent track optimization proceeds more smoothly if the tracks are initially untangled. This subsequent optimization will allow tracks to cross if that is justified by the data.

On each plane, there may be hits which are not a part of either of the tracks. The

algorithm next checks each of these to see if replacing any hit in either track with an unclaimed hit will improve the fit. The free hit is substituted, and following projected positions are re-evaluated, substituting nearby hits if appropriate.

Then the hits of the two tracks are swapped, plane by plane, to see if swapping hits will increase the total  $\chi^2$  of both tracks.

The last part of the track finding algorithm consists of checking the possibility that a track may have left the tracker. Often, a track may take a sharp scatter to leave the tracker, with the result that the predicted position is inside the tracker. The large penalty on leaving the tracker prevents tracks from choosing this virtual hit unjustifiably, but the even larger penalty on sharing hits prevents unrealistic swerves in the track to make a single hit.

Finally, the issue of terminating tracks must be addressed. For example, if one track in the  $x$ -projection leaves the tracker, then one of the tracks in the  $y$ -projection must be terminated. To determine which track has left, it is assumed that the track with the higher  $\chi^2$  probably has swerved precipitously to incorporate hits that do not belong to it. These hits reside on planes below that at which the track left the tracker. Therefore, the track is terminated at that plane, and is then taken to have no further hits.

A summary of the track finding algorithm may be found in Appendix C.

## 8.5 Measurement Error and Multiple Scatter Estimates

Of critical importance are the values used for the measurement error and multiple scattering. For the measurement error, we assume that any electron coming within one-half the strip pitch on either side of the strip will cause it to fire. This would result in a square distributions. The Gaussian with the same mean and variance has a standard deviation of the box width over  $\sqrt{12}$ . (This is easily shown: the variance of a distribution is its second moment, so we find  $\int_{-1/2}^{+1/2} x^2 P(x) dx$ . For a square normalized distribution,  $P(x) = 1$ , and the integral equals  $1/12$ ; see Figure 8.3.) There was no

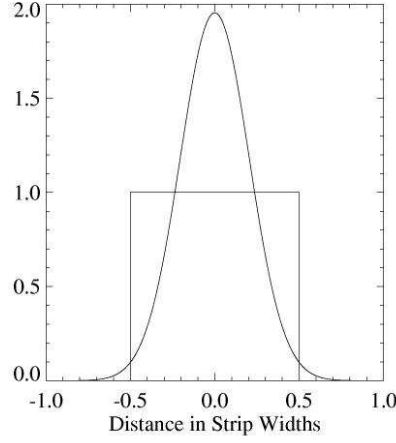


Figure 8.3: Measurement error distributions. The Gaussian approximation and square approximation to the measurement error distribution. Both are normalized and have variance  $1/12$ .

energy measurement, so its variance is arbitrary.

$$\mathbf{V} = \begin{pmatrix} 1/12 & 0 \\ 0 & 1 \end{pmatrix} \quad (8.36)$$

in units of strips [5].

According to equation (8.4), multiple scattering depends on energy. We must therefore establish the energy of the electron before we begin to fit its track. A sampling calorimeter could, in principle, provide this information. Otherwise, some approximation will have to be made. For the beam test, we assumed that the energy in each track was half the calorimeter measured energy. The thickness of the SSDs was  $500 \mu\text{m}$ , or about twice the strip pitch. From the multiple scattering equations, it follows that the multiple scattering covariance matrix  $\mathbf{Q}$  should be approximately

$$\mathbf{Q} = \begin{pmatrix} \frac{1}{12}\theta_o^2 & \frac{1}{4}\theta_o^2 & 0 \\ \frac{1}{4}\theta_o^2 & \theta_o^2 & 0 \\ 0 & 0 & 1 \end{pmatrix} \quad (8.37)$$

If the state vector were to carry a meaningful energy estimate, the (3,3) component

of  $Q$  should be the variance of the energy loss by the electron as it passes through the detector. However, the distribution of energy losses suffered by electrons passing through material is not at all well described by a Gaussian, and special care must be taken to account for these distributions [184]. Potential improvements to account for these effects are discussed in §8.8.

## 8.6 Noise

Even before the beam test actually began, it became clear that there would be some dead strips that never fire, and some noisy strips that fire far too often. At the time of the beam test, the *GLAST* collaboration did not have the capability to wire bond the individual silicon strips to the front-end readout chips. Therefore, a private company was contracted to perform the wire bonding. When the detectors were returned from the wire bonder, several of the channels drew significantly more current than they had before the wire bonding. Subsequent visual inspection revealed obvious mechanical damage to several of the strips in the form of scratches; in addition, some of the bonds were of inferior quality. Unfortunately, the detectors were returned from the contractor only one week before the beam test began, and no repair was feasible. We were thus left to incorporate the dead and noisy strips into our software analysis.

For our purposes, both dead and noisy strips were treated in the same way, and will be referred to as “noisy.” Such noisy strips will clearly confuse the track finding routines, and they must be dealt with.

Initially it was thought by many that there would not be any noisy strips at all in silicon strip detectors. In fact, carefully prepared silicon strip detectors do exhibit very few noisy strips. However, the prototypical nature of the beam test instrument, and especially the necessity of outsourcing some fabrication, led to several types of noise (Figure 8.4).

First of all, about 2/3 of the planes exhibited one or a few strips with high occupancy—typically higher than about 20% of triggers. In addition, there were also a fair number of strips which were dead. The reconstruction code merely identified these strips and flagged them for the reconstruction routines.

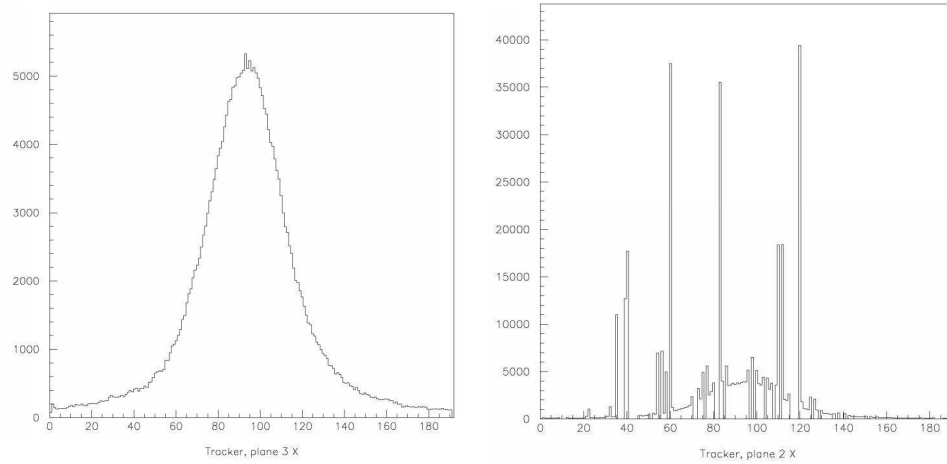


Figure 8.4: Occupancies in two planes during a typical run (Run 376). The plane on the left is almost completely noise free; all recorded hits were due to electrons passing through the plane. The plane on the right was mishandled by an outside wire-bonding contractor; it displayed excessive noise. The Gaussian shape of the real electron hits can be seen between the noisy channels.

In addition, there were two special planes to worry about. The first was a  $y$ -layer with a malfunctioning readout chip. The silicon strips connected to this chip were independently tested and found to work correctly; however, the readout chip reported a set of 32 strips to be either (almost) all on, or all off. The strips numbers were approximately 32 through 64.

The other special plane was the so-called noisy plane. This was an  $x$ -plane that exhibited a large number of noisy strips. The reasons for the large numbers of noisy strips has been traced to some quality assurance problems; they are detailed elsewhere [169].

The first attempt at identifying noisy strips was done by hand. Strips were noted as noisy when they appeared to have a higher occupancy than expected based on other nearby strips. This method proved tedious in light of the number of strips involved, and the fact the the noisy strips are not always constant between runs. On a gross level, the location of the noisy strips changed several times during the beam test as a result of the physical rearrangement of the planes within the tracker.

Clearly, noisy strips moved with the planes. In addition, several studies of the effect of different discriminator thresholds changed the noise levels.

For these reasons, we decided to automate the noise finding procedure. The algorithm works as follows: first, all strips with an occupancy above 15% were marked as “dead.” For our purposes, we flagged dead strips and excessively noisy strips in the same way. Then we looked for the plane with the bad chip. This was done by checking each  $y$ -plane in strips 32-34 and strip 60. If they were the same to within a few percent, then that plane was assumed to hold the bad chip. The entire range from 32-64 was marked as dead.

Next we looked for noisy strips in the wings of the distribution. Starting at strip 95 (approximately the center of the plane) we moved out to the left until the number of counts had dropped by a factor of 5.5 from its peak value, ignoring any dead strips. We then continued to the left and marked as dead any strip with more than one fifth the number counts as the maximum channel. The entire process was independently repeated for the right side.

Finally, we fit a Gaussian to the core of the distribution. The tails were not fit, since they were clearly non-Gaussian. Any strip with more than 130% of the hits predicted by the fit is marked as noisy. The Gaussian fit roughly represents the number of legitimate hits, and any additional hits are noise. Thus, we throw away strips where more than 30% of their hits are noise hits.

The resulting list of noisy strips is passed to the reconstruction routines, which ignore all hits from those strips.

## 8.7 Energy

Energy resolution is an important part of any  $\gamma$ -ray telescope. Good measurements of the spectra of astrophysical sources and their cutoffs offer insight into their energy-generation mechanisms. Good energy resolution is also important for good  $\gamma$ -ray reconstruction. To conserve momentum, the  $\gamma$ -ray direction must be a energy-weighted average of the  $e^-$  and  $e^+$  directions. Furthermore, the Kalman filter estimate of the



electron track depends on the expected multiple scattering, inversely proportional to the energy of the electron.

### 8.7.1 Energy Splitting

For these reasons, it is very useful to determine the energies of each electron. A useful first approximation is to simply assume each track has half the total energy measured in the calorimeter. This is a good enough approximation to allow reconstruction of the tracks. One might hope that an iterative approach would allow better energy resolution and better track fitting. We can imagine varying the fraction of energy in each track to maximize the likelihood. The energy split which produces the maximum total likelihood would be the most likely energy split.

This method was implemented, but it was unstable. In every case, the maximum likelihood energy splitting put all the energy in the straighter track, with no energy in the other track. This instability is due to the non-Gaussian tails on the multiple scattering distribution, as well as the small angle approximation we made in the Kalman filter. Tracks make large scatters much more frequently than would be expected from a Gaussian distribution. In order to make these large scatters reasonably probable, the Kalman filter radically lowers the track energy. This means that the track with a large scatter will have a grossly underestimated energy. Some possible improvements on this method will be discussed in §8.8.

### 8.7.2 Energy Dispersion

Of course, the energy measured by the calorimeter is not the true energy. In the case of the beam test, portions of the calorimeter volume were not even instrumented. Therefore, we must expect some energy dispersion. We used the simplest method of estimating total energy from the calorimeter. Eric Grove of NRL [57] provided us with a simple function (equation (7.1)) to translate raw analog-to-digital readout counts and gain settings to deposited energy. We did not try to correct for shower leakage by fitting the shower profile, or to try to separate the energy deposited by each electron.

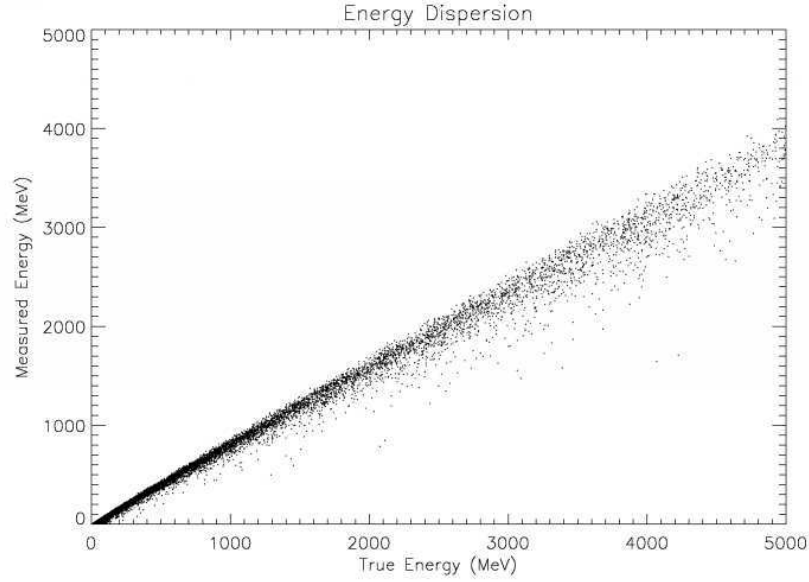


Figure 8.5: Measured energy vs. true energy in the Monte Carlo calorimeter. Measured energies are about 20% lower than true energies, since the calorimeter does not collect all of the  $\gamma$ -ray energy. In addition, the width of the measured energy distribution at any constant true energy is about another 20%.

The hodoscopic calorimeter (§7.1), which measured the energy of the “leftover” incident beam electron, allowed a rough calibration of the  $\gamma$ -ray energy. However, this measurement was only good to an accuracy of about 250 MeV. The hodoscopic calorimeter did allow the detection of some events with multiple beam electrons in a single pulse. These events could be identified when more than one leaded-glass block of the hodoscopic calorimeter recorded energy deposition.

From 10 MeV to several GeV, we compared the energy deposited in the Monte Carlo simulation of the calorimeter with the true energies of the particles injected into the simulation (Figure 8.5). Over most of the range, the calorimeter detected about 80% of the incident energy. The distribution was far from symmetric; as expected, many higher-energy photons were recorded as lower-energy photons, because of energy leakage out of the back and sides of the calorimeter as well as energy deposition in non-instrumented blocks.

## 8.8 Potential Improvements

There are a number of potential improvements to the silicon tracker analysis. Most of these would make very little difference for the results of the beam test—largely because they would affect both the actual beam test data and the Monte Carlo simulations in the same way. However, they may be quite important for track finding and fitting of *GLAST* data.

### 8.8.1 Track Fitting

**Improve estimate of measurement error distribution.** The probability that a given strip will fire is not really a boxcar, of width one strip, centered on the strip. In fact, it is a complicated function of the collection area geometry and bias voltage on the strip. It is plausible, and empirically verified, that often two adjacent strips will fire. This can occur when the electron passes between the strips, depositing enough energy into each of them to raise their potential over the threshold, or when the electron passes through the silicon at an angle, depositing energy in more than one strip. Currently, the hit which is more easily incorporated into the track is selected. Clearly, there is information in the fact that the other strip has also fired. A careful analysis of the probability of each strip firing as a function of the electron position would allow an accurate characterization of the probability of the true electron position given that both strips fired. The width of this distribution could then be used in the measurement error covariance matrix  $\mathbf{V}$  instead of the current  $1/12$  times the strip pitch.

**Transform multiple scattering distribution to Gaussian.** The Kalman filtering formalism is fast and accurate because it assumes distributions are Gaussian. However, nowhere does it require that the state vector be composed of physically meaningful values. It may be possible to find a function that would transform the multiple scattering distribution to something more nearly Gaussian. In that case, the state vector would contain the transformed variable instead of track slope. This would result in better fits, and might allow energy estimation from the track shape. The

Kalman filter would find the most likely state vectors, yielding physically meaningful information via the inverse transformation.

**Transform measurement error distribution to Gaussian.** It is unlikely that a more accurate measurement error distribution like that described above would be Gaussian. However, if a simple transformation would make it nearly Gaussian, we would achieve the same improvement as described for multiple scattering.

**Account for total material traversed.** Since both multiple scattering and energy loss depend on the amount of material that the electron traverses, electrons that cross the planes at a steep angle will be scattered more and will lose more energy. Unfortunately, this is an inherently non-linear phenomenon; large scattering leads to greater likelihood of crossing a plane at a steep angle, which leads to greater likelihood of large scattering.

**Require agreement between calorimeter and tracker reconstructed directions.** By analyzing the shape of the electromagnetic shower in the calorimeter, it is possible to estimate an incident direction of the particle. This information should be combined with the tracker reconstruction to find the best estimate of the incident  $\gamma$ -ray using all available information.

### 8.8.2 Track Finding

**Exhaustively try the first two points in track.** While a complete exhaustive search for the best track will be infeasible for *GLAST*, trying all possibilities of the first two or three planes in the track would be possible. Since the first few points are the most important in determining the rest of the track, this would increase the probability that the best track is actually found.

**Require vertex in material.** Pair production can only occur in the presence of nuclei in order to satisfy momentum and energy conservation. Therefore we can expect the two electron tracks to project back to a common vertex which is in high-Z

material. Since the conversion may well happen in lead, we may not have a measurement of the electrons at the vertex. However, we know the precise position of the lead foil, so the requirement that the vertex lie in high-Z material will improve the estimates of the tracks.

**Account for tracks which start with a dead strip.** It may happen that a  $\gamma$ -ray converts close to a dead strip. In that case, the first plane will not record a measurement of the track. The algorithm designed for the beam test would assume that the conversion actually happened in the next plane. However, it should be very rare that the conversion happens near a dead strip in both  $x$  and  $y$ . Furthermore, a fit track can be extended upwards to see if it could have converted in a dead strip above. Therefore, it may be possible to identify situations in which the first hit of the track is missing.

**Assign penalties to individual strips according to occupancy.** Currently, dead strips and noisy strips are masked identically, and all are assigned the same penalty for track finding. However, some of the noisy strips contain significant information. For a strip with a relatively low occupancy, many or most of the hits recorded may be due to actual electron tracks. A better penalty scheme would find the occupancy of each strip, and assign larger penalties to strips with higher occupancies. The magnitude of the penalty would be proportional to the likelihood that a hit registered in that strip was actually noise.

**Use empty triggers to find noisy strips.** The occupancy of each strip could be measured by examining which strips are hit when there is nothing in the silicon tracker. For the beam test, this could be done by looking at triggers in which the beam electron did not bremsstrahlung in the Cu foil. For *GLAST*, this can be done by reading out the tracker when there has not been a trigger. Careful establishment of the occupancies, remeasured frequently, would allow accurate penalties to be set for each strip.

### 8.8.3 Energy Estimations

**Take into account energy loss per plane.** It would be very easy to include energy loss in each plane. The energy loss in a material is well characterized. The (3,3) component of the propagation matrix  $\mathbf{F}$  would then become the percentage of the electron's energy that it retains. The multiple scattering covariance matrices of lower planes would then be calculated based on this reduced energy. Unfortunately, the distribution of energy losses is asymmetric. A proper treatment of energy loss [184] requires this distribution to be taken into account in the track fitting.

**Try to get energy estimates from tracks.** If the Gaussian transformations described above could be found, then the tails of the multiple scattering distribution would no longer undermine our efforts to estimate the energy of the track from the track itself. An iterative approach could then estimate the most likely energy, refit the tracks, and re-estimate the energy until it converged. Then the energy splitting information could be used to make better estimates of the incident  $\gamma$ -ray direction.

**Fit shower profiles in the calorimeter.** Fitting the shower development profile in the calorimeter may lead to much better energy estimates. Such fits allow leakage to be accurately estimated. The *GLAST* collaboration calorimeter team is implementing shower profile fits [57].

**Measure individual electron energies in the calorimeter.** A finely segmented calorimeter would enable the separation of the energy deposition from the individual electrons. An accurate measure of the individual electron energies would increase the silicon tracker resolution by allowing better energy weighting of the electron track directions to find the incident  $\gamma$ -ray direction. However, finer sampling of the calorimeter requires more electronics and thus more power, as well as more gaps between CsI blocks. Sampling granularity small enough to resolve individual electron energies may not be feasible for *GLAST*.

**Use better energy splitting probabilities.** Heitler [68, 140] has calculated the probability distributions of the energy split between the electrons as a function of the total incident energy. While it may not be possible to get good energy splitting estimates directly from the tracks, it is often possible to determine which track is more energetic. The most likely energy split according to Heitler could be assumed, with the appropriate track receiving more energy.

The relative probability of various energy splittings as a function of total  $\gamma$ -ray energy can be found from the total pair-production cross-section. In the limit of an unscreened point nucleus, extreme-relativistic energies, and negligible nuclear recoil, in the first Born approximation, the cross-section as a function of energy splitting is [140]

$$\frac{d\sigma}{df} = 4\alpha Z^2 r_0^2 \left( \frac{4}{3}f^2 - \frac{4}{3}f + 1 \right) \ln [2fE(1-f)] \quad (8.38)$$

where  $f$  is the fraction of energy in one electron,  $E$  is the total  $\gamma$ -ray energy in MeV,  $Z$  is the atomic number of the target nucleus (Si or Pb), and  $r_0$  is the classical electron radius,  $2.82 \times 10^{-13}$  cm. This function is plotted as relative probability versus energy split for a variety of total  $\gamma$ -ray energies in Figure 8.6. For the lowest energies, the probabilities appear to be negative for extreme values of the energy split; this is an indication that the assumptions noted above have broken down.

## 8.9 Calculating the Point-Spread Function

The point-spread function of the beam test instrument could be estimated by the distribution of reconstructed  $\gamma$ -ray incident angles. *GLAST* may be calibrated in the same way either in a beam, or in space with a sufficiently bright  $\gamma$ -ray point source. However, the Kalman filter offers us an opportunity to calculate the theoretical point-spread function under our Gaussian assumptions. The variance in the estimate of the incident direction of each electron is given by the (2,2) component of the covariance matrix  $\mathbf{C}$ . To calculate the point-spread function, we should look at the smoothed estimate of  $\mathbf{C}$  in the top layer. We simply read off the variance of the estimate of

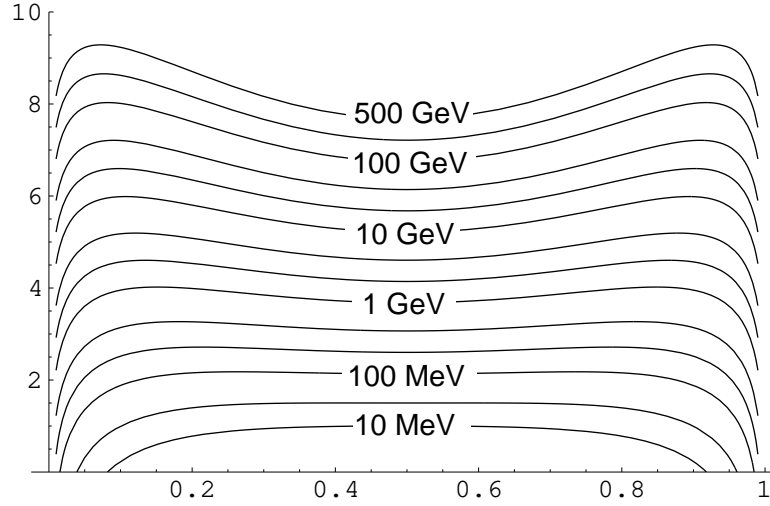


Figure 8.6: Probability distributions of  $e^-e^+$  energy split as a function of total incident energy. The vertical scale is arbitrary; each curve is normalized. The vertical offset is for clarity. Labels indicate total incident  $\gamma$ -ray energy. At the highest energies, asymmetric energy splittings are relatively more likely; for most energies of interest to *GLAST*, the probability of all splittings except the most extreme ones is approximately equal.

the electron track direction. To find the error in our estimate of the incident  $\gamma$ -ray direction, we need to combine our estimates of the two electron tracks. If  $E_1$  is the energy of one electron and  $E_2$  is the energy of the other, our estimate of the incident  $\gamma$ -ray direction is

$$\theta_\gamma = \frac{E_1\theta_1 + E_2\theta_2}{E_1 + E_2} \quad (8.39)$$

Then the variance in  $\theta_\gamma$  must be

$$\sigma_{\theta_\gamma}^2 = \frac{E_1^2\sigma_{\theta_1}^2 + E_2^2\sigma_{\theta_2}^2}{(E_1 + E_2)^2} \quad (8.40)$$

The variance in our estimate of the incident  $\gamma$ -ray direction depends on the variances of the two electron track directions, and on the energy split between the electrons. We can calculate the variances of the two electron tracks from the Kalman filtering equations. Since our estimates of  $\mathbf{C}$  do not depend on the data, we can compute the variances ahead of time. The variances will depend on the electron energy (through



$\mathbf{Q}_k$ , the multiple scattering covariance matrix given by equation (8.37)), the amount of radiator on each plane (also through  $\mathbf{Q}_k$ ), the ratio of the strip pitch to the gap between planes (through the measurement error  $\mathbf{V}$  and the propagation matrix  $\mathbf{F}$ ), and the number of planes with measurements. Thus the variance depends on four variables, making it difficult to display in a single plot. Given probability distributions for some of these variables, we may marginalize some or all of them in a Bayesian way (§2.6.3), leaving us with a representative “average” point-spread width. Table 9.2 shows the calculated width of the point-spread function for several interesting configurations of the full *GLAST* instrument.

It should be noted that all of these calculated point-spread widths assume that every quantity is normally distributed. In particular, they ignore the large tails on the multiple scattering distribution, and they combine the estimates and variances of the two electron directions as if they were Gaussian distributed. They ignore the effects of electrons leaving the tracker, which will shorten the average track length. As such, they are useful for estimating instrument performance, but would not be suitable for likelihood analysis of *GLAST* data.

## 8.10 Extended Kalman Filters

In §8.3.4 we linearized the propagation matrix  $\mathbf{F}$ . That is, we chose to use the track slope in our state vector, and assumed that the additional slope from multiple scattering would be normally distributed, and would add to the previous slope value. Of course, the multiple scattering *angle* is (roughly) normally distributed, and the additional scattering angle should be added to the previous track angle. For small angles ( $< 30^\circ$ ), this is a reasonable approximation. Since all the beam test  $\gamma$ -rays were incident from the same direction ( $0^\circ$ ), this approximation was valid. However, for *GLAST*, the  $\gamma$ -rays will be incident from every direction, and a small-angle approximation will not be valid. There has been extensive work done [89, 90] to extend Kalman filters to non-linear propagators. This would allow the electron track angle to be kept in the state vector. A detailed discussion of such methods is beyond the scope of this work.

# Chapter 9

## Instrument Response

Once the various parts of the beam test instrument had been built, and the software to analyze the data had been written, the instrument was placed in the beam line in End Station A. The data taken at SLAC during October 1997 yielded important insights into issues of backslash self-veto in the ACD as well as the establishment of the feasibility of pointing resolution using the calorimeter only [169]. In this chapter, we will focus on the silicon tracker: the specific adaptations necessary to analyze tracker data and the instrument parameters measured.

### 9.1 Alignment

To avoid systematic errors in reconstructed particle direction, corrections were made to account for possible misalignment of the planes. Machining errors on the scale of the strip pitch ( $236\text{ }\mu\text{m}$ ) would make it appear that a track had scattered more (or less) than it actually had. Smaller errors would influence track reconstruction in a statistically similar way. In part to ameliorate this effect, data was taken with the Cu radiating foil removed, so that beam electrons were directly incident on the detector. For 25 GeV beam electrons, multiple scattering is negligible. These tracks could thus be used to “align” the planes by finding the relative offset of each plane. The offsets were used to correct the positions of the hits in software.

The straight electron tracks were fit with a line in each projection. In each plane,

the median value of the fit residual was taken as the plane offset. All strip positions in the plane were corrected, and the process iterated until the median residuals converged to zero. Because the strip measurements were quantized, the linear fits were subject to severe aliasing on the scale of the strip pitch. To alleviate the effects of this aliasing, a small amount of random noise was added to each strip position independently for each fit.

The tracker was found to be nearly aligned as constructed. The largest offset was  $\sim 250 \mu\text{m}$ . The alignment procedure measured the strip positions to an accuracy of  $\sim 50 \mu\text{m}$ .

## 9.2 Cuts

The SLAC main electron beam runs nominally at 120 Hz. The state of the beam test instrument, including all strips hit, all energy deposited in the calorimeter, and all ACD tiles hit were read out for each beam spill. With an average of one electron per pulse, approximately 30% of spills had no electrons in them at all. Spills with one or more electrons shed bremsstrahlung photons with a probability dependent on the thickness of the Cu radiator foil (3.5%  $X_0$ , 5%  $X_0$ , or 10%  $X_0$ ). Therefore only a fraction of the  $2.1 \times 10^8$  triggers recorded on tape were useful. A filtering program (not to be confused with Kalman filtering) was developed to extract the useful triggers. The criteria for accepting a trigger as a useful event were the detection of hits in three successive tracker planes, or of more than 6 MeV for low gain or 160 MeV for high gain in the calorimeter. These criteria were adopted so as to be sure to accept any particle that passed through the tracker (whether or not it hit the calorimeter) as well as any event that did not interact with the tracker, such as a  $\gamma$ -ray that did not convert until it entered the calorimeter. The three-in-a-row requirement for the tracker was designed to ensure that random noise hits in the tracker would not pass the acceptance criteria. When the Cu foils were in place to produce  $\gamma$ -rays from the main electron beam, approximately 20% of the triggers were accepted. When the foil was removed, and the electron beam was directly incident on the instrument, nearly all the triggers were retained.

These “useful events” were then analyzed by the reconstruction software. Many of them had no interactions in the calorimeter and were thus thrown away. In addition, any event with one or fewer hits in either projection was thrown away. The remaining events were reconstructed, but not all of these were satisfactory to be included in the analysis. The first requirement was that the hodoscopic calorimeter reported only one electron in the spill. The presence of multiple beam electrons in the spill greatly increases the chance of multiple bremsstrahlung  $\gamma$ -rays entering the tracker at the same time. Second, each anti-coincidence tile was required to have less than  $1/4$  MIP (minimum ionizing particle; see [5] for details) of energy deposited. While the ACD is designed to detect charged particles, it represents  $1\% X_0$  of material, which can cause  $\gamma$ -rays to pair convert. If a  $\gamma$ -ray pair converts in an ACD tile, each electron will deposit 1 MIP, times the fraction of the tile through which the electron passes. For example, if the  $\gamma$ -ray converted halfway through the tile, then the two electrons would deposit  $2 \times (1/2 \times 1\text{MIP}) = 1$  MIP. The  $1/4$  MIP threshold will therefore reject all events where a  $\gamma$ -ray converts in the top  $7/8$  of the thickness of the tile. Of course, there are two layers of scintillator on the top of the instrument, so any conversions in the first layer will deposit 2 MIP in the second layer. Thus this cut eliminates  $15/16$ ths of the events which convert in the ACD, as well as any charged particle events.

In addition, cuts were made based on the characteristics of the tracks themselves. All tracks were required to have at least three real hits, exclusive of “virtual” hits placed on noisy strips or outside of the tracker. The total track  $\chi^2$  was divided by the number of hits in the track, and this reduced  $\chi^2$  was required to be less than 5. The final cut demanded that all tracks start at least 4.7 mm (20 strips) from the edge of the active area of the tracker. Electrons from  $\gamma$ -rays that convert that close to the edge are likely to exit the tracker preferentially, and will introduce a bias to the distribution of reconstructed  $\gamma$ -ray directions. The efficiency of each cut is given in Table 9.1.

**Monte Carlo cuts.** In an effort to make the beam test data as directly comparable with Monte Carlo simulations as possible, the Monte Carlo data was subjected to very

Cut	Triggers Kept
Hodoscope	42-55 %
ACD	57-84 %
Three Hits	77-87 %
$\chi^2$	73-82 %
Edge	89-96 %
All Cuts	15-25 %

Table 9.1: Cut efficiencies

similar cuts. The Monte Carlo included an anti-coincidence system, and a similar cut was made to reject events which converted in the plastic scintillator. All of the cuts based on track parameters were made in the exact same way for both the Monte Carlo and the beam test data. Since most of the Monte Carlo simulations were done with incident  $\gamma$ -rays drawn from a bremsstrahlung energy spectrum, there was no need to make cuts to ensure only one  $\gamma$ -ray in the tracker.

The particular cuts made were chosen to simplify analysis of the beam test data. They are not meant to represent the types of cuts that will be made on for *GLAST*. *GLAST* will be faced with a very different environment in space, replete with background particles, albedo  $\gamma$ -rays, and signal  $\gamma$ -rays incident from all directions. It also has a very different geometry, which will require combining data from different towers and accounting for gaps and support structure. The relevant feature of the cuts made here are that they are very nearly identical for the beam test instrument and the Monte Carlo simulations. This will allow direct comparison of their results. However, the instrumental parameters measured for the beam test instrument will not be directly scalable to *GLAST*.

### 9.3 Expected Beam Test Point-Spread Widths

. Once the various cuts have been applied to the data sets, distributions of the reconstructed angle can be compared. Before we compare these results, it may be useful to consider the theoretical widths we expect to find, based on the Kalman filter covariances. In §8.9 we saw that we could calculate the expected point-spread width

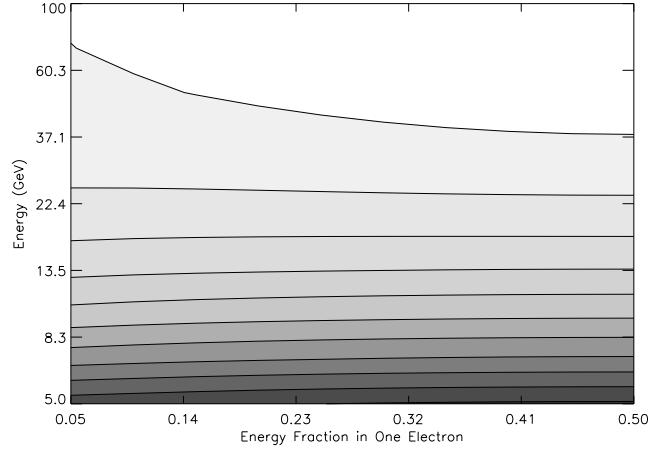


Figure 9.1: Point-spread width dependence on total energy and energy splitting fraction. Darker shades indicate larger point-spread width. At lower energies, the width is nearly constant as a function of the splitting fraction. At high energies, the point-spread function is much larger for asymmetric splittings. The beam test was always in the low-energy limit for this purpose.

of a given instrument configuration independent of the actual measured data, under the assumption that all distributions involved are Gaussian. In order to estimate the point-spread widths we will measure with the beam test instrument, we must properly average the point-spread width over all the different classes of events we expect to measure. Recall that the point-spread width  $\sigma(E, f, p, d, x, N)$  is a function of the  $\gamma$ -ray energy  $E$ , the fraction  $f$  of that energy in one electron, the silicon strip pitch  $p$ , the gap  $d$  between adjacent planes, the total amount  $x$  of material in the radiator and the detector in each plane, and the number  $N$  of planes which measure the given event. For any instrument configuration, strip pitch  $p$ , gap  $d$  and radiator  $x$  are fixed.

To facilitate comparison, we will look at events with approximately equal energies. Therefore we must average over a range of electron energy splittings and numbers of planes traversed. The point-spread width is an almost constant function of  $f$  below 5 GeV. Above 5 GeV, the point-spread width is significantly smaller for even energy split (Figure 9.1), although such a splitting is comparatively less common\* (Figure 8.6). Therefore, we will assume that the point-spread width is approximately

---

\*The energy splitting is assumed here to be symmetric, as described by the Bethe-Heitler formula

independent of the energy splitting fraction  $f$ . The number of planes  $N$  through which the  $e^-e^+$  pair travel depends on the total number of planes in the instrument (6) and in which plane the  $\gamma$ -ray converted. The probability that a  $\gamma$ -ray will convert in a given layer is given by equation (8.3) with  $t/X_o$  equal to the thickness of the SSD plus the Pb radiator for the plane in question. The intensity of the  $\gamma$ -ray beam at that plane is given by equation (8.2), with  $t/X_o$  equal to the total number of radiation lengths of material above the plane in question. This represents the beam attenuation from the planes above. Therefore, the probability of a conversion in plane  $n$  is

$$P(n) = I_o e^{(-7/9(n-1)x)} (1 - e^{7/9x}) \quad (9.1)$$

where  $x$  is the total radiator in each plane. To calculate the average point-spread width, we wish to weight the point-spread width for each number of planes by the probability that the conversion happened in that plane. Recalling that we accept only events with at least three hits, we find the probability that a  $\gamma$ -ray converted in one of the top four planes:

$$P(n \leq 4) = \sum_{n=1}^4 P(n) \quad (9.2)$$

Therefore, the probability that any given pair-production event converted in plane  $n$  is

$$P(n|1 \leq n \leq 4) = P(n)/P(n \leq 4) \quad (9.3)$$

Plugging in, we arrive at the weights we will apply to the variances measured on each plane.

$$P(n) = \frac{e^{-\frac{7}{9}(n-1)x}}{\sum_{n=1}^4 \exp\left(-\frac{7}{9}(n-1)x\right)} \quad (9.4)$$

It remains only to examine the point-spread width  $\sigma$  as a function of total  $\gamma$ -ray energy  $E$  for each instrument configuration. The nature of the Kalman equations (§8.3) makes the calculation of the point-spread width tedious. However, it is a simple matter to compute electronically [82].

---

[68]. Below about 3.3 MeV, asymmetries arise because the nucleus attracts  $e^-$  while repelling  $e^+$ . The asymmetric differential cross sections have been worked out by Øverbø, Mork, and Olsen [154].

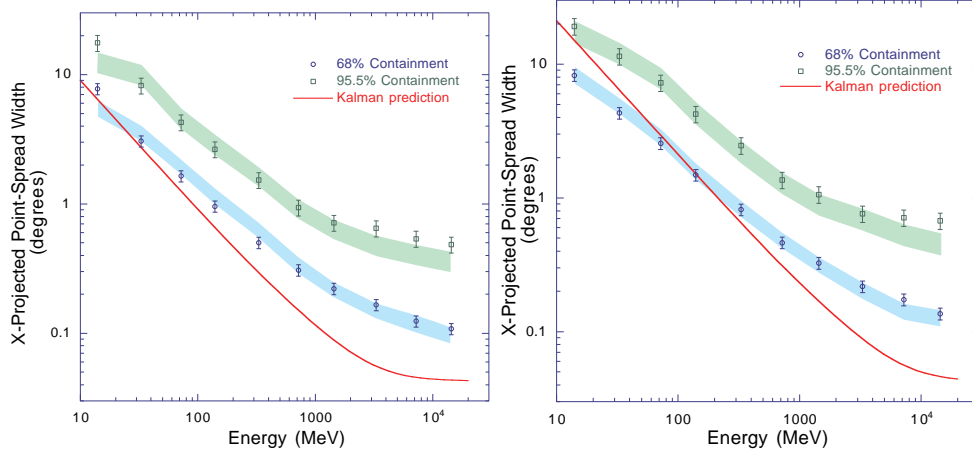


Figure 9.2:  $x$ -projected point-spread widths for Pancake configuration with no Pb radiators (left) and 4% Pb radiators (right). Circles indicate the 68% containment width, and squares indicate the 95.5% containment width. Error bars are  $2\sigma$  statistical errors, and shaded regions represent the  $2\sigma$  confidence regions of the Monte Carlo estimates. The line is an estimate of the point-spread width from the Kalman filter.

## 9.4 Conclusions

While our theoretical calculations make some simplifying assumptions which may not be entirely accurate, we hope that the Monte Carlo simulations will more completely represent the actual data. For example, the `gismo` code has a sophisticated multiple scattering model which is much more accurate than the simplistic Gaussian assumption made above. Furthermore, the Monte Carlo simulations included all the particular geometric elements of the beam test instrument.

### 9.4.1 Comparison of Beam Test and Monte Carlo Results

The measured point-spread widths for both the Monte Carlo simulations and the beam test data are shown for each instrument configuration in Figures 9.2 and 9.3. There is good agreement between the two out to the 95% containment radius. Two example distributions are shown in Figure 9.4.

Three features of the Kalman filter estimate are relevant. First of all, in general the Kalman estimate is lower than the measured widths. Second, the slope of the



Kalman estimate with energy is steeper. Finally, the Kalman estimate reaches an asymptotic limit faster, and the limit is significantly lower.

The Kalman estimates are lower than the measured widths in general because the Kalman estimates are based on Gaussian errors. Furthermore, the point-spread widths estimated by the Kalman filter are the standard deviations; that is, they correspond to the 68% containment radius of the point-spread function assuming it is Gaussian. As we have noted, the multiple scattering distributions have significant tails, and the measurement error distributions are more square than Gaussian. These effects tend to degrade the fit quality, leading to larger point-spread widths.

The slope of the Kalman estimate is very nearly  $1/E$  at low energies; this is expected since it is based on a Gaussian multiple scattering model with the width inversely proportional to the energy. On the other hand, the actual beam test instrument is very narrow. At low energies, this leads to a strong self-collimation effect.  $\gamma$ -Rays whose electrons initially make large scatters would be reconstructed in a wide instrument with large apparent incident angles. These events cannot be reconstructed with the limited data from the narrow instrument, and are thrown away. As we expect, stretch configuration displays more self-collimation than pancake, and high-radiator configurations (with larger scattering) also display more self-collimation.

At high energies, the width of the point-spread function is dominated by the measurement error. The assumptions made for the Kalman filter are not particularly good in this regime. The Kalman filter assumes that the position measurement is continuous, with Gaussian errors. In fact, the measurement is a discrete one, with roughly square errors. The effects of the square error distribution have been discussed in §8.5. The effects of the discrete measurement are more difficult to assess. Since the tracker planes were very nearly aligned, and the  $\gamma$ -ray beam was very nearly aligned with the strip grid, the measured distributions are subject to aliasing. If the planes are perfectly aligned, then the minimum non-zero half-angle which can be measured by the instrument in pancake mode is  $1/2 \times 236 \mu\text{m}/150.0 \text{ mm} \approx 0^\circ 05$ . That assumes that the  $\gamma$ -ray converts in the middle of a strip, and that the electron continues down the instrument, hitting the same strip in each plane until the last one, by which time it has drifted half the strip pitch and activates the next strip. In fact, we see in

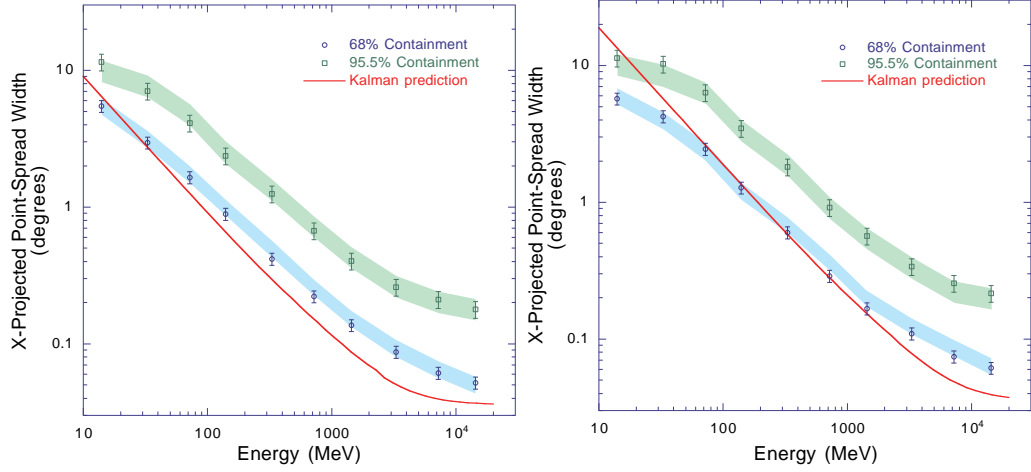


Figure 9.3:  $x$ -projected point-spread widths for Stretch configuration with no Pb radiators (left) and 4% Pb radiators (right). Circles indicate the 68% containment width, and squares indicate the 95.5% containment width. Error bars are  $2\sigma$  statistical errors, and shaded regions represent the  $2\sigma$  confidence regions of the Monte Carlo estimates. The line is an estimate of the point-spread width from the Kalman filter.

Figure 9.2 that the Kalman estimate is well below 0.05 above 5 GeV. Since the point-spread function for the beam test instrument and for the Monte Carlo simulations is quantized at that level, it is not surprising to find that its width is somewhat larger.

These aliasing effects will actually be helped by the slight offsets in the instrument planes acquired during the launch of *GLAST*, assuming that they can be well measured using cosmic rays. In addition, the additional planes will act to reduce the aliasing. Perhaps more importantly, *GLAST* will be illuminated from a large fraction of the sky. In scanning mode, the bearing to a source in instrument coordinates will be constantly changing, serving to smear the aliasing over all scales. These effects should push the performance of *GLAST* closer to the Kalman estimate. In any case, since the Monte Carlo correctly models the aliasing, simulations of *GLAST* from physically reasonable sources will make accurate predictions of the *GLAST* point-spread width.

A final difference between the instrument as tested and simulated and the idealized Kalman assumptions concerns the geometry of the detectors. The Kalman estimate assumes that the multiple scattering occurs in the same place as the measurement, when in fact most of the multiple scattering occurs in the Pb radiators, which are a few

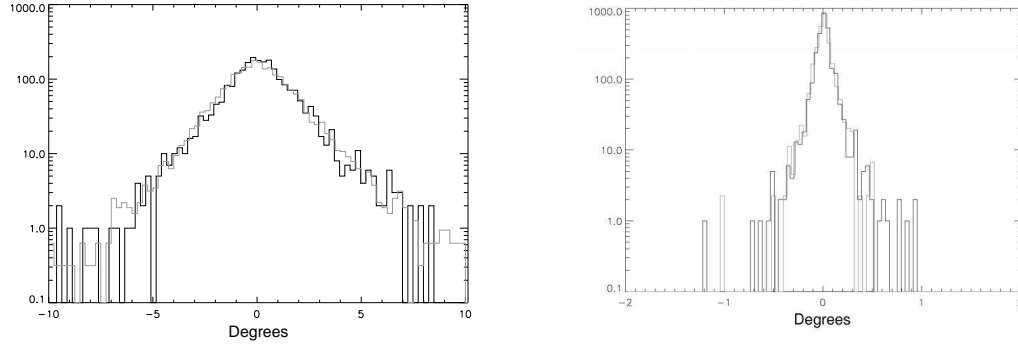


Figure 9.4: Full distributions of the reconstructed projected incident  $\gamma$ -ray angle. Left side is pancake configuration, 4% Pb radiators, 100–200 MeV. Right side is stretch configuration, no Pb radiators, 5–10 GeV. Vertical scale is renormalized for comparison of distributions.

millimeters away from the detectors. Simulations of the baseline *GLAST* instrument suggest that as a rule of thumb, the point-spread width is degraded by 3.5% per millimeter of separation between the radiator and detector [15]. The separation in the beamtest instrument was about 2 mm, which would suggest a degradation of about 7% from the theoretical Kalman estimate.

### 9.4.2 Implications for *GLAST*

The agreement between the Monte Carlo simulations and the beam test data is clearly encouraging to the *GLAST* collaboration. The Kalman filtering formalism appears to succeed admirably at reconstructing electron tracks. Kalman estimates of the *GLAST* point-spread width for various configurations are given in Table 9.2.

The equivalent Kalman estimates of the beamtest instrument point-spread width proved to be a reasonable estimate of the instrument performance. However, some care must be taken to interpret these results in light of their implications for *GLAST*. Primarily, it is important to remember that the point-spread widths measured by the beamtest may not be used as an estimate of the *GLAST* point-spread width; they are two separate instruments with different characteristics. Furthermore, the beam test instrument was measured in a controlled, low background beam environment,

Strip pitch ( $\mu\text{m}$ )	Radiator	100 MeV PSF	1 GeV PSF	10 GeV PSF
180	0.0%	0.91	0.11	0.023
180	3.5%	2.0	0.22	0.035
180	5.0%	2.3	0.25	0.038
240	0.0%	0.91	0.12	0.029
240	3.5%	2.0	0.22	0.040
240	5.0%	2.3	0.26	0.043
400	0.0%	0.93	0.13	0.044
400	3.5%	2.0	.24	0.051
400	5.0%	2.3	0.27	0.054

Table 9.2:  $1\sigma$  widths of the point-spread function as calculated from the Kalman formalism, for different silicon strip pitches and amounts lead radiator (given in radiation lengths), assuming 16 planes space 30.0 mm apart. The method used to generate these results is given in §8.9.

while *GLAST* will be operating in space, bombarded by charged particles and albedo  $\gamma$ -rays.

However, this does not mean that these results are irrelevant to *GLAST*. The verification of the Monte Carlo code implies that simulations of *GLAST* with **glastsim** should yield accurate estimates about the final instrument parameters without building many expensive prototypes. Promises made by **glastsim** may be reasonably expected to be fulfilled by *GLAST*.

# Appendix A

## SSB Arrival Time Corrections

There are four components to the corrections to Solar System Barycenter (SSB) Time from UTC time in equation (4.6) [43, 112]. The first is due entirely to timekeeping convention, and translates UTC to a monotonic sequentially indexed time known as International Atomic Time:

$$\Delta_{\text{convention}} = k + 32184 \quad (\text{A.1})$$

where  $k$  is the integral number of leap seconds since 1972.

The second correction is made for the position of the observatory. Since the pulsar is much further away from the barycenter than the observatory is, the difference in path lengths is simple. Dividing by the speed of light, we arrive at the correction to the arrival time:

$$\Delta_{\text{location}} = \frac{\hat{\mathbf{n}} \cdot \mathbf{r}_{bo}}{c} \quad (\text{A.2})$$

where  $\hat{\mathbf{n}}$  is a unit vector pointing at the pulsar, and  $\mathbf{r}_{bo}$  is the vector between the SSB and the observatory. In practice, this is the vector sum of the vector from the SSB to the center of the Sun, the vector from the Sun to the Earth, and the vector from the Earth to *CGRO*. The position vectors for the Earth and Sun are taken from the standard ephemeris published by the Jet Propulsion Laboratory [185].

The remaining two corrections are relativistic in nature. The first is the Einstein delay  $\Delta_{\text{Einstein}}$ . This is the manifestation of the old adage that “heavy clocks run

slowly.” It depends only on the depth of the potential well in which the observatory sits, not the path that a  $\gamma$ -ray takes to arrive there. Therefore, the Einstein delay is included in the JPL ephemeris. There is an additional term that results from the ellipticity of the Earth’s orbit of the form  $\mathbf{v}_\oplus \cdot \mathbf{r}_{bo}/c^2$ . The portion of this term due to the Earth’s position is already included in International Atomic Time; we need only to add the part due to the satellite position:

$$\Delta_{\text{Einstein}} = \Delta_{\text{Einstein}} (\text{JPL}) + \frac{\mathbf{v}_\oplus \cdot \mathbf{r}_{\oplus o}}{c^2} \quad (\text{A.3})$$

The last correction is the Shapiro delay  $\Delta_{\text{Shapiro}}$ . This results from the delay induced by the gravitational potential in the region of the Sun [180] and goes as

$$\Delta_{\text{Shapiro}} \simeq \frac{2GM_\odot}{c^3} \ln(1 + \cos \theta) \quad (\text{A.4})$$

where  $\theta$  is the angle between the vector from *CGRO* to the Sun and the vector from *CGRO* to the pulsar.

Combining all these corrections, the arrival time in the SSB frame as a function of the measured UTC time is given by:

$$\begin{aligned} t_b = & t_{\text{UTC}} + k + 32.184 + (1/c)\hat{n} \cdot \mathbf{r}_O + \\ & \Delta_{\text{Einstein}} + (1/c^2)\mathbf{v}_\oplus \cdot \mathbf{r}_{\oplus o} + \\ & (2GM_\odot/c^3) \ln(1 + \cos \theta) \end{aligned} \quad (\text{A.5})$$

The code to make these adjustments to *EGRET* arrival times was written by Joe Fierro [42], based on calculations and data found in [19, 72, 180, 185, 187] and [188].

# Appendix B

## Summary of Kalman Filtering Equations

Define the first state vector  $\mathbf{x}_0$  and covariance  $\mathbf{C}_0$

For each plane  $k$  in the instrument:

Project from the last plane:

$$\begin{aligned}\mathbf{x}_{k,proj} &= \mathbf{F}_{k-1}\mathbf{x}_{k-1} \\ \mathbf{C}_{k,proj} &= \mathbf{F}_{k-1}\mathbf{C}_{k-1}\mathbf{F}_{k-1}^T + \mathbf{Q}_{k-1}\end{aligned}$$

Filter the estimates:

$$\begin{aligned}\mathbf{C}_k &= \left[ (\mathbf{C}_{k,proj})^{-1} + \mathbf{H}_k^T \mathbf{G}_k \mathbf{H}_k \right]^{-1} \\ \mathbf{x}_k &= \mathbf{C}_k \left[ (\mathbf{C}_{k,proj})^{-1} \mathbf{x}_{k,proj} + \mathbf{H}_k^T \mathbf{G}_k \mathbf{m}_k \right]\end{aligned}$$

Starting at the second-to-last plane and working back up:

Smooth the estimates:

$$\begin{aligned}\mathbf{A}_k &= \mathbf{C}_k \mathbf{F}_k^T (\mathbf{C}_{k+1,proj})^{-1} \\ \mathbf{x}_{k,smooth} &= \mathbf{x}_k + \mathbf{A}_k (\mathbf{x}_{k+1,smooth} - \mathbf{x}_{k+1,proj}) \\ \mathbf{C}_{k,smooth} &= \mathbf{C}_k + \mathbf{A}_k (\mathbf{C}_{k+1,smooth} - \mathbf{C}_{k+1,proj}) \mathbf{A}_k^T \\ \mathbf{r}_{k,smooth} &= \mathbf{m}_{k,smooth} - \mathbf{H}_k \mathbf{x}_{k,smooth} \\ \mathbf{R}_{k,smooth} &= \mathbf{V}_k - \mathbf{H}_k \mathbf{C}_{k,smooth} \mathbf{H}_k^T \\ \chi_+^2 &= \mathbf{r}_{k,smooth}^T \mathbf{R}_{k,smooth}^{-1} \mathbf{r}_{k,smooth}\end{aligned}$$

# Appendix C

## Track Finding Algorithm

While the Kalman filter offers a way to quickly and automatically find the best fit electron track to a given set of detector hits, identifying which hits belong to the track is not a science, but an art. We have experimented with a number of algorithms, and have empirically fine-tuned this one. This is the algorithm used by `tjrecon` for finding tracks.

- Load the data from one event into the data structures.
- For each projection:
  1. Create a new track:
    - Initialize all the matrices and arrays
    - Assign first hit to be leftmost hit in first layer with hits
    - Assign second hit to be leftmost hit in second layer with hits.
    - If there are  $\leq 1$  hits in this projection, go to next projection
    - Assign initial slope to first hit
    - Assign half the calorimeter energy to the track
    - Assign the multiple scattering matrix for that energy as the Covariance matrix.
  2. Create a second track, using leftmost hit in first layer with hits, rightmost hit in second layer. If there are no hits in the second layer, continue down until you find a layer with hits.
  3. Find the hit for each layer of the first track:
    - Project state vector and C matrix to next layer



- Assign the hit for that layer:
    - \* If the track projects out of the tracker, add a virtual hit outside the tracker, and assign that hit to the track.
    - \* If there is a dead strip within  $\pm 10$  strips, add a virtual hit on the dead strip. Don't assign it yet.
    - \* Find the hit closest to the projected track
    - \* If there is only one hit on that layer, assign it to the track.
    - \* If the closest hit already belongs to another track, take the next closest hit. Assign it to the track.
    - \* If the closest hit is unclaimed, assign it to the track.
  - Revise (“filter”) the projection of the state vector and C matrix in light of this measurement.
4. Smooth the first track: Starting at the bottom, apply the Kalman smoothing equations to the state vectors and C matrices
  5. Find the hit for each layer of the second track.
  6. Smooth the second track.
  7. Untangle the tracks by swapping hits from one track to the other so they do not cross.
  8. Check free hits for first track:
    - For each level, starting at the top, for each unclaimed hit, swap the track's current hit with the unclaimed hit.
    - Filter the track. (giving a new set of predicted locations at each level below the current one)
    - For each successive level, check to see if the new predictions suggest different hits in the track. If so, and if they are real hits (not virtual ones), assign them to the track. Filter. Continue to the bottom of the tracker.
    - Smooth the new track.
    - Compare the  $\chi^2$  of this new track with the original. If it's lower, keep the new track. Otherwise revert to the old track.
    - Start the whole game over from scratch on the next level down.
  9. If the track changed at all in the above step, check free hits again, this time starting at the bottom.
  10. Check free hits for the second track, starting at the top.
  11. If the second track changed, check free hits again, this time starting at the bottom.

12. Starting at the bottom, check to see if swapping hits helps:
    - For each level, swap the hits between the two tracks. Filter and smooth both tracks.
    - If the new  $\chi^2$  is smaller, keep the new tracks. Otherwise revert.
  13. Make sure tracks don't cross between first and second planes. If the two tracks do not share their first hit, it is likely that the tracks don't really cross. Filter and smooth both tracks.
  14. Check to see if one of the tracks may have left the tracker: (If so, the two tracks may currently share hits on all layers below the exit point)
    - Find the lowest level on which the tracks share hits. If they don't share any, then quit.
    - If the first shared hit is at least the third hit in the track, create a virtual hit outside the tracker in the direction of the current track. Assign it to the track.
    - Remove all successive hits from the track.
    - Filter and smooth.
    - Check free hits again, to see if, in this new configuration, the track would prefer different hits upstream.
    - If the  $\chi^2$  is smaller, keep the new tracks. Otherwise revert.
  15. Repeat all for the other projection.
- If we don't have four good tracks, then throw the event away.
  - If at least one of the four tracks leaves the tracker:
    - Find the track that leaves the tracker earliest.
    - Find the track in the other projection with the larger  $\chi^2$ . We will claim that this track is the other projection of the track that leaves.
    - Remove all hits from that track below the exit point of its opposite-projected track.
  - For each projection:
    - Vary the energy split between the two tracks.
    - Filter and smooth with the new energy split.
    - Find the split fraction that minimizes  $\chi^2$ .
    - In practice, this always assigns all the energy to one track. Assign 75% of the energy to that track, 25% to the other.
  - Write tuple containing relevant information.

# Bibliography

- [1] Anthony, P. L. and Szalata, Z. M., *Flexible high performance VME based data acquisition system for the ESA physics program*, SLAC-PUB-7201, 1996.
- [2] Atwood, W. B., *Gamma-Large Area Silicon Telescope (GLAST) Applying Silicon Detector Technology to the Detection of Gamma-Rays in Space*, Nuclear Instruments and Methods in Physics Research, **342**, 1, 302–307, Mar 1994.
- [3] Atwood, W. B., Burnett, T., Cailliau, R., Myers, D. R., and Storr, K. M., *GISMO: An Object Oriented Program for High Energy Physics Simulation and Reconstruction*, International Journal of Modern Physics, **C3**, 459, 1992.
- [4] Babul, A., Paczyński, B., and Spergel, D., *Gamma-Ray Bursts from Superconducting Cosmic Strings at Large Redshifts*, Astrophysical Journal Letters, **316**, L49–L54, May 1987.
- [5] Barnett, R. M. *et al.*, *Review of Particle Properties*, Physical Review D, **54**, 1, 1996.
- [6] Bednarz, J. and Ostrowski, M., *Energy Spectra of Cosmic Rays Accelerated at Ultrarelativistic Shock Waves*, Physical Review Letters, **80**, 18, 3911, May 1998.
- [7] Bendat, J. S. and Piersol, A. G., *Random Data: Analysis and Measurement Procedures* (New York: Wiley), 2nd ed., 1986.
- [8] Bennett, K. *et al.*, *COS B Observations of Pulsed  $\gamma$ -ray Emission from PSR 0531+21 and PSR 0833–45*, Astronomy and Astrophysics, **61**, 279, 1977.
- [9] Beran, R. J., *Annals of Mathematical Statistics*, **40**, 1196, 1969.
- [10] Bertsch, D. L., Dame, T. M., Fichtel, C. E., Hunter, S. D., Sreekumar, P., Stacy, J. G., and Thaddeus, P., *Diffuse Gamma-Ray Emission in the Galactic Plane from Cosmic-Ray, Matter, and Photon Interactions*, Astrophysical Journal, **461**, 2, 587–600, Oct 1993.

- [11] Bertsch, D. L. *et al.*, *Pulsed High-energy Gamma-radiation from Geminga (1E0630+178)*, *Nature*, **357**, 306–307, May 1992.
- [12] Bignami, G. F., *The COS B Experiment for  $\gamma$ -ray Astronomy*, *Space Science Instruments*, **1**, 245, 1975.
- [13] Bignami, G. F. and Caraveo, P. A., *Geminga: new period, old  $\gamma$ -rays*, *Nature*, **357**, 287, 1992.
- [14] Bloom, E. D., *GLAST*, *Space Science Reviews*, **75**, 1–2, 109–125, Jan 1996.
- [15] Bloom, E. D., Godfrey, G., and Ritz, S. (editors), *Proposal for the Gamma-ray Large Area Space Telescope*, Feb 1998. SLAC-R-522.
- [16] Boer, M., Roberts, B. A., Malina, R., Feroci, M., Piro, L., and Hurley, K., IAU Circular 6795, Dec 1997.
- [17] Bond, H. E., IAU Circular 6654, May 1997.
- [18] Böttcher, M. and Dermer, C. D., *High-Energy Gamma Rays from Ultra-High-Energy Cosmic-Ray Protons in Gamma-Ray Bursts*, *Astrophysical Journal Letters*, **499**, L131–L134, Jun 1998.
- [19] Brumberg, V. A. and Kopejkin, S. M., *Relativistic Theory of Celestial Reference Frames*, in J. Kovalevsky, I. I. Mueller, and B. Kolaczek (editors), *Reference Frames in Astronomy and Geophysics*, p. 115 (Dordrecht: Kluwer Academic Publishers), 1989.
- [20] Buccheri, R., Maccarone, M. C., Mattox, J. R., Thompson, D. J., Kanbach, G., Camerini, U., and Fry, W. F., *A Search for High Energy Gamma-Ray Bursts in the EGRET Data Utilizing Space-Time Correlation*, in G. J. Fishman, J. J. Brainerd, and K. Hurley (editors), *Gamma-Ray Bursts: Second Workshop*, vol. 307 of *AIP Conference Proceedings*, pp. 377–381 (New York: American Institute of Physics), 1993.
- [21] Buccheri, R. *et al.*, *Search for pulsed  $\gamma$ -ray emission from radio pulsars in the COS B data*, *Astronomy and Astrophysics*, **128**, 245–251, 1983.
- [22] Catelli, J. R., Dingus, B. L., and Schneid, E. J., *EGRET Observations of Bursts at MeV Energies*, in *Proceedings of the Fourth Huntsville Gamma-Ray Burst Symposium*, 1997.
- [23] Cavalli-Sforza, M. *et al.*, *A method for obtaining parasitic  $e^+$  or  $e^-$  beams during SLAC Linear Collider operation*, SLAC-PUB-6387, 1993.

- [24] Chandrasekar, S., *The Highly Collapsed Configurations of a Stellar Mass*, Monthly Notices of the Royal Astronomical Society, **95**, 207, 1935.
- [25] Chaput, C. J., *Cosmic Ray Electrons and Positrons from 4.5 to 100 GeV*, Ph.D. thesis, University of Michigan, 1997.
- [26] Cheng, K. S., Ho, C., and Ruderman, M., *Energetic Radiation from Rapidly Spinning Pulsars. I. Outer Magnetosphere Gaps*, Astrophysical Journal, **300**, 500–521, Jan 1986.
- [27] —, *Energetic Radiation from Rapidly Spinning Pulsars. II. Vela and Crab*, Astrophysical Journal, **300**, 522–539, Jan 1986.
- [28] Chiang, J. and Dermer, C. D., *Synchrotron and SSC Emission and the Blast-Wave Model of Gamma-Ray bursts*, Astrophysical Journal, 1998. Submitted, available as <http://xxx.lanl.gov/astro-ph/9803339>.
- [29] Clear, J., Bennett, K., Buccheri, R., Grenier, I. A., Hermesen, W., and Mayer-Haßelwander, H., *A detailed analysis of the high energy gamma-ray emission from the Crab pulsar and nebula*, Astronomy and Astrophysics, **174**, 85, 1987.
- [30] Costa, E. *et al.*, IAU Circular 6572, 1997.
- [31] —, *Discovery of an X-ray afterglow associated with the gamma-ray burst of 28 February 1997*, Nature, **387**, 783–785, 1997.
- [32] Daugherty, J. K. and Harding, A. K., *Electromagnetic Cascades in Pulsars*, Astrophysical Journal, **252**, 337, 1982.
- [33] Dermer, C. D., Chiang, J., and Böttcher, M., *Fireball Loading and the Blast Wave Model of Gamma Ray Bursts*, Astrophysical Journal, 1998. Submitted, available as <http://xxx.lanl.gov/astro-ph/9804174>.
- [34] Dingus, B. L., Catelli, J. R., and Schneid, E. J., *Bursts Detected and NOT Detected by EGRET Imaging Spark Chambers*, in *Proceedings of the Fourth Huntsville Gamma-Ray Burst Symposium*, 1997.
- [35] Djorgovski, S. G., Kulkarni, S. R., Bloom, J. S., Goodrich, R., Frail, D. A., Piro, L., and Palazzi, E., *Spectroscopy of the Host Galaxy of the Gamma-Ray Burst 980703*, <http://xxx.lanl.gov/astro-ph/9808188>, Aug 1998.
- [36] Eadie, W. T., Drijard, D., James, F. E., Roos, M., and Sadoulet, B., *Statistical Methods in Experimental Physics* (Amsterdam: North-Holland), 1971.

- [37] Efron, B. and Petrosian, V., *Testing Isotropy versus Clustering of Gamma-Ray Bursts*, *Astrophysical Journal*, **449**, 216–223, Aug 1995.
- [38] Engovatov, D., *et al.*, *GLAST Beam Test at SLAC*, presented at the 1997 IEEE Nuclear Science Symposium, Nov 1997.
- [39] Fichtel, C. E., Hartman, R. C., Kniffen, D. A., Thompson, D. J., Bignami, G. F., Ögelman, H. B., Özel, M. E., and Tümer, T., *High-Energy Gamma-ray Results from the Second Small Astronomy Satellite*, *Astrophysical Journal*, **198**, 163, 1975.
- [40] Fichtel, C. E., Hartman, R. C., Kniffen, D. A., Thompson, D. J., Bignami, G. F., Ögelman, H. B., Özel, M. E., and Tümer, T., *High-Energy Gamma-Ray Results from the Second Small Astronomy Satellite*, *Astrophysical Journal*, **198**, 163, 1975.
- [41] Fichtel, C. E. and Trombka, J. I., *Gamma Ray Astrophysics: New Insight into the Universe*, chap. 6, p. 152 (Washington, D.C.: NASA), 1981.
- [42] Fierro, J. M., *PULSAR: Program Definition*, *EGRET Document*: EGRET/SU/JMF/94/MAY/01, 1992.
- [43] —, *Observations of Spin-Powered Pulsars with the EGRET Gamma-Ray Telescope*, Ph.D. thesis, Stanford University, 1995.
- [44] Fierro, J. M., Michelson, P. F., and Nolan, P. L., *Phase-Resolved Studies of the High-Energy Gamma-Ray Emission from the Crab, Geminga and Vela Pulsars*, *Astrophysical Journal*, **494**, 734–746, Feb 1998.
- [45] Fierro, J. M. *et al.*, *Pulsed High-Energy Gamma rays from PSR 1055-52*, *Astrophysical Journal*, **413**, L27–L30, Aug 1993.
- [46] —, *EGRET High-Energy Gamma-ray Pulsar Studies. II. Individual Millisecond Pulsars*, *Astrophysical Journal*, **447**, 807–812, 1995.
- [47] Fishman, G. E. *et al.*, *BATSE: The Burst and Transient Source Experiment on the Gamma Ray Observatory*, in W. N. Johnson (editor), *Proceedings of the Gamma-Ray Observatory Science Workshop*, pp. 2–39 (Greenbelt, MD: NASA), 1989.
- [48] Flanagan, C. S., IAU Circular 5311, 1991.
- [49] Frail, D. A., Kulkarni, S. R., Nicastro, L., Feroci, M., and Taylor, G. B., *Nature*, **389**, 261, 1997.

- [50] Frontera, F., *Recent Results on Gamma-Ray Bursts with the BeppoSAX Satellite*, in *Proceedings of the 25th International Cosmic Ray Conference* (World Scientific Publishing), 1997. Available as <http://xxx.lanl.gov/astro-ph/9802157>.
- [51] Frühwirth, R., *Application of Kalman Filtering to Track and Vertex Fitting*, Nuclear Instruments and Methods in Physics Research, **A262**, 444–450, 1987.
- [52] Galama, T. J., Groot, P. J., van Paradijs, J., Kouveliotou, C., Strom, R., de Bruyn, A. G., Heise, J., and in 't Zand, J. M. M., *Optical and radio observations of GRB 970228*, in *Proceedings of the Fourth Huntsville Gamma-Ray Burst Symposium*, Sep 1997.
- [53] Gilman, D., Metzger, A. E., Parker, R. H., Evans, L. G., and Tromba, J. I., *The Distance and Spectrum of the Apollo Gamma-Ray Burst*, Astrophysical Journal, **236**, 951–957, 1980.
- [54] Goldreich, P. and Julian, W. H., *Pulsar Electrodynamics*, Astrophysical Journal, **157**, 869, 1969.
- [55] Gorosabel, J. *et al.*, *Detection of the near-infrared counterpart of GRB971214 3.2 hours after the gamma-ray event*, Astronomy and Astrophysics, **335**, L5–L8, 1998.
- [56] Gregory, P. C. and Loredo, T. J., *A New Method for the Detection of a Periodic Signal of Unknown Shape and Period*, Astrophysical Journal, **398**, 146, 1992.
- [57] Grove, E., private communication, 1997.
- [58] Halpern, J. P. and Holt, S. S., *Discovery of soft X-ray pulsations from the  $\gamma$ -ray source Geminga*, Nature, **357**, 222, 1992.
- [59] Halpern, J. P., Thorstensen, J. R., Helfand, D. J., and Costa, E., *Optical afterglow of the  $\gamma$ -ray burst of 14 December 1997*, Nature, **393**, 41, May 1998.
- [60] Hanami, H., *Magnetic Cannonball Model for Gamma-Ray Bursts*, Astrophysical Journal, **491**, 687–696, Dec 1997.
- [61] Harding, A., *Pulsar  $\gamma$ -Rays: Spectra, Luminosities, and Efficiencies*, Astrophysical Journal, **245**, 267–273, 1981.
- [62] Hartman, R. C., Collmar, W., von Montigny, C., and Dermer, C. D., *Gamma-Ray Blazars*, in C. D. Dermer, M. S. Strickman, and J. D. Kurfess (editors), *Proceedings of the Fourth Compton Symposium*, vol. 410, pp. 307–327 (Woodbury, New York: American Institute of Physics), Apr 1997.

- [63] Hartman, R. C., Kniffen, D. A., Thompson, D. J., Fichtel, C. E., Ögelman, H. B., Tümer, T., and Özel, M. E., *Galactic Plane Gamma-Radiation*, Astrophysical Journal, 1979.
- [64] Hartman, R. C. *et al.*, *Simultaneous Multiwavelength Spectrum and Variability of 3C 279 from  $10^9$  to  $10^{24}$  Hz*, Astrophysical Journal, **461**, 698–712, Apr 1996.
- [65] —, *The Third EGRET Catalog of High-Energy Gamma-Ray Sources*, Astrophysical Journal Supplement, 1998. In press.
- [66] Hayakawa, S., *Propagation of the Cosmic Radiation through Interstellar Space*, Progress in Theoretical Physics, **8**, 571, 1952.
- [67] Heise, J., *et al.*, IAU Circular 6787, Dec 1997.
- [68] Heitler, W., *The Quantum Theory of Radiation* (London: Oxford University Press), 3rd ed., 1954.
- [69] Hermesen, W., Ph.D. thesis, University of Leiden, 1980.
- [70] Hewish, A., Bell, S. J., Pilkington, J. D. H., Scott, P. F., and Collins, R. A., *Observation of a Rapidly Pulsating Radio Source*, Nature, **217**, 709, 1968.
- [71] Hughes, E. B. *et al.*, *Characteristics of the Telescope for High-Energy Gamma-Ray Astronomy Selected for Definition Studies on the Gamma-Ray Observatory*, IEEE Transactions on Nuclear Science, **NS-27**, 1, 364–369, 1980.
- [72] Hunt, G. C., *The Rate of Change of the Period of the Pulsars*, Monthly Notices of the Royal Astronomical Society, **153**, 119–131, 1971.
- [73] Hunter, S. D., Kinzer, R. L., and Strong, A. W., *Diffuse Galactic Continuum Radiation*, in C. D. Dermer, M. S. Strickman, and J. D. Kurfess (editors), *Proceedings of the Fourth Compton Symposium*, vol. 410, pp. 192–207 (Woodbury, New York: American Institute of Physics), Apr 1997.
- [74] Hunter, S. D. *et al.*, *Development of Gas Micro-Structure Detectors for Gamma-Ray Astronomy*, in C. D. Dermer, M. S. Strickman, and J. D. Kurfess (editors), *Proceedings of the Fourth Compton Symposium*, vol. 410, pp. 1606–1610 (Woodbury, New York: American Institute of Physics), Apr 1997.
- [75] —, *EGRET Observations of the Diffuse Gamma-Ray Emission from the Galactic Plane*, Astrophysical Journal, **481**, 1, 205–240, May 1997.
- [76] Hurley, K. *et al.*, *Extended High Energy Emission from a Gamma-Ray Burst*, Nature, **372**, 652, 1994.



- [77] Johnson, W. N., Zdziarski, A. A., Madejski, G. M., Paciesas, W. S., Steinle, H., and Lin, Y.-C., *Seyferts and Radio Galaxies*, in C. D. Dermer, M. S. Strickman, and J. D. Kurfess (editors), *Proceedings of the Fourth Compton Symposium*, vol. 410, pp. 283–305 (Woodbury, New York: American Institute of Physics), Apr 1997.
- [78] Johnson, W. N. *et al.*, *The Oriented Scintillation Spectrometer Experiment: Instrument Description*, Astrophysical Journal Supplement, **86**, 693, 1993.
- [79] Johnston, S., Lyne, A. G., Manchester, R. N., Kniffen, D. A., D’Amico, N., Lim, J., and Ashworth, M., *A high-frequency survey of the southern Galactic plane for pulsars*, Monthly Notices of the Royal Astronomical Society, **255**, 401, 1992.
- [80] Jones, B. B., *Direct Observation of the Massive Dark Halo*, Undergraduate thesis, Princeton University, 1993.
- [81] —, *User’s Manual for timevar 2.0*, EGRET Document: EGRET/SU/BBJ/97/JAN/01, Jan 1997.
- [82] —, *PSF Estimations from Kalman Filters: Subroutines in C++*, World Wide Web, Apr 1998. <http://razzle.stanford.edu/~bbjones/psf/psf.html>.
- [83] Jones, B. B., Lin, Y.-C., Michelson, P. F., Nolan, P. L., Roberts, M. S. E., and Tompkins, W. F., *EGRET Observations of X-Ray Binaries*, in C. D. Dermer, M. S. Strickman, and J. D. Kurfess (editors), *Proceedings of the Fourth Compton Symposium*, vol. 410, pp. 783–787 (Woodbury, New York: American Institute of Physics), Apr 1997.
- [84] Jones, B. B. and Tompkins, W. F., *Preliminary Tracker Simulation Results*, World Wide Web, 1997. <http://egret0.stanford.edu/bbjones/presimres.pdf>.
- [85] —, *A Physicist’s Guide to Kalman Filters*, World Wide Web, Mar 1998. <http://razzle.stanford.edu/~bbjones/expkal.pdf>.
- [86] —, *GLAST Silicon Tracker Prototype Simulations and Beam Test Results*, in preparation.
- [87] Jones, B. B. *et al.*, *Possible EGRET Gamma-Ray Burst Detection Independent of BATSE Triggering*, Astrophysical Journal, **463**, 565–569, Jun 1996.
- [88] Jones, W. C., *Microwave Anisotropy Probe Feed Antenna Design Verification*, Undergraduate thesis, Princeton University, 1998.

- [89] Julier, S. J. and Uhlmann, J. K., *A New Extension of the Kalman Filter to Nonlinear Systems*, in *The Proceedings of AeroSense: The 11th International Symposium on Aerospace/Defense Sensing, Simulation and Controls*, Orlando, Florida.
- [90] Julier, S. J., Uhlmann, J. K., and Durrant-Whyte, H. F., *A New Approach for Filtering Nonlinear Systems*, in *Proceedings of the 1995 American Control Conference*, pp. 1628–1632, Seattle, Washington, 1995.
- [91] Kalman, R. E., *A New Approach to Linear Filtering and Prediction Problems*, Transaction of the ASME—Journal of Basic Engineering, pp. 35–45, Mar 1960.
- [92] Kanbach, G. *et al.*, *The Project EGRET (Energetic Gamma Ray Experiment Telescope) on NASA's Gamma-Ray Observatory GRO*, Space Science Review, **49**, 69, 1988.
- [93] —, *The EGRET Instrument*, in W. N. Johnson (editor), *Proceedings of the Gamma-Ray Observatory Science Workshop*, pp. 2–1 (Greenbelt, MD: NASA), 1989.
- [94] —, *EGRET Observations of the Vela Pulsar, PSR0833-45*, Astronomy and Astrophysics, **289**, 855–867, 1994.
- [95] Kippen, R. M., Woods, P., Connaughton, V., Smith, D. A., Levine, A. M., Remillard, R., and Hurley, K., IAU Circular 6789, Dec 1997.
- [96] Kippen, R. M., *et al.*, IAU Circular 5937, Feb 1994.
- [97] Klebesadel, R. W., Strong, I. B., and Olson, R. A., *Observation of Gamma-Ray Bursts of Cosmic Origins*, Astrophysical Journal, **182**, L85, 1973.
- [98] Kniffen, D. A., Bignami, G. F., Fichtel, C. E., Hartman, R. C., Ögelman, H. B., Thompson, D. J., Özel, M. E., and Tümer, T., in *Proceedings of the 14th International Cosmic Ray Conference*, vol. 1, p. 100, Munich, 1975.
- [99] Kochanek, C. S. and Piran, T., *Gravitational Waves and Gamma-Ray Bursts*, Astrophysical Journal Letters, **417**, L17–L20, Nov 1993.
- [100] Kouveliotou, C. *et al.*, *BATSE Observations of the Very Intense Gamma-Ray Burst GRB 930131*, Astrophysical Journal Letters, **422**, L59–L62, Feb 1994.
- [101] Kulkarni, S. R. *et al.*, *Identification of a host galaxy at redshift  $z=3.42$  for the  $\gamma$ -ray burst of 14 December 1997*, Nature, **393**, 35, 1998.

- [102] Kuzmin, A. D. and Losovskii, B. Y., *Detection of the Radio Pulsar PSR J0633+1746 in Geminga*, *Astronomy Letters*, **23**, 3, 283–285, 1997.
- [103] Kwok, P.-W. *et al.*, *EGRET Observations of Gamma-Ray Bursts on June 1, 1991 and August 14, 1991*, in M. Friedlander, N. Gehrels, and D. J. Macomb (editors), *Compton Gamma-Ray Observatory Symposium*, vol. 280 of *AIP Conference Proceedings*, pp. 855–859 (New York: American Institute of Physics), 1993.
- [104] Lamb, R. C. and Macomb, D. J., *Point Sources of GeV Gamma-Rays*, *Astrophysical Journal*, **488**, 872–880, Oct 1997.
- [105] Lamb, R. C. *et al.*, *Observation of Gamma Rays with a 4.8 Hour Periodicity from Cygnus X-3*, *Astrophysical Journal Letters*, **212**, L63, 1977.
- [106] Large, M. I., Vaughn, A. F., and Mills, B. Y., *A Pulsar Supernova Association?*, *Nature*, **220**, 340, 1968.
- [107] Lee, T. T. and Petrosian, V., *Distributions of Peak Flux and Duration for Gamma-Ray Bursts*, *Astrophysical Journal*, **470**, 479–492, Oct 1996.
- [108] Leonard, P. J. T., *The Challenge of Gamma Ray Burst Observations*, *Science*, **281**, 525, Jul 1998.
- [109] Lin, Y.-C. *et al.*, *EGRET Limits on High-Energy Gamma-Ray Emission from X-Ray- and Low-Energy Gamma-Ray-Selected Seyfert Galaxies*, *Astrophysical Journal Letters*, **416**, L53–L56, Oct 1993.
- [110] Lored, T. J., *From Laplace to Supernova SN1987A: Bayesian Inference in Astrophysics*, in P. Fougere (editor), *Maximum Entropy and Bayesian Methods*, pp. 81–142 (Netherlands: Kluwer Academic Publishing), 1990.
- [111] —, *Promise of Bayesian Inference for Astrophysics*, in E. D. Feigelson and G. J. Babu (editors), *Statistical Challenges in Modern Astronomy*, chap. 12, pp. 275–306 (New York: Springer-Verlag), 1992.
- [112] Lyne, A. G. and Graham-Smith, F., *Pulsar Astronomy* (Cambridge University Press), 1990.
- [113] Mardia, K. V., *Statistics of Directional Data* (London: Academic Press), 1972.
- [114] Mattox, J. R., Bertsch, D. L., Fichtel, C. E., Hartman, R. C., Kniffen, D. A., and Thompson, D. J., *SAS 2 Observation of Pulsed High-Energy Gamma Radiation from Geminga*, *Astrophysical Journal*, **401**, L23, 1992.

- [115] Mattox, J. R., Hofstadter, R., Hughes, E. V., Lin, Y.-C., Nolan, P. L., and Walker, A. H., *Use of a Tunable Quasimonoenergetic Gamma-Ray Beam for the Calibration of the EGRET Gamma-Ray Telescope in the Range 20–24000 MeV*, Nuclear Instruments and Methods in Physics Research, **B24/25**, 888–892, 1987.
- [116] Mattox, J. R., Koh, D. T., Lamb, R. C., Macomb, D. J., Prince, T. A., and Ray, P. S., *A search for radio-quiet gamma-ray pulsars in the EGRET data*, Astronomy and Astrophysics Supplement Series, **120**, 4, C95–C98, Dec 1996.
- [117] Mattox, J. R. *et al.*, *The Likelihood Analysis of EGRET Data*, Astrophysical Journal, **461**, 396, Apr 1996.
- [118] Mayall, N. U. and Oort, J. H., *Further Data Bearing on the Identification of the Crab Nebula with the Supernova of 1054 A. D.*, Publications of the Astronomical Society of the Pacific, **54**, 95–104, 1942.
- [119] Mayer-Haßelwander, H. A. *et al.*, *COS B Observation of the Milky-Way in High-Energy Gamma-Rays*, Annals of the New York Academy of Sciences, 1980.
- [120] Mayer-Haßelwander, H. A. *et al.*, *High-Energy Gamma Radiation from Geminga Observed by EGRET*, Astrophysical Journal, **421**, 276–283, Jan 1994.
- [121] McLaughlin, M. A., Mattox, J. R., Cordes, J. M., and Thompson, D. J., *Variability of CGRO/EGRET Gamma-Ray Sources*, Astrophysical Journal, 1996.
- [122] Meegan, C., Hurley, K., Connors, A., Dingus, B., and Matz, S., *A Review of Gamma Ray Bursts*, in C. D. Dermer, M. S. Strickman, and J. D. Kurfess (editors), *Proceedings of the Fourth Compton Symposium*, vol. 410, pp. 407–417 (Woodbury, New York: American Institute of Physics), Apr 1997.
- [123] Meegan, C. A., Fishman, G. J., Wilson, R. B., Paciesas, W. S., Pendleton, G. N., Horack, J. M., Brock, M. N., and Kouveliotou, C., *Spatial distribution of  $\gamma$ -ray bursts observed by BATSE*, Nature, **355**, 143, Jan 1992.
- [124] Meegan, C. A. *et al.*, *The Third BATSE Gamma-Ray Burst Catalog*, Astrophysical Journal Supplement, **106**, 65–110, 1996.
- [125] —, *Current BATSE Gamma-Ray Burst Catalog*, <http://www.batse.msfc.nasa.gov/data/grb/catalog>, Jul 1998.
- [126] Merck, M. *et al.*, *Study of the Spectral Characteristics of Unidentified Galactic EGRET Sources. Are they Pulsar-Like?*, Astronomy and Astrophysics Supplement Series, **120**, 4, 465, Dec 1996.

- [127] Mészáros, P. and Rees, M. J., *Optical and Long-Wavelength Afterglows from Gamma-Ray Bursts*, *Astrophysical Journal*, **476**, 232, 1997.
- [128] Mészáros, P., Rees, M. J., and Papathanassiou, H., *Spectral Properties of Blast-Wave Models of Gamma-Ray Burst Sources*, *Astrophysical Journal*, **432**, 181–193, Sep 1994.
- [129] Metzger, A. E., Parker, R. E., Gilman, D., Peterson, L. E., and Tromba, J. I., *Observation of a Cosmic Gamma-Ray Burst on Apollo 16 I. Temporal Variability and Energy Spectrum*, *Astrophysical Journal Letters*, **194**, L19–L25, 1974.
- [130] Metzger, M. R., Cohen, J. G., Chaffee, F. H., and Blandford, R. D., IAU Circular 6676, Jun 1997.
- [131] Metzger, M. R., Djorgovski, S. G., Kulkarni, S. R., Steidel, C. C., Adelberger, K. L., Frail, D. A., Costa, E., and Frontera, F., *Spectral constraints on the redshift of the optical counterpart to the gamma-ray burst of 8 May 1997*, *Nature*, **387**, 878–880, 1997.
- [132] Metzger, M. R., Djorgovski, S. G., Steidel, C. C., Kulkarni, S. R., Adelberger, K. L., and Frail, D. A., IAU Circular 6655, May 1997.
- [133] Michelson, A. A. and Morley, E. W., *On the Relative Motion of the Earth and the Luminiferous Æther*, *American Journal of Science—Third Series*, **34**, 21, 333, 1887.
- [134] Michelson, P. F., NASA Mission Definition Study Proposal, 1995. <http://www-glast.stanford.edu/studyprop/overview.html>.
- [135] Michelson, P. F. *et al.*, *Search for Periodic Gamma-Ray Emission from Cygnus X-3 by the EGRET Telescope on the Compton Gamma-Ray Observatory*, *Astrophysical Journal*, **401**, 724, 1992.
- [136] Michelson, P. F., *et al.*, *EGRET Upper Limits to the High-Energy Gamma-Ray Emission from the Millisecond Pulsars in Nearby Globular Clusters*, *Astrophysical Journal*, **435**, 218–224, Nov 1994.
- [137] Mitsuda, K., Inoue, H., Nakamura, N., and Tanaka, Y., *Luminosity-Related Changes of the Energy Spectrum of X1608-522*, *Publications of the Astronomical Society of Japan*, **41**, 97, 1989.
- [138] von Montigny, C. *et al.*, *Multiwavelength Observations of 3C 273 in 1993–1995*, *Astrophysical Journal*, **483**, 161–177, Jul 1997.

- [139] Mori, M., *Cygnus X-3 and EGRET Gamma-Ray Observations*, Astrophysical Journal, **476**, 842, 1997.
- [140] Motz, J. W., Olsen, H. A., and Koch, H. W., *Pair Production by Photons*, Reviews of Modern Physics, **41**, 4, 581, Oct 1969.
- [141] Mukherjee, R., Bertsch, D. L., Dingus, B. L., Kanbach, G., Kniffen, D. A., Sreekumar, P., and Thompson, D. J., *On the Nature of the Unidentified EGRET Sources: Are They Geminga-Like Pulsars?*, Astrophysical Journal, **441**, L61–L64, Mar 1995.
- [142] Murakami, T., in C. A. Meegan, R. Preece, and T. M. Koshut (editors), *Proceedings of the Fourth Huntsville Symposium on Gamma-Ray Bursts*, 1998.
- [143] Muslimov, A. G. and Harding, A. K., *Toward the Quasi-Steady State Electrodynamics of a Neutron Star*, Astrophysical Journal, **485**, 735–746, Aug 1997.
- [144] Muslimov, A. G. and Tsygan, A. I., *General relativistic electric potential drops above pulsar polar caps*, Monthly Notices of the Royal Astronomical Society, **255**, 61–70, 1992.
- [145] Narayan, R., Paczyński, B., and Piran, T., *Gamma-Ray Bursts as the Death Throes of Massive Binary Stars*, Astrophysical Journal Letters, **395**, L83–L86, Aug 1992.
- [146] Nel, H. I. *et al.*, *EGRET High-Energy Gamma-Rays Pulsar Studies. III. A Survey*, Astrophysical Journal, **465**, 898–906, Jul 1996.
- [147] Nelson, W. R., Hirayama, H., and Rogers, D. W. O., *The EGS4 Code System*, Tech. Rep. SLAC-265, Stanford Linear Accelerator Center, 1985.
- [148] Nemiroff, R. J., *A Century of Gamma Ray Burst Models*, Comments on Astrophysics, **17**, 4, 189, 1994.
- [149] Nolan, P. L., Share, G. H., Matz, S., Chupp, E. L., Forrest, D. J., and Rieger, E., *High-Energy Emission from Gamma-Ray Bursts*, in S. E. Woosley (editor), *High-Energy Transients in Astrophysics*, pp. 399–402, 1984.
- [150] Nolan, P. L. *et al.*, *Performance of the EGRET Astronomical Gamma-ray Telescope*, IEEE Transactions on Nuclear Science, **39**, 993, 1992.
- [151] —, *Observations of the Crab Pulsar and Nebula by the EGRET Telescope on the Compton Gamma Ray Observatory*, Astrophysical Journal, **409**, 697–704, Jun 1993.

- [152] —, *EGRET Observations of Pulsars*, Astronomy and Astrophysics Supplement Series, **120**, 4, C61–C64, Dec 1996.
- [153] Ostriker, J. P. and Gunn, J. E., *On the Nature of Pulsars. I. Theory*, Astrophysical Journal, **157**, 1395, 1969.
- [154] Øverbø, I., Mork, K. K., and Olsen, H. A., *Exact Calculation of Pair Production*, Physical Review, **175**, 1978, 1968.
- [155] Özel, M. E. and Mayer-Haßelwander, H. A., in L. Scarsi, V. D. Gesù, P. Crane, J. H. Friedman, and S. Levialdi (editors), *Data Analysis in Astronomy*, p. 81 (Plenum), 1984.
- [156] Özel, M. E. and Thompson, D. J., *On the Nature of Unidentified 2EG Sources at High Latitudes*, Astrophysical Journal, **463**, 105–109, May 1996.
- [157] Paczyński, B., *Gamma-Ray Bursters at Cosmological Distances*, Astrophysical Journal Letters, **308**, L43–L46, Sep 1986.
- [158] —, *Are Gamma-Ray Bursts in Star-Forming Regions?*, Astrophysical Journal, **494**, L45–L48, Feb 1998.
- [159] van Paradijs, J. *et al.*, *Transient optical emission from the error box of the gamma-ray burst of 28 February 1997*, Nature, **386**, 686–689, 1997.
- [160] Petrosian, V., *Interpretation of Gamma-Ray Burst Source Count Statistics*, Astrophysical Journal Letters, **402**, L33–L36, Jan 1993.
- [161] Petrosian, V. and Efron, B., *On the Correlation of Angular Position with Time of Occurrence of Gamma-Ray Bursts*, Astrophysical Journal Letters, **441**, L37–L38, Mar 1995.
- [162] Petrosian, V. and Lee, T. T., *The Fluence Distribution of Gamma-Ray Bursts*, Astrophysical Journal Letters, **467**, L29–L32, Aug 1996.
- [163] Pohl, M., Kanbach, G., Hunter, S. D., and Jones, B. B., *The Pulsar Contribution to the Diffuse Galactic Gamma-Ray Emission*, Astrophysical Journal, **491**, 149–164, Dec 1997.
- [164] Pollock, A. M. T., Bignami, G. F., Hermesen, W., Kanbach, G., Lichti, G. G., Masnou, J. L., Swanenburg, B. N., and Wills, R. D., *Search for Gamma-Radiation from Extra-Galactic Objects using a Likelihood Method*, Astronomy and Astrophysics, **94**, 1, 116–120, 1981.

- [165] Preece, R. D., Pendleton, G. N., Briggs, M. S., Mallozzi, R. S., Paciesas, W. S., Band, D. L., Matteson, J. L., and Meegan, C. A., *BATSE Observations of Gamma-Ray Burst Spectra. IV. Time-Resolved High-Energy Spectroscopy*, *Astrophysical Journal*, **496**, 849, Apr 1998.
- [166] Press, W. H., Teukolsky, S. A., Vetterling, W. T., and Flannery, B. P., *Numerical Recipes in C* (Cambridge University Press), 2nd ed., 1992.
- [167] Ramanamurthy, P. V. *et al.*, *EGRET Detection of Pulsed Gamma Radiation from PSR B1951+32*, *Astrophysical Journal*, **447**, L109–L112, Jul 1995.
- [168] Rees, M. J. and Mészáros, P., *Refreshed Shocks and Afterglow Longevity in Gamma-Ray Bursts*, *Astrophysical Journal*, **496**, L1–L4, 1998.
- [169] Ritz, S. *et al.*, *Nuclear Instruments and Methods*, in preparation.
- [170] Roberts, M. S. E. and Romani, R. W., *ASCA Observations of the Unidentified EGRET Source 2EGS J1418-6049*, *Astrophysical Journal*, in press.
- [171] Romani, R. W. and Yadigaroglu, I.-A., *Gamma-Ray Pulsars: Emission Zones and Viewing Geometries*, *Astrophysical Journal*, **438**, 314–321, 1995.
- [172] Ruderman, M., *Theories of Gamma-Ray Bursts*, *Annals of the New York Academy of Science*, **262**, 164–180, 1975.
- [173] Sahu, K. C., *et al.*, *The optical counterpart to the  $\gamma$ -ray burst GRB970228 observed using the Hubble Space Telescope*, *Nature*, **387**, 476, 1997.
- [174] Scargle, J. D., *Studies in Astronomical Time Series Analysis: V. Bayesian Blocks, A New Method to Analyze Structure in Photon Counting Data*, *Astrophysical Journal*, 1998. In press.
- [175] Schmidt, W. K. H., *Distance limit for a class of model  $\gamma$ -ray burst sources*, *Nature*, **271**, 525, 1978.
- [176] Schneid, E. J. *et al.*, *EGRET detection of high energy gamma rays from the gamma-ray burst of 3 May 1991*, *Astronomy and Astrophysics*, **255**, L13, 1992.
- [177] —, *EGRET measurements of Energetic Gamma Rays from the Gamma-Ray Bursts of 1992 June 22 and 1994 March 1*, *Astrophysical Journal*, **453**, 95–99, Nov 1995.
- [178] Schönfelder, V. *et al.*, *Instrument Description and Performance of the Imaging Gamma-Ray Telescope COMPTEL aboard the Compton Gamma-Ray Observatory*, *Astrophysical Journal Supplement*, **86**, 2, 657, Jun 1993.



- [179] Shakura, N. I. and Sunyaev, R. A., *Black Holes in Binary Systems. Observational Appearance*, Astronomy and Astrophysics, **24**, 337, 1973.
- [180] Shapiro, I. I., *Fourth Test of General Relativity*, Physical Review Letters, **13**, 798, 1964.
- [181] Sommer, M. *et al.*, *High Energy Gamma Rays from the Intense January 31, 1993 Gamma Ray Burst*, Astrophysical Journal Letters, **422**, L63, 1993.
- [182] Sreekumar, P. *et al.*, *EGRET Observations of the Extragalactic Gamma-Ray Emission*, Astrophysical Journal, **494**, 523–534, Feb 1998.
- [183] Staelin, D. H. and Reifenstein, E. C., *Pulsating Radio Source near the Crab Nebula*, Science, **162**, 1481, 1968.
- [184] Stampfer, D., Regler, M., and Frühwirth, R., *Track fitting with energy loss*, Computer Physics Communications, **79**, 157–164, 1994.
- [185] Standish Jr., E. M., *The observational basis for JPL's DE 200, the planetary ephemerides of the Astronomical Almanac*, Astronomy and Astrophysics, **233**, 252–271, 1990.
- [186] Tavani, M., *Theory of Gamma-Ray Burst Emission in Light of BSAX Results*, in L. Scarsi, H. Bradt, P. Giommi, and F. Fiore (editors), *The Active X-Ray Sky: Results from BeppoSAX and Rossi-XTE*, Nuclear Physics B Proceedings Supplement, Accademia Nazionale dei Lincei, Rome, Italy, Oct 1997.
- [187] Taylor, J. H., Manchester, R. N., and Lyne, A. G., *Catalog of 558 Pulsars*, Astrophysical Journal Supplement, **88**, 529–568, 1993. Available at <http://puppsr.princeton.edu/pulsar/catalog.shtml>.
- [188] Taylor, J. H. and Weisberg, R. M., *Further Experimental Tests of Relativistic Gravity Using the Binary Pulsar PSR 1913+16*, Astrophysical Journal, **345**, 434, 1989.
- [189] Thompson, D. J., Fichtel, C. E., Hartman, R. C., Kniffen, D. A., and Lamb, R. C., *Final SAS 2 Gamma-Ray Results on Sources in the Galactic Anticenter Region*, Astrophysical Journal, **213**, 252, 1977.
- [190] Thompson, D. J., Fichtel, C. E., Kniffen, D. A., and Öggleman, H. B., *SAS 2 High-Energy Gamma-Ray Observations of Vela Pulsar*, Astrophysical Journal Letters, **200**, L79, 1975.

- [191] Thompson, D. J., Harding, A. K., Hermsen, W., and Ulmer, M. P., *Gamma-Ray Pulsars: The Compton Observatory Contribution to the Study of Isolated Neutron Stars*, in C. D. Dermer, M. S. Strickman, and J. D. Kurfess (editors), *Proceedings of the Fourth Compton Symposium*, vol. 410, pp. 39–56 (Woodbury, New York: American Institute of Physics), Apr 1997.
- [192] Thompson, D. J. *et al.*, *Pulsed High Energy Gamma Rays from the Radio Pulsar PSR 1706-44*, *Nature*, **359**, 615–616, Oct 1992.
- [193] —, *Calibration of the Energetic Gamma Ray Experiment Telescope (EGRET) for the Compton Gamma Ray Observatory*, *Astrophysical Journal Supplement*, **86**, 629, 1993.
- [194] —, *EGRET High-Energy Gamma-Ray Pulsar Studies: I. Young Spin-Powered Pulsars*, *Astrophysical Journal*, **436**, 229–238, 1994.
- [195] —, *The Second EGRET Catalog of High-Energy Gamma-Ray Sources*, *Astrophysical Journal*, **101**, 259–286, Dec 1995.
- [196] —, *Supplement to the Second EGRET Catalog of High-Energy Gamma-Ray Sources*, *Astrophysical Journal Supplement*, **107**, 227–237, Nov 1996.
- [197] T'o-T'o\*, *Sung-Shih* (“History of the Sung Dynasty”), 1313.
- [198] Tompkins, W. F., *Why TS is Not (Necessarily) Distributed as  $\chi^2$  with 3 D.o.F.*, World Wide Web: <http://razzle.stanford.edu/~billt/papers/tsreport.ps>, Mar 1995.
- [199] —, *Applications of Likelihood Analysis in Gamma-Ray Astrophysics*, Ph.D. thesis, Stanford University, 1999.
- [200] Tompkins, W. F., Jones, B. B., Nolan, P. L., Kanbach, G., Ramanamurthy, P. V., and Thompson, D. J., *EGRET Gamma-Ray Observations of the Crab P2/P1 Ratio*, *Astrophysical Journal*, **487**, 385–387, Sep 1997.
- [201] Tutukov, A. V. and Yungelson, L. R., *Merging of binary white dwarfs, neutron stars and black holes under the influence of gravitational wave radiation*, *Monthly Notices of the Royal Astronomical Society*, **268**, 871, 1994.
- [202] Ulmer, M. P. *et al.*, *Compton Gamma-Ray Observatory Observations of the Crab Pulsar*, *Astrophysical Journal*, **448**, 356, Jul 1995.

---

\*While reported here, the Astronomer responsible was probably Yang Wei-tê.

- [203] Vietri, M., *The Soft X-Ray Afterglow of Gamma-Ray Bursts: A Stringent Test for the Fireball Model*, *Astrophysical Journal*, **478**, L9–L12, Mar 1997.
- [204] Waxman, E., *Angular Size and Emission Timescales of Relativistic Fireballs*, *Astrophysical Journal*, **491**, L19–L22, Dec 1997.
- [205] —,  *$\gamma$ -Ray Burst Afterglow: Confirming the Cosmological Fireball Model*, *Astrophysical Journal*, **489**, L33–L36, Nov 1997.
- [206] Waxman, E. and Bahcall, J., *High Energy Neutrinos from Cosmological Gamma-Ray Burst Fireballs*, *Physical Review Letters*, **78**, 12, 2292–2295, Mar 1997.
- [207] White, N. E., Nagase, F., and Parmar, A. N., *The properties of X-ray binaries*, in H. G. Lewin, J. van Paradijs, and E. P. J. van den Heuvel (editors), *X-Ray Binaries*, Cambridge Astrophysics Series, chap. 1 (Cambridge University Press), 1995.
- [208] White, R. S., Ryan, J. M., Wilson, R. B., and Zych, A. D., *Evidence that cosmic  $\gamma$ -ray bursts are galactic*, *Nature*, **271**, 635, 1978.
- [209] Wijers, R., *The burst, the burster, and its lair*, *Nature*, **393**, 13, May 1998.
- [210] Wijers, R. A. M. J., Rees, M. J., and Mészáros, P., *Shocked by GRB 970228: the afterglow of a cosmological fireball*, *Monthly Notices of the Royal Astronomical Society*, **288**, L51, 1997.
- [211] Wilks, S. S., *The large-sample distribution of the likelihood ratio for testing composite hypotheses*, *Annals of Mathematical Statistics*, **9**, 60, 1938.
- [212] Willis, T. D., *Observations of the Isotropic Diffuse Gamma-Ray Background with the EGRET Telescope*, Ph.D. thesis, Stanford University, Aug 1996.
- [213] Wills, R. D., *et al.*, *High-energy  $\gamma$ -ray light curve of PSR0531+21*, *Nature*, **296**, 723, 1983.
- [214] Woosley, S. E., *Gamma-ray bursts from stellar mass accretion disks around black holes*, *Astrophysical Journal*, **405**, 273–277, 1993.
- [215] Yadigaroglu, I.-A. and Romani, R. W., *Gamma-Ray Pulsars: Beaming Evolution, Statistics, and Unidentified EGRET Sources*, *Astrophysical Journal*, **449**, 211–215, 1995.
- [216] —, *Gamma-Ray Pulsars and Massive Stars in the Solar Neighborhood*, *Astrophysical Journal*, **476**, 347–356, Feb 1997.